INFORMATION TO USERS

This manuscript has been reproduced from the microfilm master. UMI films the text directly from the original or copy submitted. Thus, some thesis and dissertation copies are in typewriter face, while others may be from any type of computer printer.

The quality of this reproduction is dependent upon the quality of the copy submitted. Broken or indistinct print, colored or poor quality illustrations and photographs, print bleedthrough, substandard margins, and improper alignment can adversely affect reproduction.

In the unlikely event that the author did not send UMI a complete manuscript and there are missing pages, these will be noted. Also, if unauthorized copyright material had to be removed, a note will indicate the deletion.

Oversize materials (e.g., maps, drawings, charts) are reproduced by sectioning the original, beginning at the upper left-hand corner and continuing from left to right in equal sections with small overlaps. Each original is also photographed in one exposure and is included in reduced form at the back of the book.

Photographs included in the original manuscript have been reproduced xerographically in this copy. Higher quality 6" x 9" black and white photographic prints are available for any photographs or illustrations appearing in this copy for an additional charge. Contact UMI directly to order.

UMI®

Bell & Howell Information and Learning
300 North Zeeb Road, Ann Arbor, MI 48106-1346 USA
800-521-0600

Reproduced with permission of the copyright owner. Further reproduction prohibited without permission.

A

Photovoltaic Conversion in the Multiple Quantum Well InGaAsP Semiconductor Heterostructures

by

Oleg Yurievich Raisky

A dissertation submitted to the Graduate Faculty in Physics in partial fulfillment of the requirements for the degree of Doctor in Philosophy, The City University of New York.

1999

UMI Number: 9946212

UMI
300 North Zeeb Road
Ann Arbor, MI 48103

This manuscript has been read and accepted for the Graduate Faculty in Physics in satisfaction of the dissertation requirement for the degree of Doctor in Philosophy.

9/9/99
Date

Robert R Alfano
Chair of the Examining Committee
Dr. Robert. R. Alfano
Distinguished Professor of Science and Engineering, Department of Physics and Electrical Engineering, The City College of New York of the City University of New York

9/10/99
Date

Executive Officer
Dr. Louis Celenza

Joseph L Birman
Dr. Joseph L. Birman
Distinguished Professor of Physics, Department of Physics, The City College of New York of the City University of New York

Dr. Kai Shum
Professor, Department of Electrical Engineering, The City College of New York of the City University of New York

Frederick W. Smith
Dr. Frederic Smith
Professor, Department of Physics, The City College of New York of the City University of New York

Dr. C. Lewis Reynolds, Jr.
Distinguished Member of the Technical Staff, Bell Laboratories, Lucent Technologies

Wubao Wang
Dr. Wubao B. Wang
Department of Physics, The City College of New York of the City University of New York

Supervisory Committee

The City University of New York

Abstract

Photovoltaic Conversion in the Multiple Quantum Well InGaAsP Semiconductor Heterostructures

by

Oleg Yurievich Raisky

Adviser: Robert R. Alfano, Distinguished Professor of Science and Engineering

The topic of this thesis is the physics of carrier transport and photovoltaic conversion in InP-based multiple quantum well (MQW) and bulk heterostructures. A new concept of enhancing MQW solar cell conversion efficiency using sequential resonant tunneling (SRT) transfer was introduced. MQW InGaAsP/InP solar cells were designed, grown and investigated. Sample characterization was conducted using a wide set of techniques: photoluminescence (PL) and photocurrent (PC) measurements, current-voltage (I-V) measurements, electroreflectance and secondary ion mass spectrometry. PL, I-V and PC data were studied for their temperature and bias dependence. Enhancement of the photocurrent and reduction of the radiative recombination losses in an InGaAsP/InP MQW heterostructure due to built-in SRT have been observed for the first time. Photovoltaic efficiency measurements showed that the MQW solar cells outperformed the control non-MQW cells by 13% (relative efficiency of the control sample taken as a 100%). The effect of the SRT on the performance was relatively small because of (1) the small magnitude of the SRT peak and (2) the location of the peak out of the cell operational range. Based on the obtained results the criteria for successful implementation of the SRT in MQW structures for the purpose of enhancement of photovoltaic efficiency have been established.

Acknowledgments

I would like to thank and express my gratitude to my thesis adviser, Professor Robert R. Alfano, without whom none of this could happen. His vast knowledge and expertise were invaluable source of information, his trust in me and my research helped to carry over this project to its end.

I am extremely thankful to Dr. Wubao Wang who was tremendously helpful during all my time as a graduate student. His hardworking style and optimism were a constant encouragement. Without him my life would be much more difficult.

I am particularly grateful to Dr. C. Lewis Reynolds of Lucent Technologies. Without his willingness to support my research and share his valuable time this project could not survived.

I would also like to thank Professor Fred Pollak, Dr. Wei Sun and Dr. Arndt Jaeger from Brooklyn College for helping me with the electroreflectance results. Their contribution to my research have really moved it in the right direction.

I want to thank Professors Joseph Birman, Frederic Smith and Kai Shum for serving on my doctoral committee. Their questions and remarks have helped me to look at my research at different angles.

Dr. Dana Calistru deserves a special "thank you". Without her, Room 228 would be much colder and darker.

Last but not least I would like to thank my parents for their endless patience and support.

To my parents,
Yury and Alevtina Raisky

Contents

Copyright ii

Approval page iii

Abstract iv

Acknowledgments v

Dedication vi

Table of Contents vii

List of Figures xii

List of Tables xxi

1 Introduction 1

1.1 Historical Background On Multiple Quantum Well Structures And Solar Cells 1

1.2 Thesis Organization 10

1.3 Thesis Statement 12

2 Theoretical background 14

2.1 Introduction 14

2.2 Quantum Well Semiconductor Heterostructures 15

2.2.1 The $k \cdot p$ Method of the Band Structure Description 17
2.2.2 Envelope Function Approximation 21
2.2.3 Optical Properties of MQW Heterostructures 25
2.2.4 Strained Heterostructures 33
2.2.5 Quantum Confined Stark Effect 37
2.2.6 Carrier Escape and Transport in MQW Structures 37
2.2.7 Recombination of Carriers in MQW Structures 41
2.2.8 Resonant Tunneling Transport in MQW Structures 44
2.3 Principles of Photovoltaic Conversion 52
2.3.1 Absorption and Emission of Light in Semiconductors 53
2.3.2 Carrier Transport 57
2.3.3 Operation of a Solar Cell 62
2.3.4 Fundamental Solar Cell Parameters 66
2.3.5 Efficiency Limitations of An Ideal Single Band Solar Cell. 68
2.4 Multiple Quantum Well Solar Cells 70
2.4.1 Multigap Solar Cells 70
2.4.2 MQW Solar Cells 72
2.4.3 An Ideal Model of a Quantum Well Solar Cell 76
2.5 Numerical Solution of the Poisson's Equation in Semiconductor Heterostructures 80
2.6 Conclusions 84

3 Experimental Setup 85
3.1 Introduction 85
3.2 Photoluminescence Measurements 86
3.2.1 Description of the Major Components 87
3.3 Photocurrent Measurements 93
3.3.1 Description of the Major Components 95

3.4 Current-Voltage and Photovoltaic Efficiency Measurements 96
3.5 Sample Growth and Preparation 97
  3.5.1 Growth and Processing 97
  3.5.2 Cutting 99
  3.5.3 Wiring 100

4 Investigation of Photoluminescence and Photocurrent in $In_xGa_{1-x}As_yP_{1-y}$ Strained MQW Heterostructures 104
4.1 Introduction 104
4.2 Samples 105
4.3 Experiment 106
4.4 Results 106
  4.4.1 Photoluminescence Measurements 106
  4.4.2 Photocurrent Measurements 114
  4.4.3 Dark Current Measurements 116
4.5 Discussion 116
4.6 Calculations of the Energy States and Escape Rates 122
4.7 Conclusion 128

5 Investigation of the $In_xGa_{1-x}As_yP_{1-y}$ MQW Solar Cell Structures 129
5.1 Introduction 129
5.2 Theoretical Background 134
5.3 Samples 139
5.4 The Top Grid Contact 140
5.5 Experimental Methods 142
5.6 Results 143
  5.6.1 Efficiency Measurements 143
  5.6.2 Transmission and Reflection Measurements 144

5.6.3 Effect of the Top Layer on Cell Performance 146
5.6.4 Photocurrent and Photoluminescence Measurements 150
5.7 Discussion 153
5.8 Conclusion 156

6 Resonant Enhancement of the Photocurrent in MQW Photovoltaic Devices 158
6.1 Introduction 158
6.2 SRT in MQW Structures 160
6.3 Samples and Experimental Setup 165
6.3.1 Modulation Spectroscopy: Electroreflectance 165
6.3.2 SIMS 167
6.4 Results 167
6.4.1 Photoluminescence and Photocurrent Measurements 167
6.4.2 Electroreflectance Results 176
6.4.3 SIMS Results 177
6.5 Discussion 177
6.6 Conclusion 182
6.6.1 Criteria for Successful Implementation of the SRT in MQW Solar Cell 185

7 Conclusion 186
7.1 Thesis summary 186
7.2 Future developments in Photovoltaics 187
7.2.1 Issues to be addressed 187
7.2.2 MQW Solar Cells 189
7.2.3 Graded Band-Gap Solar Cell 190
7.2.4 Solar Cell with Internal Quantum Efficiency > 1 192
7.2.5 Solar Cell with Intermediate Bandgap 193

A Transfer Matrix Method 194

B "Ke236" – a data acquisition program 198

Appendices 194

Bibliography 200

Index 205

List of Figures

1.1 Free carrier escape and transfer processes in the MQW structure. The τ's are different characteristic times associated with these processes: τ_t is the tunneling escape time, τ_{th} is the thermionic escape time, τ_{cap} is the capture time, τ_{dr} is the drift time, and τ_{pl} is radiative recombination time; indices e and h refer to electrons and holes, respectively. 7

1.2 Multiple quantum well structures with the different tunneling alignments: (a) – non-sequential process, (b) – sequential process, (c) – phonon-assisted tunneling. 9

2.1 Room temperature energy bandgaps of several III-V and II-VI group semiconductors versus their lattice constants. The solid lines connect the semiconductors which can form stable alloys. 16

2.2 Examples of the nanostructures: (a) – a single quantum well, (b) – a superlattice. 16

2.3 Main properties of the quantum well bound states: (a) – conduction band profile, energy levels and their envelope functions, (b) – in-plane dispersion relations of the subbands, (c) – density of states as a function of energy. . . . 25

2.4 Optical transitions in the quantum well bound states. $E_{1,2,3}$ are the conduction band Γ_6 subbands, $LH_{1,2}$ and $HH_{1,2,3}$ are the valence band Γ_8 light and heavy hole subbands, respectively. 27

2.5 Diagram showing allowed polarization for (a) intraband and (b) interband quantum well transitions . . . 30

2.6 Strained quantum well configurations: (1) – no strain, (2) – biaxial compression, (3) – biaxial tension. . . . 36

2.7 The effect of the electric field on quantum well states. . . . 38

2.8 Free carrier escape and transfer processes in the MQW structure. τ's are different characteristic times associated with these processes: τ_t is the tunneling escape time, τ_{th} is the thermionic escape time, τ_{cap} is the capture time, τ_{dr} is the drift time, and τ_{pl} is radiative recombination time; indices e and h refer to electrons and holes, respectively . . . 39

2.9 Semiconductor surface states. N_S is the density of the surface states, E_f is the Fermi energy. . . . 44

2.10 Current- voltage characteristic of a double-barrier resonant tunneling AlGaAs/GaAs diode. The right side of the figure shows schematic band diagram at different points of the I-V curve. . . . 46

2.11 Sequential resonant tunneling in multiple quantum well structure . . . 48

2.12 Voltage oscillations in the current-voltage characteristic of an MQW resonant tunneling structure. The period of the oscillations, ΔV, is equal to the quantum well subband separation, $\frac{E_2-E_1}{e}$. . . . 49

2.13 Non-Sequential resonant tunneling in multiple quantum well structure . . . 50

2.14 Differential absorption rise time vs. applied field in MQW GaAs/AlGaAs. . . 52

2.15 Experimental dependence of mobility (squares) in $n-$type GaAs determined by Hall measurements. The dotted curves are the corresponding contributions from the various scattering mechanisms . . . 61

2.16 Layer diagram of a p-n junction solar cell. . . . 63

2.17 Schematic representation of the semiconductor *p-n* junction under illumination. E_c and E_v are conduction and valence band edges, F_n and F_p are the quasi-Fermi levels. 64

2.18 Equivalent circuit of the *p-n* junction solar cell. 67

2.19 Graphical analysis of the photovoltaic efficiency of solar cell. The top curve is cell's energy bandgap E_{gap} versus absorbed photon flux $\Phi(E)$. The lower curve is a work done per absorbed photon. The area under top curve is the solar power per unit area. The shaded areas are different losses. 69

2.20 Solar cell efficiency versus device energy gap for the solar concentration of 1 and 1000 suns 71

2.21 Two-band gap versus single bandgap solar cell efficiency. 72

2.22 Dark current of AlGaAs/GaAs SQW, MQW and control samples at fixed bias 0.6 V plotted as a function of the effective bandgap for absorption (E_a) 74

2.23 Open circuit voltage of AlGaAs/GaAs SQW, MQW and control samples vs. the effective bandgap for absorption (E_a) measured in a 3200K black body spectrum. The dotted line indicates the enhancement, above that of the control cell constructed from the well material, expected if V_{oc} is proportional to the E_a. 75

2.24 Flowchart of the Poisson solver. 82

3.1 Experimental setup for photoluminescence measurements. `F` is the long pass filter, `L1` and `L2` – the achromatic lenses, `G` – the grating turret. 90

3.2 Flowchart of the *Ke236* program - the program to control a data acquisition using the Keithley 236 SMU, SR830 Lock-In and Triax-320. 92

3.3 Experimental setup for the photocurrent measurements. `F` is the longpass filter, `G` – the grating turret 94

3.4 Electrical circuitry of I–V measurements. 95

3.5 Experimental setup for current-voltage and photovoltaic efficiency measurements. 98
3.6 Top view of the MQW InGaAsP/InP sample #OE2188 (left) and InP control sample #OE2126 (right) 100
3.7 View of the InGaAsP/InP sample wired and placed in the DIP header plug. 101
3.8 Effect of the heat on the I-V characteristics of the samples. 102
3.9 View of the InGaAsP/InP sample inserted in the ZIF socket. 103

4.1 Layer diagram of the InGaAsP/InP MQW heterostructures (samples #381 and #382). 105
4.2 Photoluminescence spectra of the InGaAsP/InP MQW heterostructures at $T = 77$ K. Thick line – the 80 Å barrier sample; thin line – the 150 Å barrier sample 107
4.3 Evolution of the PL spectra with temperature (sample #381, InGaAsP/InP MQW heterostructure) 109
4.4 QW PL peak position versus temperature. Circles – the 80 Å barrier sample; triangles – the 150 Å barrier sample; solid lines – calculated values for the bandgap of InGaAsP bulk alloy. 110
4.5 Plot of the ratio of the well-to-barrier PL intensities versus temperature. Circles – the 150 Å barrier sample; triangles – the 80 Å barrier sample. 111
4.6 InGaAsP/InP MQW Photoluminescence at 0 V bias (dotted) and -1.0 V bias (solid, x25 magnified). 112
4.7 QW and barrier PL peak intensities versus applied voltage bias. 113
4.8 A plot of the photocurrent density versus excitation energy for InGaAsP MQW samples. The "80 Å" curve is shifted down for better view. 114
4.9 A plot of the normalized QW PC intensity versus temperature. 115
4.10 Dark current density for the InGaAsP MQW samples at room temperature. Thick line – the 150 Å barrier sample; thin line – the 80 Å barrier sample. . . 117

4.11 Temperature dependence of the dark current density for the InGaAsP MQW sample with a barrier thickness of 80 Å. 118

4.12 Calculated conduction band diagram and internal electric field distribution for InGaAsP/InP MQW samples. Dotted line – #381 sample (150 Å), solid line – #382 sample (80 Å). E_c is the conduction band edge, F is the internal field. 119

4.13 Calculated effect of the bias on the total recombination rate in the InGaAsP/InP MQW sample. 120

4.14 Effect of the strain on the band edges of InGaAsP. ΔE_c is the conduction band offset in unstrained InGaAsP, δE_c is the shift of the InGaAsP conduction band edge due to the strain, δE_{hh} and E_{lh} are the shifts of heavy and light hole valence band edges, respectively. 121

4.15 Diagram of the InGaAsP quaternary alloy showing lattice-matched composition and the composition of compressive and tensile strain 123

4.16 Calculated escape rates $1/\tau$ (solid lines) and experimental photocurrent (circles). All curves were normalized to their respective values at room temperature. (a) sample 381 (150 Å barrier), (b) sample 382 (80 Å barrier). 127

5.1 Conduction band edge diagram of the $\mathrm{In}_{1-x}\mathrm{Ga}_x\mathrm{As}_{1-y}\mathrm{P}_y$/InP MQW solar cell sample. Shown is a part of the MQW layer. 130

5.2 The photovoltaic conversion efficiency of InAs/InGaAs and GaAs/AlGaAs MQW solar cell 133

5.3 Calculated photovoltaic parameters of the ideal InP-based quantum well solar cell plotted vs QW-base bandgap difference: (a) – η the photovoltaic conversion efficiency, (b) – J_{sc} short-circuit current density, (c) – V_{oc} open circuit voltage. 136

5.4 Calculated relative increase in photovoltaic efficiency $\eta^R = \eta^{QW} - \eta^{base}$ vs QW-base bandgap difference for different values of γ_B. 137

5.5 Multiple quantum well structures with the resonant tunneling alignment: (a) – non-sequential, (b) – sequential 139
5.6 Layer diagrams of (a) the $In_{1-x}Ga_xAs_{1-y}P_y$/InP MQW and (b) InP control solar cell samples. 140
5.7 Design of the top grid contact for InGaAsP MQW solar cells: (a) top view of rectangular grid, $2S$ is the distance between the fingers, D is the distance between the busbars, and W_f is the finger width; (b) side view of the cell with the current flow. 141
5.8 Photovoltaic efficiency of the InGaAsP/InP MQW and InP solar cell samples vs. the white light illumination intensity. 145
5.9 Transmission of the MQW and control samples. The inset shows difference. Solid line – MQW; dotted line – control. 146
5.10 Reflectivity of the MQW and control samples. The inset shows difference. Solid line – MQW; dotted line – control. 147
5.11 Photocurrent versus distance from the metal contact. The inset shows a experiment schematics. 148
5.12 Photoresponse curves of the InP (a) and MQW InGaAsP/InP (b) solar cell samples exposed to H_2O_2:HBr:H_2O (1:1:25) etching solution. Dotted lines are the start (no etching done), dashed lines are after 2 min etching, solid lines are after 10 min etching. 149
5.13 Solar cell efficiency vs emitter (top layer) thickness. 151
5.14 Photoresponse (photocurrent vs. excitation wavelength) and photoluminescence intensities of the InGaAsP/InP MQW and InP solar cell samples at zero bias. InP PL peaks are 15 times magnified. 152

5.15 Photoluminescence (a) and photocurrent (b) intensities of InGaAsP/InP and InP solar cell samples vs. voltage bias measured at the fixed wavelengths: $\lambda = 920$ nm for the control sample, and $\lambda = 1300$ and 920 nm for the MQW sample. 920 nm PL is 20 times magnified. 1300 nm PL is 5 times magnified. The insert shows the dark current of the MQW sample. V_1 and V_2 are cutoff voltages (see text for the explanation). 154

6.1 Non-sequential resonant tunneling arrangement in MQW heterostructure. . 160

6.2 Sequential resonant tunneling transfer in an MQW structure. E_1 and E_2 are the energies of the ground and first excited states in the quantum well, respectively, d the superlattice period, and $\vec{F}$ the internal field. (a) – the structure is in a resonance, $F = F_{res}$; (b) – the structure is out of resonance, $F \neq F_{res}$. 161

6.3 Graphical solution of the equation $E_2 - E_1 = |q\vec{F}d|$. Squares show the calculated difference $E_2 - E_1$, where E_1 and E_2 are the energies of the ground and first excited states in the quantum well (the dashed line is the interpolating polynomial); the solid straight lines are $qF(w+b)$ for different values of barrier width; the horizontal line is drawn to mark the $\Delta E = 35$ meV boundary. The open circle marks the intersection 140Å well and 60 Å barrier chosen as "resonant" values for our sample. 164

6.4 Photoresponse of the InGaAsP/InP MQW sample at 77 K measured at different bias voltage. 168

6.5 Evolution of the PC features with the bias: second derivative of the InGaAsP/InP MQW sample at 77 K measured at different voltage bias. Dotted lines are drawn to show changes in PC peak positions due to the QCSE (Stark Effect). +0.7 and +0.9 V curves are in the "resonant" range 169

6.6 Photocurrent peak positions vs voltage bias for the InGaAsP/InP MQW sample at 77K. 171

6.7 Temperature dependence of the dark current in the $In_{1-x}Ga_xAs_{1-y}P_y$/InP MQW sample. The plots were taken at $\Delta T \approx 20$ K intervals. The inset shows the 77 K curve after subtracting a fitted exponential background. . . 172

6.8 Bias dependence of the photocurrent at 77 K. The detection wavelengths were fixed at the $E_1 \rightarrow HH_1$, $E_1 \rightarrow LH_1$, and $E_2 \rightarrow HH_2$ transitions. The inset shows $E_1 \rightarrow HH_1$ curve after eliminating a linear background. 173

6.9 Temperature dependence of PL intensity vs. bias. For each PL(V) curve, the detection system was fixed at the PL maximum. The plots were taken at $\Delta T \approx 20$ K intervals. 174

6.10 Integrated QW PC versus temperature measured at different biases. 176

6.11 InP-related electric fields (from FKO) as a function of *dc* bias for control (squares) and MQW (circles) samples. Lines are fits to a linear function. Electric field is found to vary linearly with a slope coefficient of 30. 178

6.12 SIMS profiles of the InP control sample. 179

6.13 SIMS profiles of the InGaAsP/InP MQW sample. 180

6.14 Calculated concentration of ionized impurity atoms (Zn) in InP as a function of temperature. Activation energy $E_{ac} = 46$ meV 181

6.15 Calculated band diagram of the MQW InGaAsP/InP sample at different concentration of ionized impurity atoms inside the intrinsic layer. 183

6.16 Calculated field distribution inside the intrinsic layer of the MQW InGaAsP/InP sample at different concentration of ionized impurity atoms. 184

7.1 Response characteristic of the proposed SRT electro-optical modulator. The peak in the current corresponds to the situation when the incident light power is exactly the one needed to put the device in resonant condition (causes the wells to be "resonantly" aligned). 188

7.2 *p-i-n* $CuInSe_2$/CdS solar cell structure with graded bandgap *i*-layer 191

7.3 Band diagram of a solar cell structure with an intermediate band. Arrows denote possible transitions between bands. 193

A.1 Piecewise potential used to calculate quantum well eigenstates and eigenfunctions. V_{bar} - barrier height, W_{well} - well width, W_{bar} - barrier width. . . 195

A.2 Logarithmic plot of the calculated transmission coefficient for the InGaAsP/InP double barrier heterostructure. 197

List of Tables

2.1 The eigenfunctions and eigenvalues of the Kane Hamiltonian 20

2.2 Selection rules for intraband transitions in a semiconductor quantum well. q is the propagation vector, z is the growth axis. 28

2.3 Selection rules for interband transitions in a semiconductor quantum well. $\Pi = \frac{-i}{m_0}\langle S|p_x|X\rangle = \frac{-i}{m_0}\langle S|p_y|Y\rangle = \frac{-i}{m_0}\langle S|p_z|Z\rangle$, q is the propagation vector, z is the growth axis. 29

2.4 Material parameters related to elastic properties of InAs, InP and GaAs. . . 35

3.1 Specifications of the TRIAX 320 spectrometer 87

4.1 Material parameters of GaAs, GaP, InAs, InP and $In_{0.532}Ga_{0.486}As$. m_e^*, m_{lh}^* and m_{hh}^* are effective masses (given in free electron mass m_0 units) for electrons, light holes and heavy holes, respectively. 123

4.2 InGaAsP alloy (1.3 μm – strained, 1.1 μm – unstrained)parameters used in calculations. z is the composition parameter, ΔE_c, ΔE_{hh} andΔE_{lh} are the conduction, heavy hole and light hole band offsets, respectively, m_e,m_{lh} and m_{hh} their corresponding effective masses. 124

4.3 Calculated and experimentally measured energies of the optical interband transitions in InGaAsP/InP MQW samples 125

5.1 Parameters of the InGaAsP/InP MQW and control InP solar cell samples as measured under 100 mW/cm^2 illumination of the QHT lamp ($T_{col} \simeq 3000^\circ$ K). 143

6.1 A list of energy values of prominent features in PC spectra together with calculated values of quantum well states. $T = 77\ K,\ V_{bias} = 0.3\ V$. 170

B.1 A list of GPIB-controlled devices used by the "Ke236.exe" and their addresses 199

Chapter 1

Introduction

1.1 Historical Background On Multiple Quantum Well Structures And Solar Cells

In 1969, Esaki and Tsu [1] were first to propose an artificially made semiconductor superlattice (SL) with a one-dimensional periodic potential. Two kinds of superlattice structures were suggested: one based on the periodic changing in doping concentration, and another one based on a periodic changes in composition. At that time superlattice structures presented a real challenge for existing semiconductor growth methods. The observation of the quantum effects in the superlattice is only possible if the characteristic parameter of the SL (SL period) is less than the phase-coherent length, and the latter is directly related to the quality of the crystal and the quality of the heterostructure interfaces. However the demand for high quality semiconductor thin films has initiated rapid development of various growth techniques. In 1974, five years later, Chung, Esaki and Tsu [2] reported on the first observation of *negative differential resistance* (NDR) in the current-voltage characteristic of the superlattice diode. That was a pure quantum effect predicted for this kind of microstructure. Thus, the possibility of creating a low-dimensional structure had had been experimentally proved.

Multiple quantum well (MQW) semiconductor heterostructures have attracted a considerable theoretical and experimental research interest. A proliferation of MQW devices has been made possible with invention and development of advanced growth techniques such as molecular beam epitaxy (MBE) and metalorganic chemical vapor deposition (MOVPE). These techniques allow to grow structures with atomically abrupt interfaces and precisely controlled compositional and doping parameters on the scale of a few angstroms (Å). For the last two decades MQW-based structures have created a foundation for new generations of infrared (IR) photodetectors, semiconductor lasers, electro-optical modulators and, recently, quantum well solar cells (QWSC).

A large number of available compatible materials has led to what J. M. Woodall [3,4] called "Band-Gap Engineering", a new concept in building opto-electronic devices. By changing compositional and doping parameters during growth, engineers can artificially "tailor" the fundamental parameters of the devices (i.e. mobility, bandgap, effective mass) to suit their specific needs.

Ever since the manufacturing of the first Si *p-n* junction diodes, semiconductor based solar cells were in constant development. Continuous improvements in semiconductor technology, in particular, Si technology, has led to considerable increases in solar cell photovoltaic conversion efficiency, a figure of merit used to characterize solar cell performance. The current best-performing solar cell efficiency (24%) has almost reached the theoretical limit for Si-based solar cells. Further advancements in efficiency required new ideas and new materials.

In order to make a better solar cell one has to consider what limits solar cell efficiency. The factors affecting SC performance can be divided into two somewhat overlapping categories. The first group is related to the sample quality and depends on a particular growth technique/process and on control over such parameters as layer thickness, doping concentration and distribution, and contact quality. The second group describes factors inherent to any photovoltaic device. This group relates to the fundamental physical processes affecting the photovoltaic conversion: carrier recombination, transport, and photon absorption.

Both groups are equally important in terms of their effect on the device's performance. Let us briefly outline the most important factors.

- The first and most important fundamental limitation imposed by a single-band solar cell device is that all photons with energy $\hbar\omega$ below energy gap E_{gap} are not absorbed.
- The second loss happens because of the very rapid relaxation of carriers towards their respective band edges. Thus all energy in excess of E_{gap} is lost to the heat.
- Radiative recombination of the photogenerated carriers is responsible for the third kind of loss as it reduces the number of electron-hole pairs. Radiative current subtracts from the total current delivered to the load by the cell.
- For a non ideal device, one must consider various non-radiative recombination losses due to contact resistance, impurities, interface roughness and so on.

High conversion efficiency requires both high current and high voltage. However, the reduction of the energy gap produces not only the increase in photocurrent but also a reduction in voltage, due to decreasing of the potential energy of collected carriers. Increasing the bandgap produces a gain in the voltage but a loss in the photocurrent. This situation can be resolved if one can build a solar cell which performs well not only in one particular point of the solar spectrum but in many points. In this way, the absorption spectrum of the cell will be a closer match to the solar spectrum. Thus, the concept of a *multiple bandgap solar cell* was born [5].

The idea was to create a vertical stack of several solar cells with different bandgaps, which made it possible for better utilization of the solar spectrum. This had required: (a) an epitaxial growth of semiconductor thin films of very different composition, (b) means to efficiently (without electric losses) connect the constituent subcells, and (c) to achieve optimum efficiency, the constituent subcells must be current matched to each other. This was a difficult task, and earlier multiband solar cells did not perform as well as it was expected from them.

Initial difficulties with fabricating high efficiency multiband solar cells has resulted in the emergence of a new approach to the problem. In 1990, Barnham and Duggan [6] have proposed to use MQW structures in high efficiency multi bandgap solar cells, to overcome difficulties associated with making lossless interconnections between subcells. Shortly after their proposal, this group experimentally demonstrated [7] that the photovoltaic conversion efficiency of *p-i-n* AlGaAs/GaAs photodiodes can be enhanced as much as 100% by inserting quantum wells in the intrinsic region. The insertion of quantum wells has extended the lower part of the cell's absorption spectrum resulting in an additional carrier generation and increase in a photocurrent.

Thus it has been established experimentally that quantum wells can increase the photovoltaic conversion efficiency for wide bandgap materials (AlGaAs/GaAs), however for materials with a bandgap closer to the optimum the results were rather disappointing. For instance, for InP/InGaAs cells several authors reported [8,9] *a decrease* in the efficiency compared to a control (non-MQW) sample. Anderson and Wojtczuk [9] explained the observed decrease by increased recombination on impurities, which effectively eliminated all advantage of MQW inclusion. To this date the best efficiency reported for QWSCs is an AlGaAs/GaAs 50 quantum well device with a 14% efficiency [10].

The choice of well/barrier combination seems to be a significant factor too. In 1994, Mohaidat *et al.* [11] theoretically investigated the dependence of the MQW solar cell efficiency on the barrier potential (band offset) under resonant tunneling conditions. It was found that the small bandgap ($InAs/In_{1-x}Ga_xAs$) MQW structure has a pronounced maximum at about 450 meV, while the efficiency declines linearly with the barrier potential increase for the larger bandgap ($GaAs/Al_xGa_{1-x}As$) structures.

The main positive effect of the MQW region is the extension of the cell's absorption spectrum. However, it is not enough to produce an enhancement of efficiency. Prompt collection of the photoexcited carriers is another key ingredient of the high efficiency. This is a weak point of the MQW solar cells. It is well known that the radiative recombination rate in quantum well structures is significantly larger than that in similar non-QW structures due to spatial localization of the carriers. Although it is beneficial for light-emitting devices such as lasers and LEDs, it is a disadvantage for solar cells due to reduction of the photogenerated current. Characteristic feature of the QW is that it acts as a carrier trap and so to guarantee an efficient operation one must provide means for efficient carrier escape and collection. Nelson *et al.* [12] have concluded that in a moderate quality quantum well with non-radiative recombination time $\tau_{nr} \geq 1$ ns, most photogenerated carriers will escape the wells via thermionic emission at room temperature. The issue of efficient escape, becomes critical in the deep-well systems (InP/InGaAs(P)), where second escape channel – tunneling – is more important.

Another positive aspect of the QWSC - better temperature dependence (less susceptible to temperature changes) than conventional cell was reported by Ballard *et al* [13]. It can be important for cells operating in a harsh environment.

Theoretical analysis [5] shows that to produce a sizeable increase of the photovoltaic efficiency in the two-gap or MQW solar cell over single bandgap devices, the difference in the bandgaps of constituent materials must be > 0.5 eV. In this case an ideal two gap cell can reach 50% of efficiency against 37% for the single gap cell. This analysis suggested that so-called "deep-well" systems such as InGaAs(P)/InP, where the aforementioned difference is about 0.6 eV, may have an advantage over the AlGaAs/GaAs material system, where this difference is less than 0.4 eV. Besides an advantage of larger bandgap difference the InGaAs(P)/InP-based solar cells exhibit higher radiation resistance compared to the GaAs-based cells which is important for extraterrestrial applications.

These developments presented several problems that need to be answered:

1. What physical factors influence performance of MQW-based solar cells most?
2. Is it possible to make an MQW InP-based solar cell which will outperform a conventional (non-MQW) solar cell?
3. Can the recombination losses specific to MQW devices be reduced?

My thesis will attempt to answer these questions.

This requires an understanding of physical mechanisms responsible for generating photocurrent in solar cells, and, in particular, mechanisms, specific to the MQW devices. An efficient escape and transport of the photoexcited carriers across the MQW region will largely determine the performance of an MQW device. The carrier escape mechanisms fall into several categories: thermionic emission of carriers above the barrier, a process which depends primarily on barrier height and temperature; tunneling out of the well, which exponentially depends on barrier width; escape via an absorption of optical phonons, a process which is affected by temperature, and the combination of the last two (phonon-assisted tunneling) [14].

Escape processes are competing against radiative and non-radiative recombination which tends to diminish the photocurrent. Fig. 1.1 shows a schematic diagram of these processes in a quantum well. All these mechanisms depend on structural and compositional parameters of the MQW structures. External factors, such as voltage bias and temperature variations, are other important parameters which can influence escape process.

As was mentioned before, in order to extend solar cell's absorption range, the difference between barrier and well bandgaps should be made large (> 0.5 eV). However, it contradicts with a requirement of having high escape rates, because, the deeper the well the harder for carriers to escape. To enhance carrier collection rate and reduce recombination losses one can implement *resonant tunneling* transfer inside the MQW structure. In resonantly coupled wells, the electron transfer time between adjacent wells is reduced by several orders of magnitude, which can produce a large amplification of the photocur-

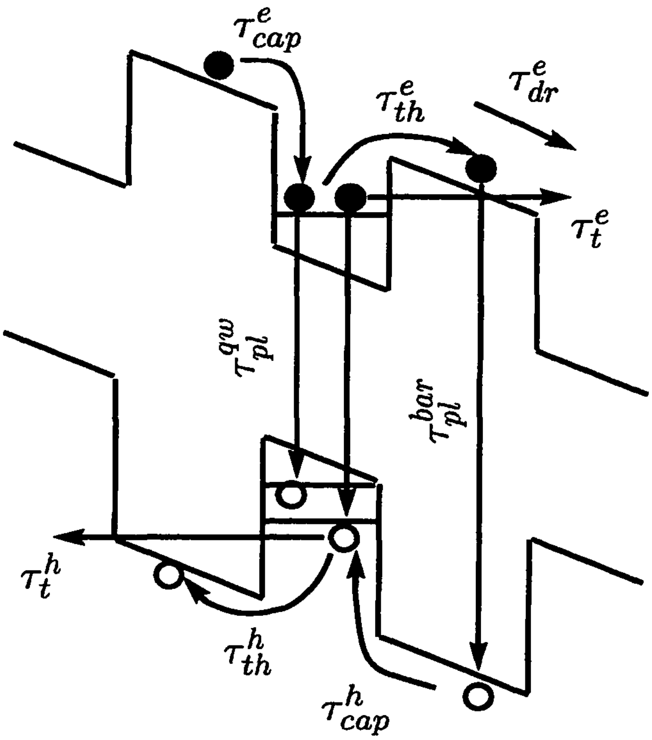

Figure 1.1: Free carrier escape and transfer processes in the MQW structure. The τ's are different characteristic times associated with these processes: τ_t is the tunneling escape time, τ_{th} is the thermionic escape time, τ_{cap} is the capture time, τ_{dr} is the drift time, and τ_{pl} is radiative recombination time; indices e and h refer to electrons and holes, respectively.

rent [15]. In 1990, Barnham and Duggan (B&D) [6] suggested a resonant tunneling structure for efficient carrier collection in MQW solar cells as shown in Fig. 1.2a. Resonantly enhanced photocurrent in the MQW structures was observed by several groups [16,17] in GaAs/AlAs MQW samples. Summers *et al.* [18] have reported on the observation of negative differential resistance in resonantly aligned three well AlGaAs/GaAs structure, in what they called "variably spaced superlattice energy filter". To the best of our knowledge, this was the only experimental work where the resonant MQW structure with variable well width and number of wells more than two was investigated.

The major problem with this kind of structure is that the total number of QWs, which can be simultaneously aligned in resonance with each other, is limited to 5-6. That corresponds to the ~0.1 μm thickness of the intrinsic layer and it is not acceptable for photovoltaic devices due to the low absorption. To compensate for low absorption B&D suggested to add several *not-in-resonance* wells to the end of the MQW stack. In my opinion, it defeats the whole purpose of having resonant tunneling transfer in the first place. After passing through the first "resonant" region carrier will tend to accumulate in the region with slow transfer capabilities. One could overcome insufficient thickness by putting together several lattice-matched materials, e.g., II–VI and III–V group semiconductors. However at the current state of semiconductor growth, it is difficult to combine more than three lattice-matched materials.

To overcome this deficiency we have proposed an MQW solar cell with a sequential resonant tunneling.

Sequential resonant alignment shown in Fig. 1.2b appears to be free of thickness limitations. The sequential resonant tunneling happens if the following condition is satisfied: $E_{e2} - E_{e1} = |q\vec{F}d|$, where E_{e1} and E_{e2} are the ground and first excited subband energies of the quantum well, q – the electron charge, $\vec{F}$ – the internal electric field, and d – the MQW spatial period. In this thesis we propose to utilize *sequential resonant tunneling* (SRT) in MQW solar cells.

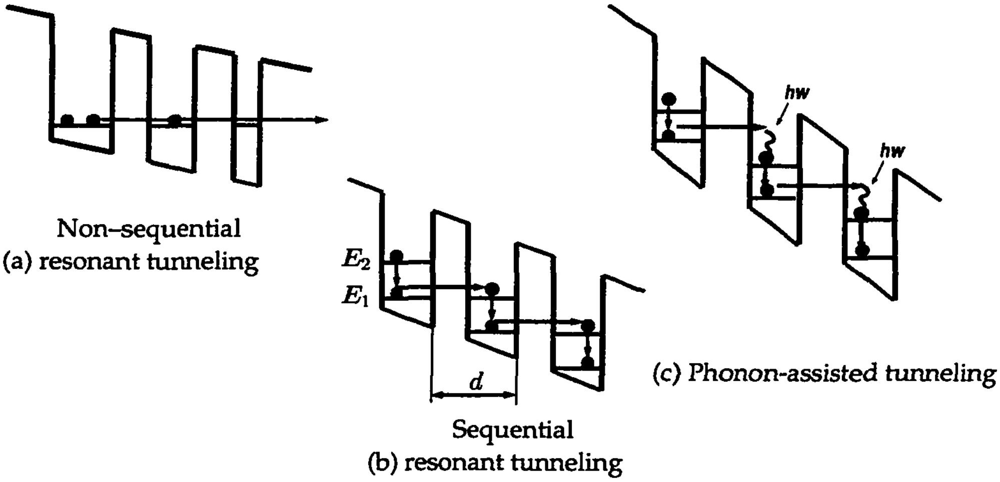

Non–sequential
(a) resonant tunneling

Sequential
(b) resonant tunneling

(c) Phonon-assisted tunneling

Figure 1.2: Multiple quantum well structures with the different tunneling alignments: (a) – non-sequential process, (b) – sequential process, (c) – phonon-assisted tunneling.

Electron-phonon interaction can be responsible for so-called *phonon-assisted tunneling* shown in Fig. 1.2c. When the difference between the final and initial state are comparable to an optical phonon energy $\hbar\omega_{LO}$ ($\Delta E_{i\rightarrow f} = E_f - E_i \approx \hbar\omega_{LO}$), and if the phonon-assisted tunneling rate is larger than other escape processes, then an increase in tunneling rate can be observed when the $\Delta E_{i\rightarrow f}$ exceeds $\hbar\omega_{LO}$, i.e. phonon absorption becomes allowed.

Investigation of the MQW solar cells with a built-in SRT requires reliable experimental methods which can provide information about device structure, carrier escape and transport, recombination losses. Steady-state photoluminescence (PL) and photocurrent (or photoconductivity) (PC) measurements are widely acceptable methods and they can provide required information. Each technique is complementary to another in a sense that the photoluminescence and photoconductivity are essentially competing processes — certain gain in the PL intensity may produce corresponding loss in the PC amplitude and vice versa. Along with the standard PL and PC measurements where intensity is measured as a function of exciting or emitted wavelength, we have extended these methods to make it possible to measure the intensities as a function of applied bias. This allow us to control the internal electric field and study the effects of the field variation on the PC and PL intensities. Information obtained with the help of additional techniques (Electroreflectance and Secondary Ion Mass Spectrometry) was used to get dopant concentration profiles and the value of electric field inside the sample.

Steady-state measurements can provide only very indirect information on the dynamics of the transport. Time-resolved techniques are required for the direct study of the transport process. Progress in the ultrafast spectroscopy for the last decade has offered "the possibility of studying and discovering key processes unresolved in the pass" [19]. Ultrafast laser spectroscopy was particularly successful in investigating tunneling phenomena in MQW heterostructures by measuring photoluminescence decay times. Throughout this work we have relied on the experimental results obtained by several groups [20–23].

1.2 Thesis Organization

The thesis is divided into seven chapters.

The first chapter, "Introduction", contains a brief historical introduction into the subject of quantum well solar cells. It gives major accomplishments and the current developments in this field. The rest of the chapter presents thesis outline and thesis statement.

The second chapter, "Theoretical background", provides a theoretical description of semiconductor MQW heterostructures. It starts with a description of the *envelope function approximation* (EFA). Using this approximation optical properties of quantum well heterostructures are then outlined. The effect of the strain and electric field (Quantum Confined Stark Effect) on these properties is also presented. A separate section gives physical principles of photovoltaic conversion and the main factors which limit the efficiency of common solar cells. The section on MQW solar cells presents a model of an ideal QW solar cell. The chapter ends with a description of a numerical solution of Poisson's equation in semiconductor heterostructures.

The third chapter, "Experimental setup", describes photoluminescence and photocurrent measurement systems, their major components and specifications. Separate section presents "Ke236" – a software developed to conduct data acquisition and to control various instrument functions. The rest of the chapter describes sample growth and preparation.

The next three chapters contain my original research work conducted on various InGaAsP/InP semiconductor heterostructures.

In fourth chapter, "Investigation of photoluminescence and photocurrent in $In_xGa_{1-x}As_yP_{1-y}$ strained MQW heterostructures", we present our studies on the photoluminescent and photoconductive properties of the MQW InGaAsP/InP *p-i-n* heterostructures. Two samples with the same well thickness and different barrier width were investigated using photoluminescence, photocurrent and dark current measurements. The focus of the study is the basic properties of the MQW structures: quantum well energy states, the effect of the strain, temperature and electric field on these states, and the escape processes in quantum wells. The origin of recombination losses is analyzed. The relation of the quantum well electronic properties with structural and compositional parameters of heterostructures is also a subject of investigation as it is important for understanding of basic physics of MQW devices.

The fifth chapter, "Investigation of the $In_xGa_{1-x}As_yP_{1-y}$ multiple quantum well solar cell structures", presents a study of InGaAsP/InP MQW solar cell structures. Two samples, with MQW layer and without it, were designed, grown and investigated. The design of the MQW cell facilitated transport and increased the collection rates of the photogenerated carriers in the MQW region, in which the well and barrier widths were chosen to permit a *sequential resonant tunneling* between adjacent wells [15]. An increase of 13% in photovoltaic efficiency for the MQW device was observed over the control sample. Photocurrent and photoluminescence spectra measured at the different bias and excitation wavelengths were used to investigate carrier escape and recombination processes. The chapter concludes with a discussion of possible ways to further improve the photovoltaic efficiency.

The sixth chapter, "Resonant enhancement of the photocurrent in MQW photovoltaic devices", deals with an investigation of resonant enhancement of photocurrent in the InGaAsP/InP MQW samples. The evidence of the resonant transfer was observed in photoluminescence, photocurrent and dark current measurements. Full characterization of samples including identification of quantum well states was conducted using photoluminescence and photocurrent spectroscopies. Besides photoluminescence and photocurrent measurements, additional experimental techniques were used to investigate dopant profiles and electric field distribution in the *i*-region in the samples: *electroreflectance* spectroscopy (ER) and *secondary ion mass spectrometry* (SIMS). The criteria for successful implementation of SRT in the MQW photovoltaic devices are given.

The last chapter gives a thesis summary and discusses future developments in this field.

1.3 Thesis Statement

This thesis focuses on the physics of photovoltaic conversion in InP-based MQW semiconductor heterostructures. A new idea of improving collection of the photo-induced carriers and to enhance photovoltaic conversion efficiency of the MQW solar cell devices by using sequential resonant tunneling transfer (SRT) is investigated. Based on this new concept InGaAsP/InP MQW samples were designed, grown and investigated. Enhancement of the photocurrent in the InGaAsP/InP MQW heterostructure due to a built-in SRT has been observed for the first time.

The following major objectives were focused on in this thesis:

- Several InGaAsP/InP MQW and bulk InP samples were designed and investigated. Quantum well subbands were identified and matched with calculated results. The effect of the temperature and voltage bias was used to identify dominant escape mechanism in these structures.

- A new InGaAsP/InP MQW solar cell design was investigated. Measurements of the photovoltaic efficiency in InGaAsP/InP clearly demonstrated that the MQW sample outperformed the control InP (bulk) sample by an 13%.
- Investigation of the SRT transfer in InGaAsP/InP MQW sample has shown that the SRT does reduce radiative recombination losses and can increase a collection rate of photogenerated carriers.
- The criteria for successful implementation of the SRT in MQW structures for the purpose of enhancement of photovoltaic efficiency have been established. The main requirements are low residual dopant concentration in the *i*-layer (less than $1 \times 10^{15}\ cm^{-3}$) and careful choice of "resonant" value of the bias, which must be within the operational range of the designed cell.
- It has been shown for several samples that voltage dependence of photoluminescence in *p-i-n* diodes can be used to identify the origin of PL in multilayer structures.
- The semiconductor characterization system incorporating an 0.3 m Triax Spectrometer, Stanford Research Lock-in Amplifier and Keithley Source-Measure Unit was built. Software utilizing GPIB interface was developed to perform data acquisition and control various instrumentation functions. The system allows to conduct photoluminescence, photocurrent, current-voltage and photovoltaic efficiency measurements in 20-300 K temperature range.

Chapter 2

Theoretical background

2.1 Introduction

This chapter describes the physics involved in semiconductor heterostructures and quantum well devices based on these structures. The envelope function approximation (EFA) is presented as a method to describe properties of the heterostructures. Based on the EFA optical properties of the MQW structures are described. The effect of the electric field and strain on the properties of the MQW is also discussed. Separate sections outline main characteristics of carrier escape and transport in the MQW, and special consideration is given to various scattering mechanisms affecting the transport. The principles of photovoltaic conversion are given. Brief introduction into theory of semiconductor *p-n* junction is followed by a discussion of the efficiency limitations of photovoltaic conversion. Multiband solar cell as a way to improve the efficiency of photovoltaic devices is considered in this chapter. MQW solar cell is presented as a particular realization of the multiband solar cell. The chapter concludes with the description of the model of ideal solar cell.

2.2 Quantum Well Semiconductor Heterostructures

Advances in the semiconductor growth techniques such as molecular beam epitaxy (MBE) and metal-organic chemical vapor deposition (MOVPE) helped to create a basis for the development of devices with characteristic sizes of a few nanometers and less, so called *nanostructures*. An interest to these structures comes from the fact their electronic and vibrational properties are modified as a result of quantum confinement. These changes can be relatively easy controlled by changing device parameters such as layer thickness and stoichiometry. Combining layers of two different materials requires matching of their *lattice constants*. When these constants are identical or very close, it is easier to align A atoms with B atoms and produce sharp A/B interface. There are only few semiconductor materials which can be grown lattice-matched. Fig. 2.1 shows a plot of the bandgaps of different semiconductors versus their lattice constants. The solid lines are joining semiconductors which can form stable alloys.

A typical example of the nanostructure is a *quantum well* device shown in Fig. 2.2a. This kind of configuration is achieved by growing a thin layer (order of nanometers) of semiconductor B between two layers of semiconductor A. The bandgap of B is less than the bandgap of A: $E^A_{gap} < E^B_{gap}$. Stacking together many QWs and barriers one can build so-called *superlattice* shown in Fig. 2.2b. The quantum well and superlattice are examples of two-dimensional nanostructures. Other structures with lower dimensionality were successfully grown and investigated – one-dimensional *quantum wires* and zero-dimensional *quantum dots*.

The next several sections are outlining analytical models used to describe MQW semiconductor heterostructures.

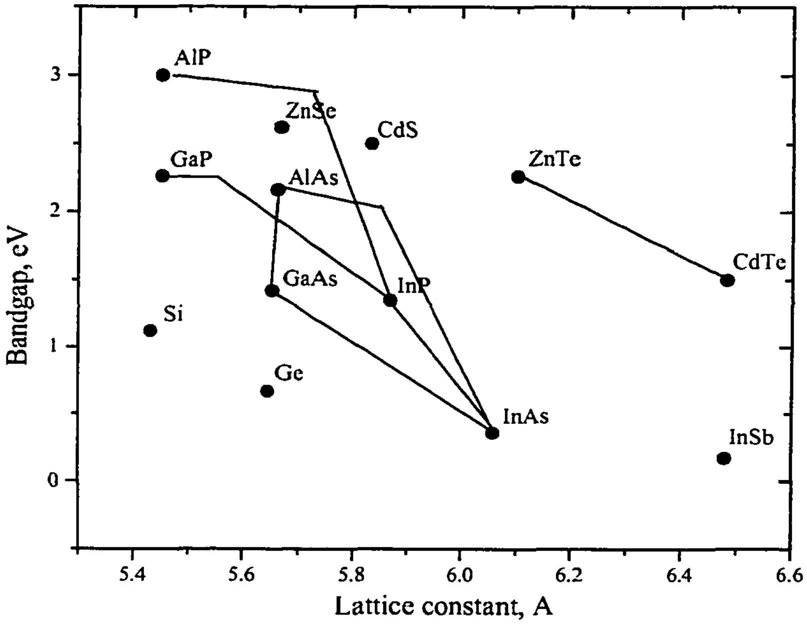

Figure 2.1: Room temperature energy bandgaps of several III-V and II-VI group semiconductors versus their lattice constants. The solid lines connect the semiconductors which can form stable alloys.

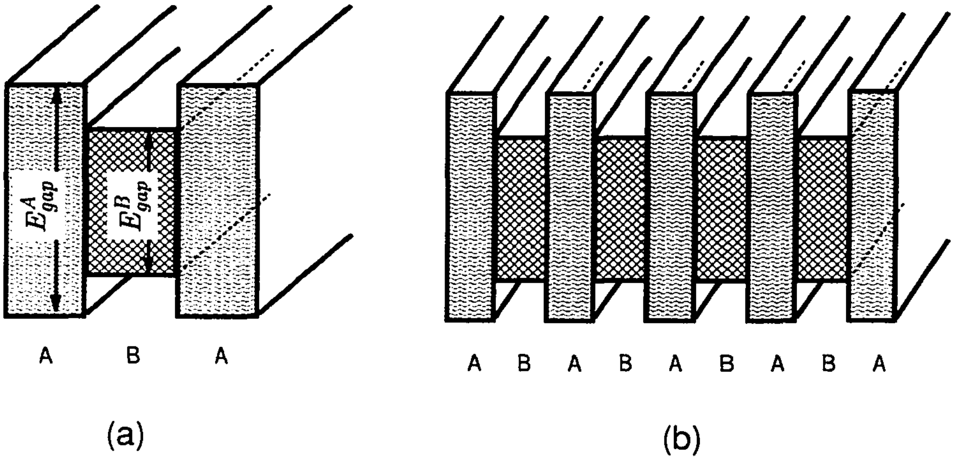

Figure 2.2: Examples of the nanostructures: (a) – a single quantum well, (b) – a superlattice.

2.2.1 The $k \cdot p$ Method of the Band Structure Description

The Schroedinger equation describing the motion of one electron in the crystal can be written as:

$$\mathcal{H}_{el}\Phi_n(\boldsymbol{r}) = \left(\frac{\boldsymbol{p}^2}{2m_0} + V_{ave}(\boldsymbol{r})\right)\Phi_n(\boldsymbol{r}) = E_n\Phi_n(\boldsymbol{r}) \tag{2.1}$$

where $\mathcal{H}_{el}$, $\Phi_n(\boldsymbol{r})$ and E_n denote, respectively, the one-electron Hamiltonian, the wavefunction and energy of an electron in an eigenstate n, $\boldsymbol{p}$ is the momentum operator of the electron and $-e$ is its charge. The $\boldsymbol{r}$ is the position of the electron in the crystal. It is assumed that every electron experiences the same average potential $V_{ave}(\boldsymbol{r})$, where $V_{ave}(\boldsymbol{r})$ is:

$$V_{ave}(\boldsymbol{r}) = \overline{\frac{1}{2}\sum_{i}^{N_{el}} \frac{e^2}{|\boldsymbol{r} - \boldsymbol{r}_i|} + \sum_{j}^{N_{at}} \frac{Z_j e^2}{|\boldsymbol{r} - \boldsymbol{R}_{j0}|}} \tag{2.2}$$

where R_{j0} is the position of the j-th nucleus frozen in its equilibrium position, Z_j is the atomic number of the nucleus, and N_{at} and N_{el} are the numbers of nuclei and electrons, respectively.

According to quantum mechanics, the wavefunction of the particle moving in the periodic potential $V(\boldsymbol{r}) = V(\boldsymbol{r} + \boldsymbol{R}_j)$, $j = 1 \ldots N$, can be expressed in the form of *Bloch functions*:

$$\Phi_{nk}(\boldsymbol{r}) = \exp(i\boldsymbol{k} \cdot \boldsymbol{r})u_{nk}(\boldsymbol{r}) \tag{2.3}$$

where $u_k(\boldsymbol{r})$ is a periodic function with the same periodicity as $V(\boldsymbol{r})$, n is the index and k is the *wave vector* of the plane wave forming Bloch function. A plot of the electron energies in Eq. 2.1 versus k is referred as the *electronic band structure* of the crystal. After Φ_{nk} is substituted into Eq. 2.1 we can obtain an equation for u_{nk}:

$$\left(\frac{p^2}{2m_0} + \frac{\hbar\boldsymbol{k} \cdot \boldsymbol{p}}{2m_0} + \frac{\hbar^2 k^2}{2m_0} + V_{ave}\right)u_{nk} = E_{nk}u_{nk} \tag{2.4}$$

At $k_0 = (0,0,0)$, Eq. 2.4 reduces to:

$$\left(\frac{p^2}{2m_0} + V_{ave}\right) u_{nk0} = E_{nk0} u_{nk0} \tag{2.5}$$

Once E_{nk0} and u_{nk0} are found, $\hbar \boldsymbol{k} \cdot \boldsymbol{p}/2m_0$ and $\hbar^2 k^2/2m_0$ can be treated as perturbations using either degenerate or non-degenerate perturbation theory. This method of calculating the band structure is known as the $k \cdot p$ method.

In many cases the complete knowledge of crystal band structure is not required, since the electronic properties of semiconductors are governed by the electronic states that are in the close vicinity of the conduction band minimum and valence band maximum. Let us assume that at $E(k = k_0) = E_{n0}$ the band structure is non-degenerate, and it has an extremum at this point. Then, using standard perturbation theory, the eigenfunctions u_{nk} and eigenvalues E_{nk} near k_0 can be expressed in the terms of unperturbed u_{n0} and E_{n0} as [24]:

$$\begin{aligned} u_{nk} &= u_{nk0} + \frac{\hbar}{m_0} \sum_{n' \neq n} \frac{\langle u_{n0} | \boldsymbol{k} \cdot \boldsymbol{p} | u_{n'0} \rangle}{E_{n0} - E_{n'0}} u_{n'0} && \text{(2.6a)} \\ E_{nk} &= E_{n0} + \frac{\hbar^2 k^2}{2m_0} + \frac{\hbar^2}{m_0^2} \sum_{n' \neq n} \frac{|\langle u_{n0} | \boldsymbol{k} \cdot \boldsymbol{p} | u_{n'0} \rangle|^2}{E_{n0} - E_{n'0}} u_{n'0} && \text{(2.6b)} \end{aligned}$$

It is conventional to express the energy E_{nk} as:

$$E_{nk} = E_{n0} + \frac{\hbar^2 k^2}{2m^*} \tag{2.7}$$

where m^* is known as the effective mass of the band:

$$\frac{1}{m^*} = \frac{1}{m_0} + \frac{2}{m_0^2 k^2} \sum_{n' \neq n} \frac{|\langle u_{n0} | \boldsymbol{k} \cdot \boldsymbol{p} | u_{n'0} \rangle|^2}{E_{n0} - E_{n'0}} u_{n'0} \tag{2.8}$$

Kane Model of Dispersion Relations

Kane [25] took a different approach from the perturbative expansion of E_{nk} in terms of k. He noticed that in III–V semiconductors the topmost valence band and the lowest conduction band are close to each other and well separated from the bands. Thus Kane solved Eq. 2.4 *exactly* for a limited number of bands, and later introduced the coupling with other bands using second-order perturbation analysis.

From the group theory analysis of the band structure it is known that the conduction and valence band functions are s- and p-like, respectively, and can be denoted by $|S\rangle$ and $|X\rangle$, $|Y\rangle$ and $|Z\rangle$. The electron spin is 1/2 and will be noted by $\uparrow$ (spin-up state) and $\downarrow$ (spin-down state). From atomic physics, it is known that electron spin s can be coupled to the orbital angular momentum l via *spin-orbit interaction*. The spin-orbit interaction can expressed as:

$$\mathcal{H}_{so} = \lambda \boldsymbol{s} \cdot \boldsymbol{l} \tag{2.9}$$

where the constant λ is referred to as the *spin-orbit coupling*. The eigenfunctions of Eq. 2.9 are the eigenfunctions of the *total angular momentum* $\boldsymbol{j} = \boldsymbol{l} + \boldsymbol{s}$ and its z component j_z. For $l = 0$ (conduction band) there are two eigenstates ($j = s = \frac{1}{2}$, Γ_6 symmetry), and for $l = 1$ (valence band) there are six eigenstates: four for the $j_{3/2} = l + s = \frac{3}{2}$ (Γ_8 symmetry) and two for the $j_{1/2} = l - s = \frac{1}{2}$ (Γ_7 symmetry). In III–V group semiconductors the quadruplet $j_{3/2}$ is always higher in energy than the doublet $j_{1/2}$. Calculating the matrix elements of E_{nk} between these 8 Bloch functions and solving the secular equation the eigenvalues of the Eq. 2.4 can be found.

Table 2.1 lists the eigenfunctions and eigenenergies of the Kane Hamiltonian. The energy origin is chosen at the Γ_6 edge. The eigenenergies depend on three parameters: the fundamental bandgap ϵ_0, the spin-orbit coupling gap Δ, and the interband matrix element

u_l	$\lvert j, j_z\rangle$	ψ_{j,j_z}	$E_l(k=0)$
u_1	$\lvert\frac{1}{2},\frac{1}{2}\rangle$	$i\lvert S\uparrow\rangle$	0
u_2	$\lvert\frac{1}{2},-\frac{1}{2}\rangle$	$i\lvert S\downarrow\rangle$	0
u_3	$\lvert\frac{3}{2},\frac{1}{2}\rangle$	$-\sqrt{\frac{2}{3}}\lvert Z\uparrow\rangle+\frac{1}{\sqrt{5}}\lvert(X+iY)\downarrow\rangle$	$-\epsilon_0$
u_4	$\lvert\frac{3}{2},-\frac{1}{2}\rangle$	$-\sqrt{\frac{2}{3}}\lvert Z\downarrow\rangle-\frac{1}{\sqrt{5}}\lvert(X+iY)\uparrow\rangle$	$-\epsilon_0$
u_5	$\lvert\frac{3}{2},\frac{3}{2}\rangle$	$\frac{1}{\sqrt{2}}\lvert(X+iY)\uparrow\rangle$	$-\epsilon_0$
u_6	$\lvert\frac{3}{2},-\frac{3}{2}\rangle$	$\frac{1}{\sqrt{2}}\lvert(X-iY)\downarrow\rangle$	$-\epsilon_0$
u_7	$\lvert\frac{1}{2},\frac{1}{2}\rangle$	$\frac{1}{\sqrt{3}}\lvert Z\uparrow\rangle+\frac{1}{\sqrt{3}}\lvert(X+iY)\downarrow\rangle$	$-\epsilon_0-\Delta$
u_8	$\lvert\frac{1}{2},-\frac{1}{2}\rangle$	$\frac{1}{\sqrt{3}}\lvert Z\downarrow\rangle-\frac{1}{\sqrt{3}}\lvert(X-iY)\uparrow\rangle$	$-\epsilon_0-\Delta$

Table 2.1: The eigenfunctions and eigenvalues of the Kane Hamiltonian

of the momentum operator:

$$P = -\frac{i}{m_0}\langle S|p_x|X\rangle = -\frac{i}{m_0}\langle S|p_y|Y\rangle = -\frac{i}{m_0}\langle S|p_z|Z\rangle \tag{2.10}$$

All the other p matrix elements vanish by symmetry.

Band Edge Effective Masses

If $k \parallel j \parallel \hat{z}$ and $k = (0, 0, k_z)$, the dispersion relations can simply be obtained, and $j_z = \pm 1/2$ and $j_z = \pm 3/2$ bands remains decoupled. For the band edges ($k \rightarrow 0$) the effective masses can be expressed in terms of band structure parameters ϵ_0, Δ and P:

$j_z = \pm 1/2$: these states are usually associated with light particles.

$$\frac{1}{m_{\Gamma_6}} = \frac{1}{m_0} + \frac{4P^2}{3\epsilon_0} + \frac{2P^2}{3(\epsilon_0+\Delta)} \qquad \text{electrons} \tag{2.11a}$$

$$\frac{1}{m_{\Gamma_8^{lh}}} = \frac{1}{m_0} - \frac{4P^2}{3\epsilon_0} \qquad \text{light holes} \tag{2.11b}$$

$$\frac{1}{m_{\Gamma_7}} = \frac{1}{m_0} - \frac{2P^2}{3(\epsilon_0+\Delta)} \qquad \Gamma_7 \text{ holes} \tag{2.11c}$$

$j_z = \pm 3/2$: these states are usually associated with heavy hole particles. To get a dispersion for the heavy holes, one has to include coupling with the remote bands besides Γ_6, Γ_7 and Γ_8:

$$\frac{1}{m_{\Gamma_8^{hh}}} = -\frac{1}{m_0} + \frac{2}{m_0^2} \sum_{l \neq \Gamma_{6,7,8}} \frac{\left| \langle \frac{3}{2}, \pm\frac{3}{2} | p_z | u_l \rangle \right|^2}{\epsilon_l + \epsilon_0} \tag{2.12}$$

2.2.2 Envelope Function Approximation

The common approach to the description of electron states in a quantum well is based on *an envelope function approximation* (EFA) [26]. The key assumptions of this approach are:

- The band offsets are usually a small fraction of the host bandwidths.
- The band structures of the host layers are usually very similar.

The first assumption means that the conduction band edge of semiconductor A will line up with the conduction band edge of semiconductor B within ≈1 eV range or, more generally, $\Delta E_{gap}^{AB} < E_{gap}^{B}$, where $\Delta E_{gap}^{AB} = E_{gap}^{A} - E_{gap}^{B}$. The second assumption means that these two edges are of the same symmetry (e.g. Γ_6). Then the electronic states in both layers can be described in terms of $k \cdot p$ expansion around the Γ_6 point.

Inside each layer the total wavefunction can be expanded in terms of the periodic parts of the Bloch functions u_{lk_0} of the edges under consideration:

$$\Psi(\boldsymbol{r}) = \begin{cases} \sum_{l=1}^{8} u_{lk_0}^{A}(r)\Big[a_l(k_l^A)\exp(ik_l^A \cdot r) & + \quad b_l(k_l^A)\exp(-ik_l^A \cdot r)\Big], \\ & \text{for } (-L/2) < z < (L/2) \\ \sum_{l=1}^{8} u_{lk_0}^{B}(r)\Big[a_l(k_l^B)\exp(ik_l^B \cdot r) & + \quad b_l(k_l^B)\exp(-ik_l^B \cdot r)\Big], \\ & \text{for } z > (L/2) \text{ or } z < (-L/2) \end{cases} \tag{2.13}$$

Similarity of the A and B band structures implies that $u_{lk_0}^{A,B}$ are the same:

$$u_{lk_0}^{A} = u_{lk_0}^{B} \tag{2.14}$$

Let the growth axis to be the $\hat{z}$ axis and the plane $z = z_0$ to be the interface separating the A and B layers. Using translational invariance in the layer plane and assuming the same lattice constant in both semiconductors, $\Psi(\boldsymbol{r})$ can be factorized:

$$\Psi(\boldsymbol{r}) = \exp(i\boldsymbol{k}_\perp \cdot \boldsymbol{r}_\perp) \sum_{l=1}^{8} u_{lk_0}(\boldsymbol{r}) f_l^{A,B}(z) \tag{2.15}$$

where $\boldsymbol{k}_\perp$ and $\boldsymbol{r}_\perp$ are in-plane projections of $\boldsymbol{k}$ and $\boldsymbol{r}$ vectors, respectively, and $f_l^{A,B}(z)$ is an *envelope function* that is slowly varying on the scale of the host periodicity. The $f_l(z)$ are solutions of the coupled differential system:

$$\begin{aligned} &\left[\epsilon_l^A Y(z \in A) + \epsilon_l^B Y(z \in B) + V_{ext}(z) + \frac{\hbar^2 k_\perp^2}{2m_0} - \frac{\hbar^2}{2m_0}\frac{\partial^2}{\partial z^2}\right] f_l(z) \\ &+ \sum_{m=1}^{8} \left[\frac{\hbar \boldsymbol{k}_\perp}{m_0} \cdot \langle u_{lk_0} | \boldsymbol{p}_\perp | u_{mk_0} \rangle + \frac{1}{m_0} \cdot \langle u_{lk_0} | p_z | u_{mk_0} \rangle \frac{\hbar}{i}\frac{\partial}{\partial z}\right] f_m(z) = \epsilon f_l(z) \end{aligned} \tag{2.16}$$

where the u_{lk_0}, by definition, solutions of:

$$\begin{aligned} &\left[\frac{p^2}{2m_0} + V^A(\boldsymbol{r}) Y(z \in A) + V^B(\boldsymbol{r}) Y(z \in B)\right] u_{lk_0} \\ &\qquad = \left[\epsilon_l^A Y(z \in A) + \epsilon_l^B Y(z \in B)\right] u_{lk_0} \end{aligned} \tag{2.17}$$

and $Y(z)$ is a step function:

$$Y(z \in A) = \begin{cases} 1, & \text{for } z \text{ inside } A \text{ layer} \\ 0, & \text{for } z \text{ outside } A \text{ layer} \end{cases} \tag{2.18}$$

In Eq. 2.16 all explicit information about hosts periodic structure is *disappeared*, and it contains in the implicit form through effective parameters such as bandgaps and the Kane matrix elements.

The Ben Daniel-Duke Model

This model is the simplest form of the EFA and works for the lowest conduction band of several heterostructures. It takes into consideration only one parabolic band. The Eq. 2.16 simplifies to:

$$\left[-\frac{\hbar^2}{2m^*(z)}\frac{\partial^2}{\partial z^2}+\frac{\hbar^2 k_\perp^2}{2m^*(z)}+\epsilon_0+V(z)\right]f(z)=\epsilon f(z) \tag{2.19}$$

where m_z^* and Vz

$$m^*(z)=\left\{\begin{array}{ll} m^A, & \text{for } z\in A \text{ layer} \\ m^B, & \text{for } z\in B \text{ layer}\end{array}\right\} \tag{2.20}$$

$$V^*(z)=\left\{\begin{array}{ll} 0, & \text{for } z\in A \text{ layer} \\ V_0, & \text{for } z\in B \text{ layer}\end{array}\right\} \tag{2.21}$$

The boundary conditions on the A/B interface require continuity of the function $f(z)$ and $\frac{1}{m^*(z)}\frac{df}{dz}$ at $z = \pm(L/2)$. The second condition ensures that the particle flux is continuous across the interface. It can be seen that the problem was practically reduced to the quantum-mechanical problem of finding energy states of the particle in a quantum well. The bound state solutions are sought in the following form:

$$f_{even}(z)=\begin{cases} A\cos(k_z^A z), & \text{for } |z|\le\frac{L}{2} \\ Be^{-\kappa^B z}, & \text{for } z>\frac{L}{2} \\ Ce^{\kappa^B z}, & \text{for } z<-\frac{L}{2} \\ f_{even}(z)=f_{even}(-z) & \end{cases} \tag{2.22}$$

for even states, and

$$f_{odd}(z)=\begin{cases} A\sin(k_z^A z), & \text{for } |z|\le\frac{L}{2} \\ Be^{-\kappa^B z}, & \text{for } z>\frac{L}{2} \\ Ce^{\kappa^B z}, & \text{for } z<-\frac{L}{2} \\ f_{odd}(z)=-f_{odd}(-z) & \end{cases} \tag{2.23}$$

for odd states. In general, there are no analytical expression for the eigenvalues except for the special case of infinite V_0. In this special case both $f(z)$ and $df(z)/dz$ are zero inside B layers and corresponding energies are

$$\epsilon_n(k_x, k_y) = \frac{\hbar^2}{2m^A}\left[\left(\frac{n\pi}{L}\right)^2 + k_x^2 + k_y^2\right] \qquad n = 1, 2, 3, \dots \tag{2.24}$$

To distinguish them from the energy bands of the host crystal, these energy band are called *subbands.*

Appendix A contains a description of a *transfer matrix method* – a technique commonly used to calculate quantum well energy states.

Quasi-2D Density of States

The density of states $\rho(\epsilon)$ associated with the subbands:

$$\rho(\epsilon) = 2\sum_{k_x, k_y, n} \delta\left(\epsilon - E_n - \frac{\hbar^2 k_\perp^2}{2m^*}\right) \tag{2.25}$$

where δ is the delta function. Summation over k_x, k_y can be converted to integration over $k_\perp$-space using:

$$k_x = m\frac{2\pi}{L_x},\ k_y = m\frac{2\pi}{L_y}; \qquad \sum_{k_x, k_y} a(k_x, k_y) \rightarrow_{L_x, L_y \rightarrow \infty} \frac{L_x L_y}{(2\pi)^2}\int a(k_x, k_y)\, dk_x dk_y \tag{2.26}$$

then $\rho(\epsilon)$:

$$\rho(\epsilon) = \sum_n \rho_n(\epsilon), \quad \rho_n(\epsilon) = \frac{m_n^* S}{\pi\hbar^2} Y(\epsilon - E_n) \tag{2.27}$$

Fig. 2.3 illustrates main properties of the quantum well.

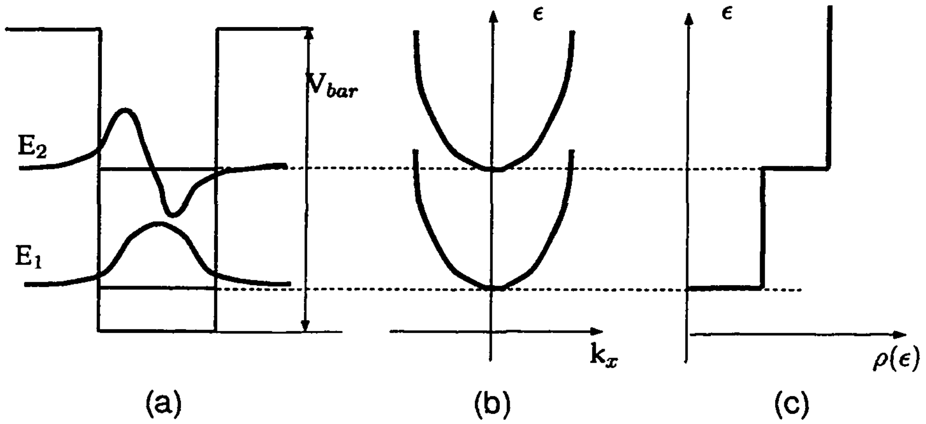

Figure 2.3: Main properties of the quantum well bound states: (a) – conduction band profile, energy levels and their envelope functions, (b) – in-plane dispersion relations of the subbands, (c) – density of states as a function of energy.

2.2.3 Optical Properties of MQW Heterostructures

In the presence of the vector potential A_{em}, describing the electro-magnetic wave, the electron momentum p should be replaced by $p + eA_{em}/c$ [24] in the Hamiltonian of the Eq. 2.4.

$$A_{em}(r,t) = -\frac{\varepsilon c F}{2i\omega}\{\exp[i(\omega t - q \cdot r)] - \exp[-i(\omega t - q \cdot r)]\} \tag{2.28}$$

where ω, q and ε are, respectively, an angular frequency, a propagation vector, and a polarization vector of the wave, F is the electric field.

To the first order in A_{em} and using the electric dipole approximation (exponential term in the Eq. 2.28 is replaced with 1) the transition probability per unit time (Fermi Golden Rule) that an electron, under the influence of A_{em}, makes a transition from the initial state $|i\rangle$ to the final state $|f\rangle$:

$$P_{i\to f} = \tilde{P}_{i\to f} f(\epsilon_i)[1 - f(\epsilon_f)] \tag{2.29}$$

where V and $\tilde{P}_{i\to f}$

$$\tilde{P}_{i\to f} = \frac{2\pi}{\hbar}|\langle f_i|V|f_f\rangle|^2\delta[\epsilon_f - \epsilon_i - \hbar\omega] \tag{2.30}$$

$$V = \frac{ieF}{2m_0\omega}\boldsymbol{\epsilon}\cdot\boldsymbol{p} \tag{2.31}$$

and $f(\epsilon_l)$ describes the mean occupancy of the level $|l\rangle$:

$$f(\epsilon_l) = \frac{1}{1+\exp\left[\frac{\epsilon_l-\mu}{k_BT}\right]} \tag{2.32}$$

where T the temperature and μ the chemical potential of the electrons.

Selection Rules

Using envelope function approximation (see Eq. 2.15) the matrix element $\langle f_i|\boldsymbol{\varepsilon}\cdot\boldsymbol{p}|f_f\rangle$ can be written as:

$$\langle f_i|\boldsymbol{\varepsilon}\cdot\boldsymbol{p}|f_f\rangle \approx \boldsymbol{\varepsilon}\cdot\langle u_i(\boldsymbol{r})|\boldsymbol{p}|u_f(\boldsymbol{r})\rangle\int_{el.cell} f_i^* f_f d^3r + \delta_{if}\boldsymbol{\varepsilon}\cdot\int_{el.cell} f_i^*\boldsymbol{p} f_f d^3r \tag{2.33}$$

where the δ_{if} is Kronecker symbol:

$$\delta_{if} = \begin{cases} 1 & \text{if } i = f \\ 0 & \text{if } i \neq f \end{cases} \tag{2.34}$$

It can be seen that the allowed optical transitions can be divided into two categories (see Fig. 2.4): *interband* transitions (the first term in Eq. 2.33), which occur between subbands originating from the different band extrema (i.e. between conduction band subbands and valence band subbands), and *intraband* transitions, which happen within the same semiconductor band and involve the dipole matrix elements between envelope functions (the second term in Eq. 2.33).

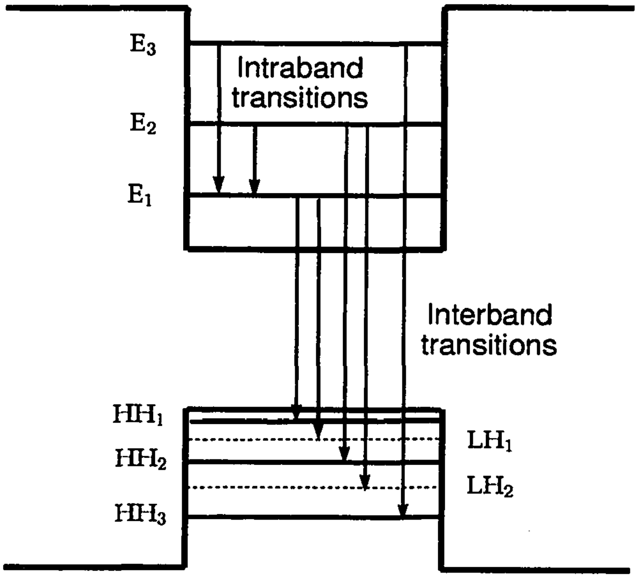

Figure 2.4: Optical transitions in the quantum well bound states. $E_{1,2,3}$ are the conduction band Γ_6 subbands, $LH_{1,2}$ and $HH_{1,2,3}$ are the valence band Γ_8 light and heavy hole subbands, respectively.

Polarization	ε_x	ε_y	ε_z
$q \parallel \hat{x}$	impossible	forbidden	allowed
$q \parallel \hat{y}$	forbidden	impossible	allowed
$q \parallel \hat{z}$	forbidden	forbidden	impossible

Table 2.2: Selection rules for intraband transitions in a semiconductor quantum well. q is the propagation vector, z is the growth axis.

Intraband Transitions

We assume z to be the growth axis (perpendicular to the wells). Using EFA the second term of the Eq. 2.33 can be re-written as:

$$\boldsymbol{\varepsilon} \cdot \int_{el.cell} f_i^* \boldsymbol{p} f_f d^3r = \hbar(\varepsilon_x k_x + \varepsilon_y k_y)\delta_{if}\delta_{k_\perp,k'_\perp} + \delta_{k_\perp,k'_\perp}\varepsilon_z \int f_i^*(z) p_z f_f(z) dz \qquad (2.35)$$

where $k_\perp = (k_x, k_y)$.

The polarizations ε_x and ε_y induce optical transitions only if the initial and final states coincide. It means that for a perfect heterostructure, the free carrier absorption is forbidden in quantum well quasi-2D electron gas, but it is allowed if the scattering by lattice imperfections is taken into account to satisfy momentum and energy conservation laws.

The polarizations ε_z corresponds to the light propagating in the layer plane (*in-plane*) with an electric field vector parallel to the growth axis. It gives the rise to the optical transitions between subbands providing that $k_\perp$ is conserved. The occurrence of intraband transition without the participation of defects *originates from the existence of a z-dependent potential in the Hamiltonian.* If the heterostructure Hamiltonian and its eigenfunctions have a definite parity, then the the matrix element $\int f_i^*(z) p_z f_f(z) dz$ is *non-zero* only if initial and the final states are of the *opposite* parities, or $n - m = oddnumber$.

Selection rules for intraband transitions are summarized in the Table. 2.2 and illustrated in Fig. 2.5a.

Polarization	ε_x	ε_y	ε_z
	$HH_n \rightarrow E_m$ transitions		
$\boldsymbol{q} \parallel \hat{x}$	impossible	$\Pi/\sqrt{2}$	forbidden
$\boldsymbol{q} \parallel \hat{y}$	$\Pi/\sqrt{2}$	impossible	forbidden
$\boldsymbol{q} \parallel \hat{z}$	$\Pi/\sqrt{2}$	$\Pi/\sqrt{2}$	impossible
	$LH_n \rightarrow E_m$ transitions		
$\boldsymbol{q} \parallel \hat{x}$	impossible	$\Pi/\sqrt{6}$	$2\Pi/\sqrt{6}$
$\boldsymbol{q} \parallel \hat{y}$	$\Pi/\sqrt{6}$	impossible	$2\Pi/\sqrt{6}$
$\boldsymbol{q} \parallel \hat{z}$	$\Pi/\sqrt{6}$	$\Pi/\sqrt{6}$	impossible

Table 2.3: Selection rules for interband transitions in a semiconductor quantum well. $\Pi = \frac{-i}{m_0}\langle S|p_x|X\rangle = \frac{-i}{m_0}\langle S|p_y|Y\rangle = \frac{-i}{m_0}\langle S|p_z|Z\rangle$, $\boldsymbol{q}$ is the propagation vector, z is the growth axis.

Interband Transitions

The selection rules for the interband transitions have two origins:

- the overlap integral between envelope functions selects the quantum numbers of the initial and final subbands. It means that for symmetrical well the initial and the final states must be of the same parities.
- $\varepsilon \cdot \langle u_i(\boldsymbol{r})|\boldsymbol{p}|u_f(\boldsymbol{r})\rangle$ of the Eq. 2.33 sets the selection rules on the polarization ε of the electro-magnetic wave.

Here it is assumed that valence band states $m_j = \pm 3/2$ and $m_j = \pm 1/2$ at $\boldsymbol{k}_\perp = 0$ are decoupled. However, any forbidden transition at $\boldsymbol{k}_\perp = 0$ might become allowed due to valence band mixing between $m_j = \pm 3/2$ and $m_j = \pm 1/2$ states at $\boldsymbol{k}_\perp \neq 0$.

Selection Rules on the Light Wave Polarization Examination of the periodic parts of the Bloch functions of the Γ_6, Γ_7 and Γ_8 bands [26] leads to the selection rules for the light wave propagation. For interband transitions the dipole matrix element $\langle u_i(\boldsymbol{r})|\boldsymbol{p}|u_f(\boldsymbol{r})\rangle$ gives:

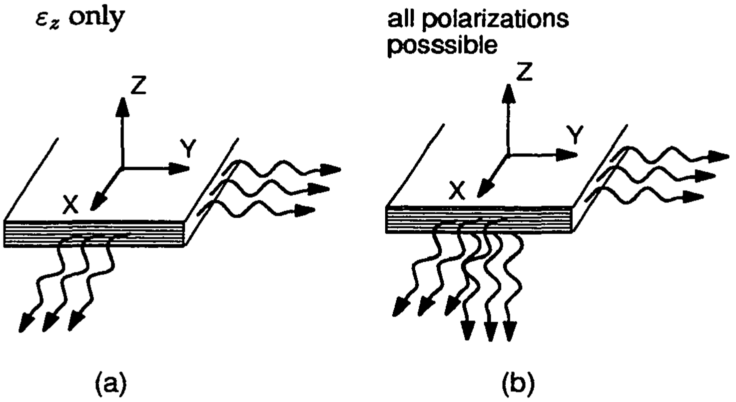

Figure 2.5: Diagram showing allowed polarization for (a) intraband and (b) interband quantum well transitions

- The heavy hole → electron transitions ($HH_n \rightarrow E_m$) are three times more intense than the light hole → electron transitions ($LH_n \rightarrow E_m$). The $\Gamma_7 \rightarrow E_m$ transitions have an intermediate strength (2/3 of $HH_n \rightarrow E_m$)
- For the propagation along z axis all three types of transitions are allowed. When the propagation happens *in-plane*, the polarization ϵ_z is forbidden for the ($HH_n \rightarrow E_m$) transitions.

Selection Rules on the Envelope Functions The envelope function overlap integral for the type I symmetrical quantum well $\langle f_n(\boldsymbol{r})|f_m(\boldsymbol{r})\rangle$ (both conduction and valence electrons are confined in the same semiconductor layer) is *non-zero* if $n + m$ is *even*. Moreover, if the well is rectangular and infinitely deep, the $n = m$ rule is imposed. In practical cases, when the wells have finite depth and not strictly rectangular, it results in that the $n = m$ transitions are much stronger than $n \neq m$ transitions.

Selection rules for interband transitions are summarized in the Table. 2.3 and illustrated in Fig. 2.5b.

Effect of Interband Coupling on the Selection Rules: Eight-Band Model Inclusion of the interband coupling into consideration has a profound effect on the optical transitions in quantum wells. It has been shown by several groups both experimentally and theoretically that in a valence band QW *in-plane* ($\varepsilon \perp \hat{z}$) polarized optical transitions are possible due to the coupling between valence bands. At the same time conduction band based structures often offer higher sensitivity and speed due to smaller electron mass than comparable valence band devices. This and the common belief in the absence of the *in-plane* polarized optical transitions in a conduction band QW has led to complicated designs to allow for coupling incident light with a MQW structure. Accurate calculations, however, showed that this strict polarization rule does not hold in the expanded band model, the model including interband coupling.

Yang *et al.* [27] have evaluated the impact of interband coupling upon the intraband transitions in a conduction band quantum well. Their analysis showed that (1) intraband transitions of both polarizations (*in-plane* and normal) are possible and (2) they are critically dependent on the coupling between the conduction and valence bands. Intraband transitions can be grouped into two categories according to whether the subband index difference $\Delta n = n' - n$ is an odd or even number.

When the Δn is *odd*, then the ratio of the matrix elements for two possible polarizations is

$$R_{odd} = \frac{M_{\|}}{M_{\perp}} \approx \frac{1}{3} \frac{(E_{n'} - E_n)\Delta}{(E_n + E_g + \Delta)(E_{n'} + E_g)} \tag{2.36}$$

where $M_{\|}$ and $M_{\perp}$ are the matrix elements for *in-plane* and normal polarizations, respectively, Δ is the split-off energy gap. This ratio is very small in most semiconductors. Thus *in-plane* polarized transitions between *adjacent* subbands in quantum wells are normally too weak to be observed, which agrees with previous results obtained without interband coupling.

Not so when the Δn is *even*. Then the ratio of matrix elements is reversed

$$R_{even} = \frac{M_{\|}}{M_{\perp}} \approx \frac{\sqrt{2}}{3}\frac{(E_n + E_g + \Delta)(E_{n'} + E_g)}{(E_{n'} - E_n)\Delta} \tag{2.37}$$

therefore, between the *second adjacent* subbands the *in-plane* polarized optical transition is dominant.

Excitons

Attraction between the electron and the hole results in the creation of coupled electron-hole pair known as *an exciton*. In most semiconductors, the Coulomb interaction is strongly screened by the valence electrons, and electrons and holes are only weakly bound in the excitons. The energy spectrum of the exciton can be obtained by finding eigenstates of the Hamiltonian:

$$\mathcal{H}_{exc}(\boldsymbol{r}_e, \boldsymbol{r}_h) = -\frac{\hbar^2 \boldsymbol{p}_e^2}{2m_e^*} - \frac{\hbar^2 \boldsymbol{p}_h^2}{2m_h^*} - \frac{e^2}{\varepsilon_0 |\boldsymbol{r}_e - \boldsymbol{r}_h|} \tag{2.38}$$

Using the following substitutions

$$\boldsymbol{R} = \frac{m_e^* \boldsymbol{r}_e + m_h^* \boldsymbol{r}_h}{m_e^* + m_h^*}, \quad \boldsymbol{r} = \boldsymbol{r}_e - \boldsymbol{r}_h \text{ and } \frac{1}{\mu} = \frac{1}{m_e} + \frac{1}{m_h} \tag{2.39}$$

the Eq. 2.38 can be decoupled and reduced to two one-particle equations: one for the motion of the exciton as a whole and another for the relative motion of electron and hole. These equations are similar to equations describing hydrogen atom. Then total energy of the exciton associated with l-th electron subband and m-th hole subband:

$$E_{exc}^{lkn} = E_{gap} + E_{E_l} + E_{HH_m} + \frac{\hbar^2 k^2}{2}(m_e^* + m_h^*) + \frac{R_{2D}^*}{n^2} \tag{2.40}$$

where R_{2D}^* is the $2D$ Rydberg constant:

$$R_{2D}^* = 4R^* = 4\frac{\mu e^4}{2\hbar^2 \epsilon_0^2} \tag{2.41}$$

where ε_0 is semiconductor static dielectric constant.

2.2.4 Strained Heterostructures

Parameters Describing Strained Heterostructures

For some heterostructures compressive or tensile strain can be intentionally introduced. Then, it is possible to force one epitaxial layer (*epilayer* A) to have the same lattice constant as the epilayer B even if these layers have different constants when they are grown separately. This results in the *strained* epilayer, a situation, characterized by a *pseudomorphic* or coherent interface, and an excess of energy equal to the elastic energy stored in the A and B epilayers. The thickness of the strained epilayer, however, limited by the strain energy, which increases with the thickness. At some particular thickness, known as a *critical layer thickness*, the epilayer can lower its total energy by relieving the strain via the creation of *misfit dislocations*. This is the *relaxed-layer* regime, characterized by a 2D density of dangling atomic bonds equal to the 2D density of atoms on each side of the interface.

Let us consider A/B superlattice (SL) in the strained-layer regime. The layers of the SL exert biaxial tensile and compressive strain on each other to conform with the same lattice constant. The elastic properties of cubic materials are described by the following matrix equation:

$$\begin{pmatrix} \sigma_{xx} \\ \sigma_{yy} \\ \sigma_{zz} \\ \sigma_{xy} \\ \sigma_{yz} \\ \sigma_{xz} \end{pmatrix} = \begin{pmatrix} C_{11} & C_{11} & C_{12} & 0 & 0 & 0 \\ C_{12} & C_{11} & C_{12} & 0 & 0 & 0 \\ C_{12} & C_{12} & C_{11} & 0 & 0 & 0 \\ 0 & 0 & 0 & C_{44} & 0 & 0 \\ 0 & 0 & 0 & 0 & C_{44} & 0 \\ 0 & 0 & 0 & 0 & 0 & C_{44} \end{pmatrix} \begin{pmatrix} \epsilon_{xx} \\ \epsilon_{yy} \\ \epsilon_{zz} \\ 2\epsilon_{xy} \\ 2\epsilon_{yz} \\ 2\epsilon_{xz} \end{pmatrix} \tag{2.42}$$

where σ_{ij} are the components of the stress tensor, $\epsilon_{ij} = \frac{1}{2}(\delta u_i/\delta x_j + \delta u_j/\delta x_i)$ are the components of the strain tensor, and the C_{ij} are the elastic constants

For the systems grown along the (001) axis the strain tensor reduces to three components: $\epsilon_{xx} = \epsilon_{yy}$ and ϵ_{zz}. Since there is no external stress along (001) surface ($\sigma_{zz} = 0$)

$$\epsilon_{xx}^{A} - \epsilon_{xx}^{B} = \frac{a_0^A - a_0^B}{a_0^B} \tag{2.43a}$$

$$\epsilon_{zz}^{A,B} = -\frac{2C_{12}^{A,B}}{C_{44}^{A,B}}\epsilon_{xx}^{A,B} \tag{2.43b}$$

Effect of the Strain on the Band Structure

Lattice mismatch on (001) oriented substrates changes energy bands by two strain components: a shift due to *hydrostatic* compression and splitting of the valence bands due to tetragonal distortion or *shear* deformation of the cubic lattice. The hydrostatic part ΔE_g^h is described by a deformation potential a_g which is known from the pressure dependence of the gap dE_g/dP, the elastic constants and the strain components ϵ_{xx} and ϵ_{zz} perpendicular and parallel to the growth direction (001):

$$\Delta E_g^h = a_g(2\epsilon_{xx} + \epsilon_{zz}) = -\frac{dE_g}{dP}\frac{C_{11} + 2C_{12}}{3}(2\epsilon_{xx} + \epsilon_{zz}) \tag{2.44}$$

The change in the bandgap from the change in the conduction band related to the strain through the deformation potential a_c of the conduction band:

$$\Delta E_c = a_c(2\epsilon_{xx} + \epsilon_{zz}) \tag{2.45}$$

Important consequence of the strain is the lowering of the symmetry of the semiconductor [28]. The tetragonal distortion removes the degeneracy of the $J = 3/2$ valence states which split by an energy 2ζ:

$$2\zeta = 2b(\epsilon_{zz} - \epsilon_{xx}) = -2b(1 + 2\frac{C_{12}}{C_{11}})\epsilon_{xx} \tag{2.46}$$

Parameter	GaAs	InAs	InP
a (Å)	5.6532	6.0583	5.8687
C_{11} (GPa)	120.9	83.29	102.2
C_{12} (GPa)	54.7	45.3	57.6
dE_g/dP (meV/GPa)	113	103	91
a_c (eV)	-7.1	-5.4	-5.9
b (eV)	-2.0	-1.8	-1.9
a_g (eV)	-8.64	-5.967	6.595

Table 2.4: Material parameters related to elastic properties of InAs, InP and GaAs.

Coupling of the light hole and split-off bands results in an extra term η, which depends on strain-induced splitting ζ and spin-orbit splitting Δ of the $j = 3/2$ and $j = 1/2$ valence bands:

$$\eta = \frac{\Delta}{2}(1 + \xi - \sqrt{1 + 2\xi + 9\xi^2}), \quad \xi = \frac{\zeta}{\Delta} \tag{2.47}$$

Eq. 2.48 summarize the effect of the strain of semiconductor bands:

$$\begin{aligned}
E_{hh}(\epsilon) &= E_{hh}(\epsilon = 0) + (\Delta E_g^h - \Delta E_c) - \zeta && \text{(2.48a)}\\
E_{lh}(\epsilon) &= E_{lh}(\epsilon = 0) + (\Delta E_g^h - \Delta E_c) + \zeta + \eta && \text{(2.48b)}\\
E_{so}(\epsilon) &= E_{so}(\epsilon = 0) + (\Delta E_g^h - \Delta E_c) + \eta && \text{(2.48c)}\\
E_c(\epsilon) &= E_c(\epsilon = 0) + \Delta E_c && \text{(2.48d)}
\end{aligned}$$

Table 2.2.4 lists elastic parameters of several semiconductors.

Strained Superlattices

The main effect of strain on an MQW structures is the change in bandgap offsets. In particular, the built-in strain can lead to re-ordering of the valence-band states. Let us consider three possible configurations (see Fig. 2.6):

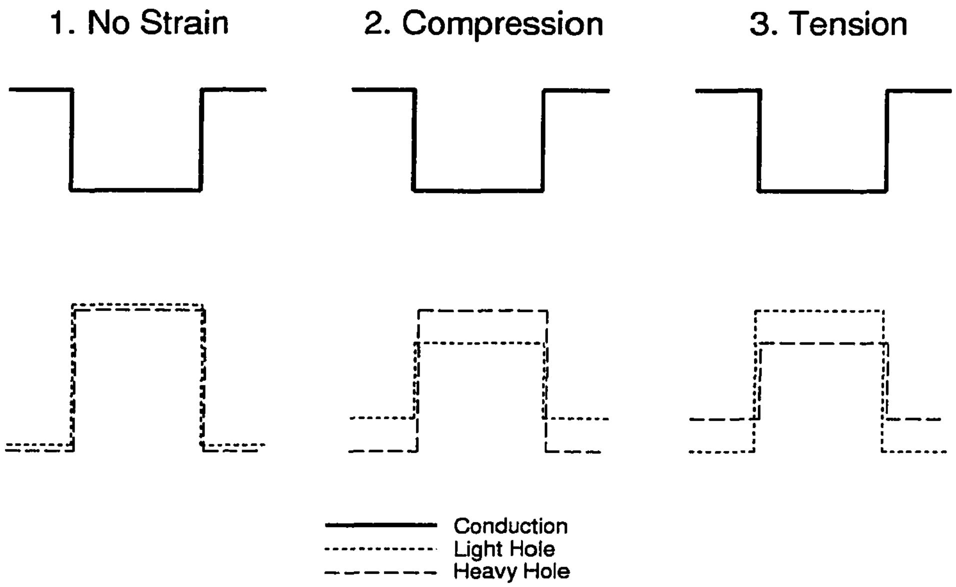

Figure 2.6: Strained quantum well configurations: (1) – no strain, (2) – biaxial compression, (3) – biaxial tension.

1. Unstrained structure (Fig. 2.6(1)). Heavy and light holes are confined in the same potential. Because of the difference in effective mass the first (lowest) energy level is always HH_1.

2. Biaxial compression (Fig. 2.6(2)). The strain-induced splitting of the bulk valence band increases the energy separation between a HH and LH bands such that "heavy" holes are confined in a deeper potential well than "light" holes. The first energy level is HH_1.

3. Biaxial tension (Fig. 2.6(3)). The strain-induced splitting is of opposite signs for HH and LH bands. Depending on the magnitude of the strain the LH_1 level can become the first energy level.

2.2.5 Quantum Wells in a Presence of Electric Field

If a constant longitudinal electric field ($\boldsymbol{F} \parallel \hat{\boldsymbol{z}}$) is applied to the quantum well, the $V(z)$ in the Hamiltonian of Eq. 2.19 is equal to eFz. There are no longer bound states and all electrons will eventually escape the well. In practice, however, over a considerable field range ($\boldsymbol{F} \leq 100\text{kV/cm}$), the quantum well structures continue to behave as if they have truly bound states, so called *metastable* states. In a small-field limit one can use a second order perturbation approach to estimate the effect of $F(z)$ on the energy state E_n:

$$E_n(F) = E_n(0) + e^2F^2 \sum_{m \neq n} \frac{|\langle m|z|n\rangle|^2}{E_n - E_m} \tag{2.49}$$

From this equation we can see that only the ground state ($n = 1$) experiences a red shift. The application of an electric field can effectively *tune* the absorption edge of a quantum well. This tunability of absorption onset is used in *electro-optical modulators*.

Applied electric field polarizes the conduction and valence band states along opposite direction (see Fig. 2.7). This has two pronounced effects on the electronic properties:

1. Weakening of excitonic bonding. Large fields can induce complete dissociation of excitons.
2. The Hamiltonian no longer has a distinctive parity and strict optical selection rules are relaxed.

2.2.6 Carrier Escape and Transport in MQW Structures

In the MQW system the vertical carrier transport (in z-direction) can be very complex. Fig. 2.8 schematically shows the processes associated with carrier transport. A characteristic lifetime constant can be ascribed to each of these processes.

$1/\tau_{th}$ thermionic emission rate. According to Schneider and von Klitzing [29] this rate for the applied field F and a quantum well of width L_w is:

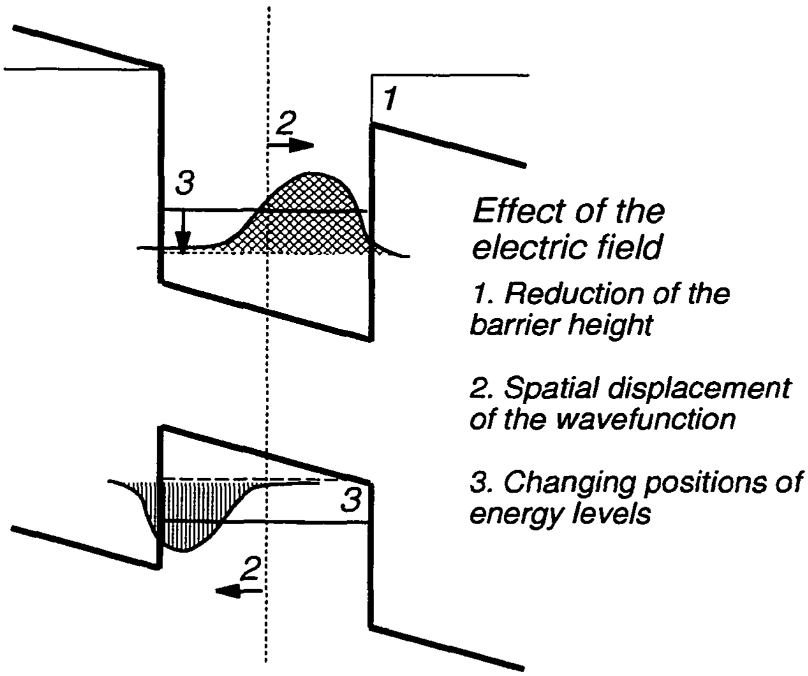

Figure 2.7: The effect of the electric field on quantum well states.

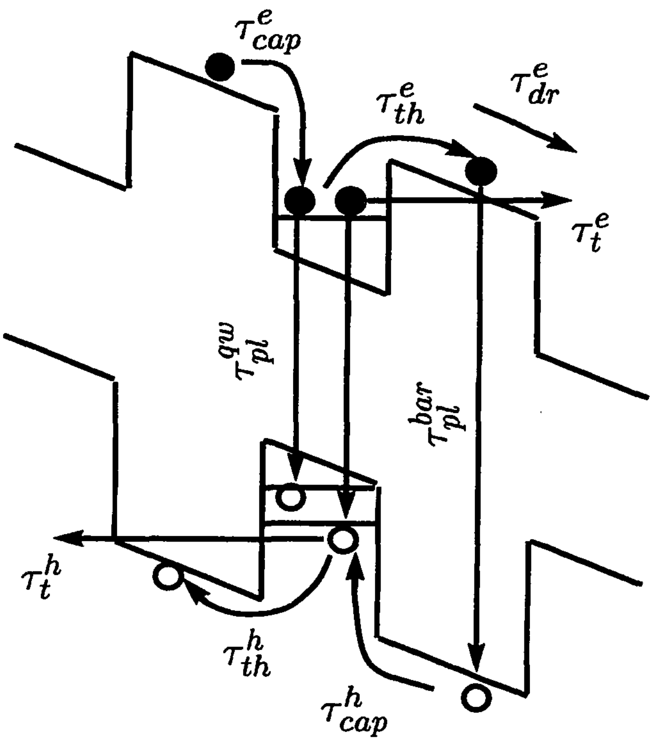

Figure 2.8: Free carrier escape and transfer processes in the MQW structure. τ's are different characteristic times associated with these processes: τ_t is the tunneling escape time, τ_{th} is the thermionic escape time, τ_{cap} is the capture time, τ_{dr} is the drift time, and τ_{pl} is radiative recombination time; indices e and h refer to electrons and holes, respectively

$$\frac{1}{\tau_{th}^{e,h}} = \left(\frac{k_b T}{2\pi m_{e,h}^*}\right)^{1/2} exp\left[-\frac{H_{e,h}(F)}{k_B T}\right] \tag{2.50}$$

where e and h indices refer to electrons and holes, respectively. The emission rate depends exponentially on the barrier height $H(F)$ and the absolute temperature T. For the simple rectangular well $H(F)$ can be written as:

$$H_{e,h}(F) = \Delta E_{c,v} - E_n^{e,h} - \frac{1}{2}|F|L_w \tag{2.51}$$

where $\Delta E_{c,v}$ is the conduction or valence band offset, and $E_n^{e,h}$ is the energy of the n-th electron (hole) subband.

τ_{tun} tunneling from a quantum well bound state into the continuum or the adjacent well. The main characteristic of this process is its exponential dependence on the carrier mass, field intensity and the shape of the barrier potential. For an arbitrary potential $V(z)$ this rate can be expressed as a product of the oscillation frequency and tunneling probability [30]:

$$\frac{1}{\tau_{tun}} = \frac{1}{L_w^2}\frac{n\pi\hbar}{2m_w^*} \exp\left[-\frac{2}{\hbar}\int_0^b \sqrt{2m_b^*(qV(z) - E_n - qFz)dz}\right] \tag{2.52}$$

The important case of the tunneling process is resonant tunneling, when the initial and final subband energies are aligned by the applied field. This alignment results in a great enhancement of the tunneling rate.

τ_{drift} drift time. Once escaped the free carriers are moving under the influence of the electric field. This field dependent constant can be estimated using expression for the saturation drift velocity

$$\tau_{drift} = \frac{\mu_{e,h}F}{L_w + L_b} \tag{2.53}$$

where $\mu_{e,h}$ is electron (hole) mobility. The mobility is a complex function of various scattering processes occurring in a semiconductor. In general, the carrier mobility in the z-direction of heterostructure is smaller than mobilities in any of constituent materials due to additional interface scattering.

τ_{cap} capture time. The free carries can be re-captured into bound states of quantum wells.

2.2.7 Recombination of Carriers in MQW Structures

Escape process directly compete with recombination processes. Whenever the *thermal equilibrium* is disturbed by the generation of electron-hole pairs, recombination processes exist to restore the system equilibrium. The thermal equilibrium is characterized by a situation when the rate of thermally stimulated transitions between any two energy states is equal to the rate of the recombination process. Recombination processes can be divided into two classes: band-to-band recombination and recombination through the participation of various crystal defects. Generally, all recombination processes occur simultaneously and the total recombination rate is the sum of all individual processes.

$$\frac{1}{\tau_{rec}} = \Sigma_i \frac{1}{\tau_i} \tag{2.54}$$

The shortest rate thus dominates the total recombination in the crystal. The lifetime for a particular recombination process can be calculated by considering the generation and recombination rates between two levels.

Band-to-Band Recombination

The direct recombination of an electron-hole pair when the electron goes from the conduction to the valence band is a process that can not be suppressed in a crystal, and thus the corresponding lifetime gives an upper limit for the total carrier lifetime in the semiconductor. Several processes can be distinguished depending on how the excess energy is dissipated. The energy can be released by the emission of a photon (*radiative recombination*) or by the excitation of a second free electron or hole (*Auger recombination*). In the Auger recombination, the excited particle finally transfers its energy to the lattice through the interaction with phonons. The general expression for the transition rate of the band-to-band recombination τ_{b2b} is given by:

$$\frac{1}{\tau_{b2b}} = \int P(E,E')N_V(E)f(E)N_C(E')(1-f(E'))dEdE' \tag{2.55}$$

where $P(E,E')$ is the probability per unit time for the transition between the energy levels E and E', and $f(E)$ is the occupation probability.

In general, one assumes that the transition probability for radiative recombination (P_{rr}) is a constant, while for the Auger process (P_{ar}) is proportional to the carrier concentration (it is a second order process). For low doping concentration, the probability of the Auger recombination is usually small compared to the radiative recombination, but it increases rapidly with the majority carrier concentration. In fact it becomes the dominant recombination mechanism in heavily doped indirect semiconductors like silicon. The radiative recombination lifetimes are much larger in indirect than in direct semiconductors. The band-to-band recombination, however is not the only possible recombination process, and in semiconductor with a relatively large bandgap the lifetime is usually dominated by recombination on impurities and other lattice defects.

Recombination on Lattice Defects

Deep Level Impurities Lattice defects introduce energy (trap) levels in the forbidden energy gap. This reduces the lifetime of the minority (photoexcited) carriers and thus has a severe effect on the performance of photovoltaic devices.

Point defects are characterized by a single energy level E_T. In this case, $N_C(E)$ in Eq. 2.55 can be described by a delta function $N(E) = N_T\delta(E - E_T)$ where N_T is the total concentration of traps. The occupation of the trap is determined by the following four processes: the capture of electrons in the trap level and thermal generation into the conduction band, and the capture of the holes and thermal generation into the valence band. The total recombination rate on the trap level is given by Shockley-Read-Hall (SRH) statistics:

$$R = \frac{np - n_i^2}{\tau_p(n + n_{tr}) + \tau_n(p + p_{tr})} \tag{2.56}$$

where $\tau_{n,p}$ are the electron and hole recombination lifetimes, and n_{tr} and p_{tr} are:

$$n_{tr} = N_C \exp(-\frac{E_c - E_{tr}}{k_B T}) \qquad p_{tr} = N_V \exp(\frac{E_v - E_{tr}}{k_B T}) \tag{2.57}$$

where E_{tr} is the trap energy level. The analysis of the SRH expression shows that the lifetime is mostly affected by deep trap centers in the middle of the bandgap. The lifetime decreases with increasing doping concentration first and remains constant for the higher doping level.

Surface and Interface Recombination Similar to impurity atoms, surfaces and interfaces introduce electronic states in the energy bandgap. Because a surface is not a point defect, it creates a continuous density of states as shown in Fig. 2.9. The trapped charge on the surface states creates so-called *band bending*. For a clean surface, the position and distribution of the surface states is directly related to the underlying atomic structure. However, due to the exposure to oxygen and other chemically active elements in the air, the surface is usually covered with an oxide layer or with adsorbed foreign atoms. The surface properties therefore can be significantly modified by surface preparation techniques like polishing and etching. The surface recombination rates [31] for p- and n-type semiconductor are:

$$S_p = \sigma \nu_T N_{so} \exp(\frac{V_s}{k_b T}) \qquad S_n = \sigma_n \nu_T N_{su} \exp(\frac{-V_s}{k_b T}) \tag{2.58}$$

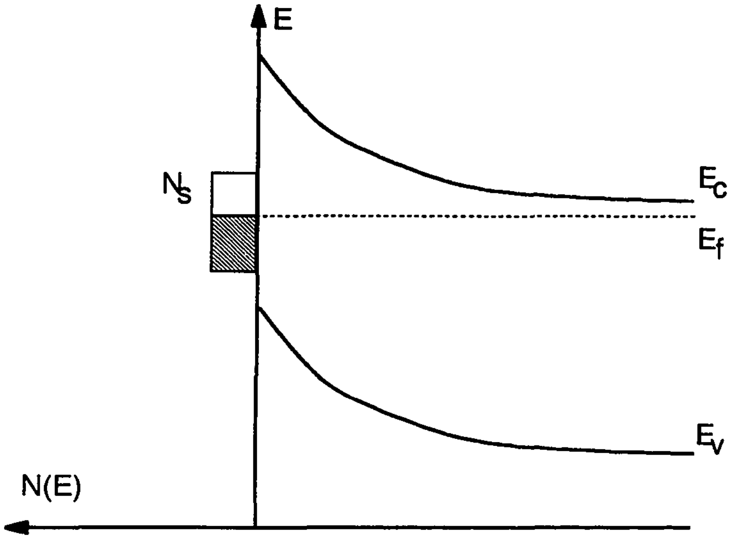

Figure 2.9: Semiconductor surface states. N_S is the density of the surface states, E_f is the Fermi energy.

where $\sigma_{n,p}$ are the electron and hole capture cross sections, $\nu_T = (8k_bT/\pi m_0)^{1/2}$ is the thermal velocity of electrons, and V_s is the surface potential associated with surface charge Q_s: $V_s = Q_s^2/8\varepsilon\varepsilon_0 N_d$. As in case with the impurity atoms, the most effective surfaces are those with a quasi-Fermi level E_{so} near the middle of the bandgap.

2.2.8 Resonant Tunneling Transport in MQW Structures

Tunneling of the particle through a barrier is one of the most studied phenomena in quantum mechanics [32]. We can distinguish two important cases of tunneling in QW heterostructures: nonresonant and resonant tunneling . The following is a brief description of each case.

Nonresonant Tunneling When there is no coupling between wells and energy states are well separated, the wavefunctions are localized and the transfer to another well can only occur through scattering process which can be either an elastic or inelastic collision.

Phonon-electron interaction can play an important role here. When the difference between the final and initial state are comparable to an optical phonon energy $\hbar\omega_{LO}$ ($\Delta E_{i\rightarrow f} = E_f - E_i \approx \hbar\omega_{LO}$), and if the phonon-assisted tunneling rate is larger than other escape processes, then an increase in tunneling rate can be observed when the $\Delta E_{i\rightarrow f}$ exceeds $\hbar\omega_{LO}$, i.e. phonon absorption becomes allowed. Müller *et al.* [33] have observed resonances due to elastic (resonant) tunneling out of the ground state as well as the respective satellite peaks due to LO phonon-assisted tunneling.

Resonant Tunneling When there is a strong coupling between wells and energy states are aligned in resonance, these states are split into two (crossing and anti-crossing states). Unlike nonresonant case, the transfer between the wells does not require the change in the energy or momentum. The wavefunctions of these two states are *delocalized* and have an equal amplitude in each well (with no electric field present). If initially electrons were localized in one well, the electron density will oscillate between two wells with the period $\tau_{coh} = h/\Delta E$, where the ΔE is the difference between crossing and anticrossing states. However, inhomogeneities in the well widths and electric field, as well as various scattering processes, cause the observed tunneling time to be sometimes the order of magnitude larger than the calculated *coherent time* [21,23].

Tunneling in DBQW

Tunneling plays an important role in many semiconductor devices. An important characteristic of the tunneling diode is the *negative differential resistance* (NDR), which makes it possible to use these devices in high frequency generators. The NDR has been observed in single QW and MQW devices. Let us consider the simplest case of the QW tunneling diode - *double barrier quantum well heterostructure diode* (DBQW).

Typical DBQW consists of a quantum well sandwiched between two barriers. Fig. 2.10 shows the current-voltage characteristic of the AlGaAs/GaAs diode with the correspond-

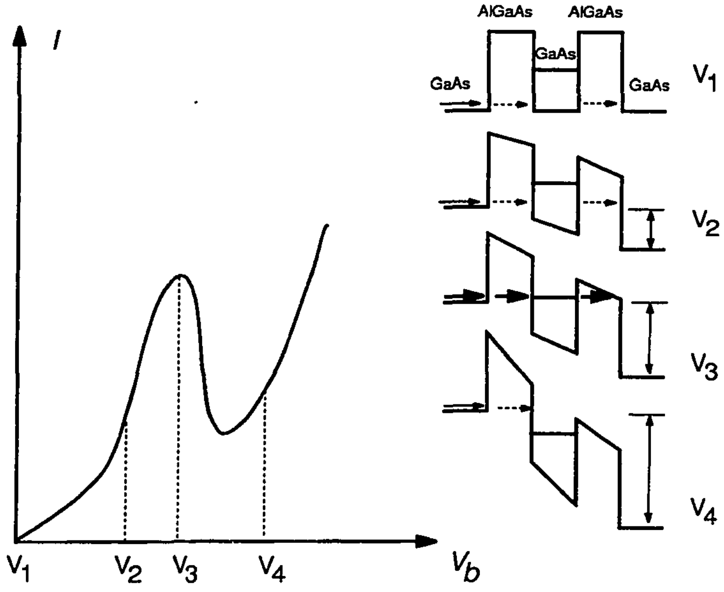

Figure 2.10: Current- voltage characteristic of a double-barrier resonant tunneling AlGaAs/GaAs diode. The right side of the figure shows schematic band diagram at different points of the I-V curve.

ing band diagrams at selected points of the I-V curve. The carriers are injected from the left side of the diode, the emitter. Under the applied bias, electrons can tunnel from the GaAs emitter on the left through the barriers and QW to the right side, the collector. The resonance occurs when the quasi Fermi energy of the electron in the emitter coincides with the energy of quantum well subband.

The current is small initially ($V_{bias} : V_1 \rightarrow V_2$) and increases with the applied voltage. As soon as the voltage reaches the resonant value of bias ($V_{bias} \approx V_3$) the current will show a peak in the I-V curve. Once bias passes V_3, the current shows a *decrease* up to some bias. This is the NDR region. The ratio of the current at resonant tunneling voltage to that of the minimum before the current starts to increase is called *peak-to-valley current ratio.* The magnitude of the ratio strongly depends on the scattering of the tunneling electrons by the various defects and phonons. The phonon scattering has a very pronounced temperature dependence and results in degradation of the peak-to-valley ratio at high temperatures.

The tunneling current density can be calculated if the tunneling probability $T(E)$ is known:

$$J_{tun} = \frac{e}{4\pi^3\hbar}\int_0^\infty dk_x dk_y \int_0^\infty dk_z \left(\frac{\partial E}{\partial k_z}\right) T(E_z)(f(E') - f(E)) \tag{2.59}$$

where the $f(E)$ and $f(E')$ are the occupation probabilities of the initial and final states, respectively. In an assumption of no scattering this formula can be written as [34]:

$$J_{tun} = \frac{qm^* k_B T}{2\pi^2\hbar^3}\int_{E_c}^\infty T(E_z, F)\ln\left(\frac{1+\exp((E_z - E_f)/k_B T)}{1+\exp((E_z - E_f - eV)/k_B T)}\right) dE_z \tag{2.60}$$

The most commonly used method to calculate the transmission probability $T(E_z, F)$ through an MQW structure is based on the *transfer matrix method.* The outline of this method is given in the Appendix A.

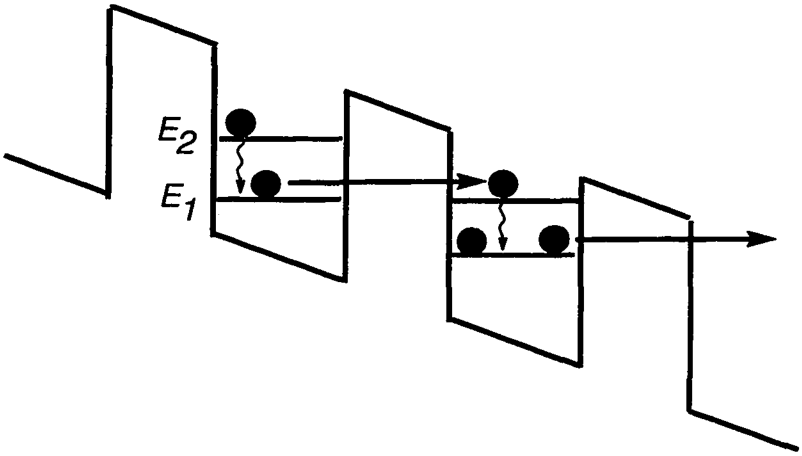

Figure 2.11: Sequential resonant tunneling in multiple quantum well structure

Tunneling in MQW Structures

Tunneling phenomenon in MQW structures has basically the same characteristics as that in the DBQW structures: resonant peaks in the I-V curve and degradation with temperature. Historically, tunneling in the MQW was first predicted theoretically and then observed experimentally.

Sequential resonant tunneling The term *sequential* is used here to denote the peculiarity of the resonant tunneling in the multiple quantum well structures. In most situations there is no coherent state which extends over the whole MQW region. Which means that tunneling occurs in many steps or *sequentially* as it is shown in Fig. 2.11. Each tunneling process is followed by a non-radiative or radiative relaxation from the E_2 state to the E_1 state. Then the process repeats itself. It is said that the superlattice is of the tight-binding type: the coupling between the wells is weak and their minibands can be satisfactorily described in terms of discrete energy states of a single quantum well.

In 1971 Kazarinov and Suris [35] theoretically studied the current-voltage characteristic of the MQW structures and predicted the existence of peaks corresponding to resonant

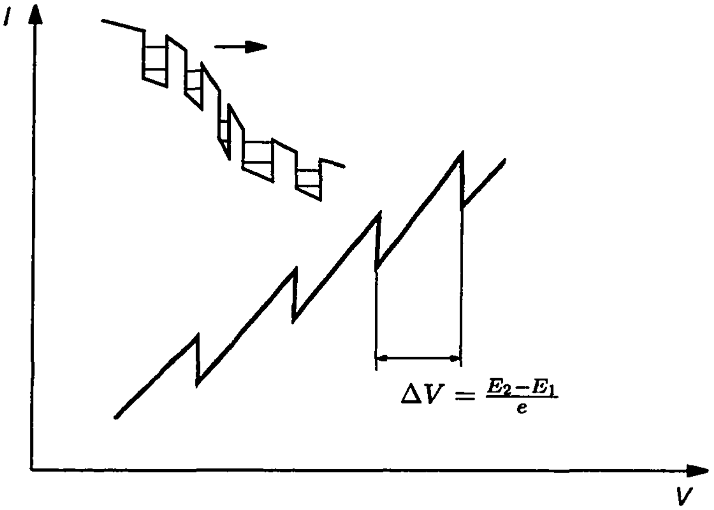

Figure 2.12: Voltage oscillations in the current-voltage characteristic of an MQW resonant tunneling structure. The period of the oscillations, ΔV, is equal to the quantum well subband separation, $\frac{E_2 - E_1}{e}$.

tunneling between the ground and excited states of adjacent wells. In 1974, Esaki and Chang [36] observed discontinuities (shown in Fig. 2.12) in the *I-V* characteristics with an average separation equal to the subband spacing in each quantum well: $\Delta V = (E_2 - E_1)/e$. This was explained through the formation of high and low electric field domains in the MQW region: the resonant condition *did not* extend to the whole region (see the inset in Fig. 2.12) but existed only in some areas (domains). Sweeping the bias results that some areas get in the resonance while the others get off. The resulting I-V curve has a saw-like look as shown in Fig. 2.12.

In 1989, Capasso, Mohammed and Cho (CMC) [15] reported on sequential resonant tunneling which existed in the whole MQW region. To prevent formation of the field domains and ensure uniform field, the superlattice was placed inside the i region of a reverse-biased $p^+ - i - n^+$ junction. As a result of these precautions instead of an oscillatory conductance with a voltage period equal to Δ as in Fig. 2.12, the I-V characteristic showed just two peaks at voltages $n\Delta/e$ and $n\Delta_1/e$, where n is the number of superlattice periods.

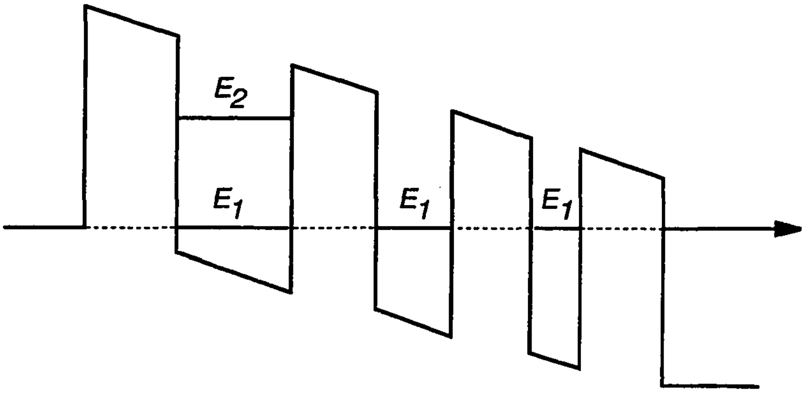

Figure 2.13: Non-Sequential resonant tunneling in multiple quantum well structure

These peaks corresponded to resonant transitions $E_1^n \to E_2^{n+1}$ and $E_1^n \to E_3^{n+1}$.

Non-Sequential resonant tunneling Non-sequential resonant tunneling refers to the situation when the coherent state does extend over the whole MQW region. Summers and Brennan were first to propose and actually made a device with resonant tunneling which occurred simultaneously across three quantum wells [18,37]. These is achieved by making devices where the quantum well widths are progressively decreased through the superlattice such that under the appropriate bias, the confined quantum levels in adjacent wells become aligned [18] as shown in Fig. 2.13. Unlike in sequential tunneling devices, in non-sequential ones the number of QW which can be put together in resonance is limited to 5-6.

Resonant Tunneling Times in Quantum Well: Time-Resolved Experiments Steady-state measurements can provide only very indirect information on the dynamics of the transport. Time-resolved techniques are required for the direct study of the transport process. Progress in the ultrafast spectroscopy for the last decade has offered "the possibility of studying and discovering key processes unresolved in the pass" [19]. Ultrafast laser spectroscopy was particularly successful in investigating tunneling phenomena in MQW heterostructures by measuring photoluminescence decay times.

Oberli *et al.* have reported [21] on the direct measurement of resonant and nonresonant tunneling times in double asymmetric coupled quantum wells using subpicosecond PL spectroscopy. They have investigated several asymmetric double quantum well samples with different barrier thicknesses. The samples were placed under different bias and tunneling from narrow to wide well was studied. PL decay time from the narrow well was directly associated with tunneling time from that well. This study revealed a *nonmonotonic* behavior of the tunneling time (tunneling time vs. bias has showed a minimum at certain voltage) with the increasing electric field, which was a direct evidence of resonant transfer occurred between narrow and wide wells. The authors found that the resonance field value was off the calculated value by several per cent, which they explained by space-charge build-up: in the PL experiment the photoinduced carrier density is sufficiently high to change the internal field, consequently, an additional bias needs to be applied to compensate for this extra field. The measured tunneling time for 55 Å AlGaAs barrier was 7.6ps which was considerably larger than the calculated value of 0.67ps. The authors explained this increase by dumping of coherent oscillations between wells through various scattering mechanisms.

Resonant tunneling can greatly reduce the time it takes carriers to reach device terminals. Livescu *et al.* [22] have conducted measurements of tunneling escape time in 75 well GaAs/AlGaAs MQW structure using pump-and-probe electroabsorption technique. The experiment has a pulse-width limited resolution of $\approx$ 10ps. Fig. 2.14 shows measured differential absorption rise time τ as a function of applied field; the rise time τ is a direct measure of carrier escape time. The authors found that τ is independent of temperature, which means that tunneling is most likely the dominant escape mechanism in this sample. It is clearly seen that the curve has a pronounced minimum at 130 kV/cm which corresponds to the resonance between the $n = 1$ electron level in the one quantum well, and the $n = 2$ electron level in the adjacent one. The resonant tunneling has reduced the rise time

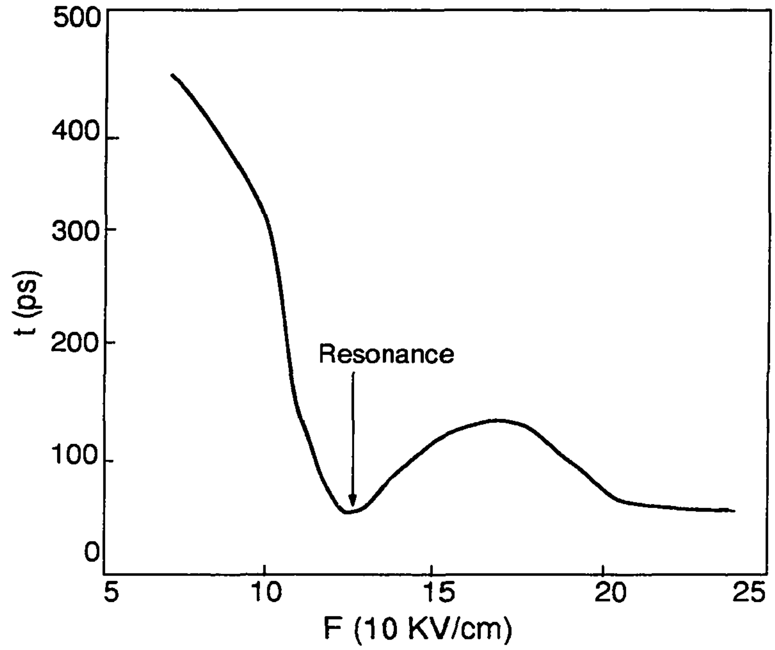

Figure 2.14: Differential absorption rise time vs. applied field in MQW GaAs/AlGaAs (from [22]).

almost tenfold.

2.3 Principles of Photovoltaic Conversion

The following section describes physical aspects of the photovoltaic conversion. Efficient photovoltaic conversion is based on the three major factors:

- Strong optical absorption over the whole solar spectrum.
- A physical mechanism of separating photogenerated carriers.
- Lossless transport of photogenerated carriers towards devices terminals.

2.3.1 Absorption and Emission of Light in Semiconductors

Absorption of light

The photogenerated current I_{ph} is determined by the absorption behavior of the semiconductor in question. The fraction of incident light $A = 1 - R$ that penetrates inside the absorbing material can be calculated from the complex refraction index $n_c = n - i\kappa$, where κ is the extinction coefficient and the reflectivity R is given by:

$$R = \frac{(n-1)^2 + \kappa^2}{(n+1)^2 + \kappa^2} \tag{2.61}$$

where both $n(\nu)$ and $\kappa(\nu)$ are functions of the photon frequency ν. The light passing through the material generates electron-hole pairs whose number depends on the number of incident photons per unit area, unit time, and unit energy $S_0(\nu)$. Inside the material the photon flux $S(x,\nu)$ decreases exponentially:

$$S(x,\nu) = S_0(\nu)\exp^{-\alpha x}, \quad where \quad \alpha(\nu) = \frac{4\pi\kappa\nu}{c} \tag{2.62}$$

Then the number of electron-hole pairs $G(x,\nu)$ generated per unit time in the volume between x and $x + \Delta x$ is:

$$G(x,\nu) = \beta(\nu)\alpha(\nu)S_0(\nu)(1-R)\exp^{-\alpha(\nu)x} \tag{2.63}$$

The quantum efficiency $\beta(\nu)$ takes into account that only a fraction of absorbed photons generate electron-hole pairs. For Ge, Si and some III-V compound *direct* semiconductors values of $\beta(\nu) \approx 1$ are measured even near the absorption edge.

For photons with energy higher than the bandgap energy $h\nu > E_g$, the generated electrons carry an excess kinetic energy which is rapidly dissipated to the lattice through the electron-phonon interactions. If the kinetic energy is high enough, more electrons can be created through impact ionization so that values $\beta(\nu) \gg 1$ can be observed.

The absorption coefficient $\alpha(\nu)$ depends on the band structure of the semiconductor. For direct (no change in wave vector $\boldsymbol{k}$) transitions this coefficient (α_d) is:

$$\alpha_d(\nu) = \alpha_0 \frac{(h\nu - E_G)^{1/2}}{h\nu} \tag{2.64}$$

where α_0 is a constant obtained either from calculations, or from fitting to experimental data.

In indirect semiconductors like Si and Ge, optical transitions between states close to the band edges require a change in the momentum of the electrons $\boldsymbol{p} = \hbar\boldsymbol{k}$ and therefore only possible with phonon participation. The absorption coefficient $\alpha_{in}^{ij}(\nu)$ associated with allowed indirect transitions:

$$\alpha_{in}^{ij}(\nu) = \frac{(h\nu - E_{gi} + h\nu_{ph,j})^2}{\exp(h\nu_{ph,j}/k_B T) - 1} + \frac{(h\nu - E_{gi} - h\nu_{ph,j})^2}{1 - \exp(-h\nu_{ph,j}/k_B T)} \tag{2.65}$$

The $\alpha_{in}^{ij}(\nu)$ is the sum of the absorption processes involving emission and absorption of phonons.

Emission of light

Closely related to the absorption process is an *emission* or *radiation* process. In order to emit radiation electron-hole pairs first must be created. Depending on the type of the excitation source there are several kinds of luminescence: *photoluminescence,* where the electron-hole pairs are created by the light source, *electroluminescence,* where carriers are injected by driving electrical current through the sample, *thermoluminescence,* where the pairs are created by heating the sample, and *sonoluminescence,* where the emission is due to the propagation of the acoustic waves through the sample.

Emission is the inverse of absorption, and the relation between these two processes is known as *the van Roosbruck-Schokley relation.* The emission rate for the transition from the conduction band to the valence band R_{cv} is given by:

$$R_{cv}(\nu) = \frac{\alpha(\nu) 8\pi (\nu n_{rf})^2}{c^2 e^{\frac{h\nu}{k_B T}} - 1} \tag{2.66}$$

where $\alpha(\nu)$ is the semiconductor absorption coefficient, n_{rf} is the refraction index and ν the light frequency. In heavily doped semiconductors the emission spectra are modified by additional effects such as bandgap shrinkage, radiative recombination centers, band filling and others.

The luminescence is produced by fully or partially thermalized carriers and thus, the emitted photons have no correlation with the excitation process. However, in time-resolved experiments one can observe so-called *hot luminescence*, the emission from the incompletely thermalized carriers.

Optical transitions can be classified into several major categories

band-to-band transitions This type of transitions involves the recombination of free electrons and free holes. In high quality direct bandgap semiconductors such as GaAs and InP, *band-to-band* (B2B) transitions are a dominant recombination mechanism. In indirect bandgap semiconductors such as Si and Ge, electron-hole recombination requires participation of phonons. B2B transitions can characterized by a *radiative recombination time*, τ_{rad}. In general, recombination time is a function of the emitted wavelength. Typically, for pure semiconductors, τ_{rad} ranges from a few μs for direct semiconductors to seconds and hours for indirect semiconductors. In a doped semiconductor the carrier radiative lifetime is reduced and strongly depends on the doping concentration.

free-to-bound transitions B2B transitions are dominant at high temperature when all the shallow impurities are ionized. At lower temperatures, carriers become trapped at impurity atoms. A new type of transition, involving a free carrier and a charge bound to an impurity, become possible – *free-to-bound* transition. If the semiconductor is

p-type then the emitted photon energy is equal to $E_g - E_A$, where the E_A is the shallow acceptor binding energy. The PL intensity of this transition is proportional to $(1 - \exp[-E_A/(k_B T)])$. Then the acceptor ionization energy E_A can be deduced from the slope of so-called *Arrhenius plot* of $\log[1 - (I(T)/I(T_0))]$ vs. $1/(k_B T)$, where $T_0 = 0$ and $I(T)$ is the PL intensity.

donor-acceptor transitions In many situations a semiconductor can contain both donors and acceptors. Such semiconductors are called *compensated,* because some of the electrons from the donors will be captured on ionized acceptors (A^-) as well as some holes from the acceptors can be captured on ionized donors (D^+), thus *compensating* the effect of doping. Optical excitation creates electrons and holes which can be trapped on ionized impurities and neutralize them. Some of the trapped carriers can later recombine via radiative recombination via reaction [32]:

$$D^0 + A^0 \rightarrow \hbar\omega + D^+ + A^- \tag{2.67}$$

with the photon energy:

$$\hbar\omega = E_g - E_A - E_D + \frac{e^2}{\varepsilon R} \tag{2.68}$$

where the term $e^2/(\varepsilon R)$ takes into account lowering of the energy due to Coulomb attraction, R is the distance between the D^+ and A^-, and E_A andE_D are the acceptor and donor activation energies, respectively.

free-exciton and bound-exciton emission At low temperatures in high quality semiconductors electrons and holes can be attracted to each other by Coulomb interaction and form *free excitons.* The radiative recombination of the exciton pair is the dominant feature of the semiconductor emission spectra at low temperatures. When the semiconductor contains a number of neutralized impurities the excitons can be attracted to these impurities by *van der Waals* interaction and form so-called *bound ex-*

citons. Because of the binding, the bound-exciton peak appears below the energy of the free-exciton peak.

2.3.2 Carrier Transport

To describe the motion a charged particle in periodic lattice, we will use a *quasi-classical* approach, where all effects of local atomic field are contained in the effective mass. Then, an equation of motion can written as:

$$m^* \frac{d^2 \boldsymbol{r}}{dt^2} + \frac{m^*}{\tau} \frac{d\boldsymbol{r}}{dt} = -e\boldsymbol{F} \tag{2.69}$$

where $\boldsymbol{r}$ is the position of the particle, τ is a phenomenological scattering time introduced to account for lattice imperfections, and $\boldsymbol{F}$ is an external electric field applied to the particle.

Under the influence of $\boldsymbol{F}$ a charged carrier will accelerate, until the retardation term $\frac{m^*}{\tau}\frac{d\boldsymbol{r}}{dt}$ in Eq. 2.69 cancels out the field term $e\boldsymbol{F}$. The particle velocity at this steady state situation is referred as a *drift* velocity:

$$\boldsymbol{v}_{dr} = q\boldsymbol{F}\tau/m^* = \mu\boldsymbol{F} \tag{2.70}$$

where μ is the carrier *mobility*:

$$\mu = q\tau/m^* \tag{2.71}$$

The current density J at steady state is related to v_{dr} and τ_k by

$$J = nqv_{dr} = nq^2\boldsymbol{F}\tau/m^* \tag{2.72}$$

Relaxation Time Approximation

We will generalize the current density expression for the system of particles distributed in a band according Boltzmann or Fermi-Dirac statistics. This implies the solution of *Boltzmann equation*:

$$\frac{df_k}{dt} = \left(\frac{\partial f_k}{\partial t}\right)_f + \left(\frac{\partial f_k}{\partial t}\right)_{dif} + \left(\frac{\partial f_k}{\partial t}\right)_{sc} \tag{2.73}$$

this equation includes the effect of field (I term), the carrier diffusion (II term), the scattering of carriers by phonons, impurities etc. (III term), and k refers to the wave vector of the electron. Neglecting the diffusion term and in assumption that the field is small enough to permit the expansion of the f_k in terms of $\boldsymbol{F}$: $f_k = f_k^0 + \nabla_k f_k \cdot \boldsymbol{F} = f_k^0 + g_k(\boldsymbol{F})$ and the field term:

$$\left(\frac{\partial f_k}{\partial t}\right)_{field} \approx \left(\frac{\partial f_k^0}{\partial E_k}\right)\frac{dE_k}{dt} = \left(\frac{\partial f_k^0}{\partial E_k}\right) q\boldsymbol{v}_k \cdot \boldsymbol{F} \tag{2.74}$$

Within the *relaxation time approximation* and at steady state ($df_k/dt = 0$) it is assumed that the net result of all scattering events is to cause g_k to relax with a time constant τ_k. Then

$$g_k = \left(\frac{\partial f_k^0}{\partial E_k}\right) \tau_k q \boldsymbol{v}_k \cdot \boldsymbol{F} \tag{2.75}$$

and the current density:

$$J = \int q g_k \boldsymbol{v}_k d\boldsymbol{k} = q^2 \int \left(\frac{\partial f_k^0}{\partial E_k}\right) \boldsymbol{v}_k \tau_k q(\boldsymbol{v}_k \cdot \boldsymbol{F}) d\boldsymbol{k} \tag{2.76}$$

All effects of the scattering are contained in τ_k.

Next we consider different scattering mechanisms existing in a semiconductor. Carriers in a semiconductor can be scattered via interaction with the following:

- acoustic and optical phonons

- ionized and neutral impurity atoms
- surface and interfaces
- other carriers interaction

We will give a short characteristic of each scattering process.

Scattering by Acoustic Phonons In electron-phonon interaction, the conservation of momentum and energy is presumed in every scattering event:

$$E'_k - E_k = E_{ph} \qquad \boldsymbol{k}' - \boldsymbol{k} = \boldsymbol{q} \tag{2.77}$$

where prime denotes final state (after scattering). Acoustic phonon energy for a small $\boldsymbol{q}$ is:

$$E_{ph} = \hbar v_{ph} q \tag{2.78}$$

The maximum energy lost by an electron can be estimated from Eq. 2.77 and Eq. 2.78 as:

$$E_k - E'_k = \hbar v_{ph} q_{max} = 2\hbar v_{ph} k - 2m v_{ph}^2 \tag{2.79}$$

This estimate shows that in emitting an acoustic phonon with wave vector q_{max} the electron reverses its direction while loosing only 13% of its original energy. Thus the scattering between electrons and acoustic phonon is quasi-elastic and the main effect is the relaxation of electron momentum.

Scattering by Polar Optical Phonons Typical energy of the optical phonon in a semiconductor is 30 meV. So at low temperature most electrons do not have enough energy to emit optical phonons. In addition, the occupation number of optical phonons is also low and the scattering events involving phonon absorption are very rare. Thus, optical phonon-electron interaction at low temperature can be safely ignored. At room temperature, these interaction tend to dominate over acoustic phonon scattering. While scattering by acoustic phonons relaxes mainly the electron momentum, scattering by optical phonons changes both momentum and energy of electron.

Intervalley scattering The role of intervalley scattering is very different in indirect and direct semiconductors. In direct semiconductors (InP and GaAs) this process is only important for the electrons with high enough energy to scatter into the higher conduction bands, so-called *hot electrons*. In indirect semiconductors (Si and Ge) the electrons are located in conduction band minima which are not at the zone center and are degenerate. It turned out that in Si and Ge the intervalley processes are more important than the intraband processes in relaxing the momentum and energy of the electrons.

Scattering by Impurity Atoms These processes are caused by a Coulomb interaction of electrons with the ionized atoms. Because of the huge difference between masses of participating particles the scattering process are elastic.

Scattering by Interaction with Other Carriers: Electron-Electron Scattering Of all scattering processes considered above this type of scattering has usually a lesser role. The main effect of the EES are a reduction of mobility in semiconductors [38] and thermalization process.

Scattering in MQW structures It is common practice to consider *intraband* scattering (scattering between two subbands in quantum well) as a special case. It is not caused, however, by any new physical mechanism besides that considered above. If the density of the carriers inside the quantum well is relatively low, electron-electron scattering events are rare, and the dominant scattering mechanism is electron-phonon interaction. For narrow wells, a proximity to the heterostructure interface can result in additional phonon modes involved in this process, so called "interface" modes or 2D phonons. Dür, Goodnick and

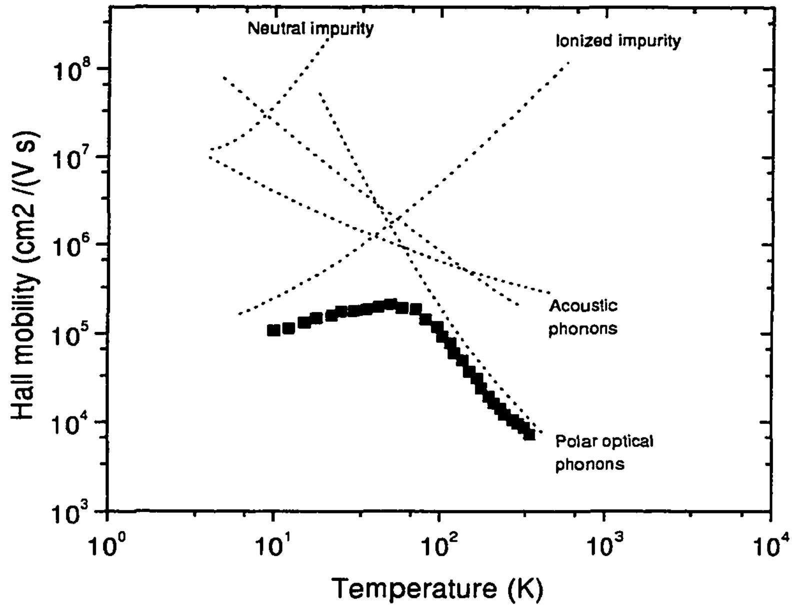

Figure 2.15: Experimental dependence of mobility (squares) in n-type GaAs determined by Hall measurements. The dotted curves are the corresponding contributions from the various scattering mechanisms [32].

Lugli [39] conducted an extensive Monte Carlo simulation of intersubband relaxation in GaAs/Al_xGa_{1-x}As quantum wells. Their conclusion was that the decay of electron from the first excited subband into the ground subband is limited by ionized impurity scattering. Polar optical phonon emission also gives a considerable contribution to the electron decay when it is allowed. Intersubband scattering by electron-electron interaction plays a lesser role for the electron decay.

In the general case the scattering time τ depends on carrier energy and temperature. For a non-degenerate electron gas (Boltzmann statistics) in a parabolic band the average scattering time τ_{ave} can be written as:

$$\tau_{ave} = \frac{2}{3k_BT} \cdot \frac{\int \tau(E) E^{3/2} e^{-E/k_BT} dE}{\int E^{1/2} e^{-E/k_BT} dE} \tag{2.80}$$

where $\tau(E)$ is a sum of contributions from various scattering processes:

$$\frac{1}{\tau(E)} = \sum_k \frac{1}{\tau_k(E)} \tag{2.81}$$

Fig. 2.15 illustrates the effect of different scattering processes on the mobility of GaAs [32].

2.3.3 Operation of a Solar Cell

This section deals with a semiconductor solar cell based on the *p-n* junction photodiode. The basic equations describing the photodiode operation are given.

The most widely used photovoltaic device is based on the semiconductor diode. Solar cells require a shallow *p-n* junction (a junction, positioned close to the surface), a front ohmic contact usually covering less than 5 % of the surface and the back contact which covers the whole back surface. Layer diagram of the *p-n* junction based solar cell is shown in Fig. 2.16.

For an abrupt junction with uniform doping the standard approximation (so called *depletion approximation*) is that within a certain distance from the junction (denoted by x_n and x_p in Fig. 2.16), the semiconductor is completely depleted of free charges. The total depletion width $W = x_n + x_p$ is given by:

$$W = \sqrt{2\varepsilon\varepsilon_0 V_b \frac{N_D + N_A}{N_D N_A}} \tag{2.82}$$

where V_b is the built-in internal potential determined by the doping concentrations N_D and N_A:

$$V_b = k_BT \log\left[\frac{N_D N_A}{n_i^2}\right] \tag{2.83}$$

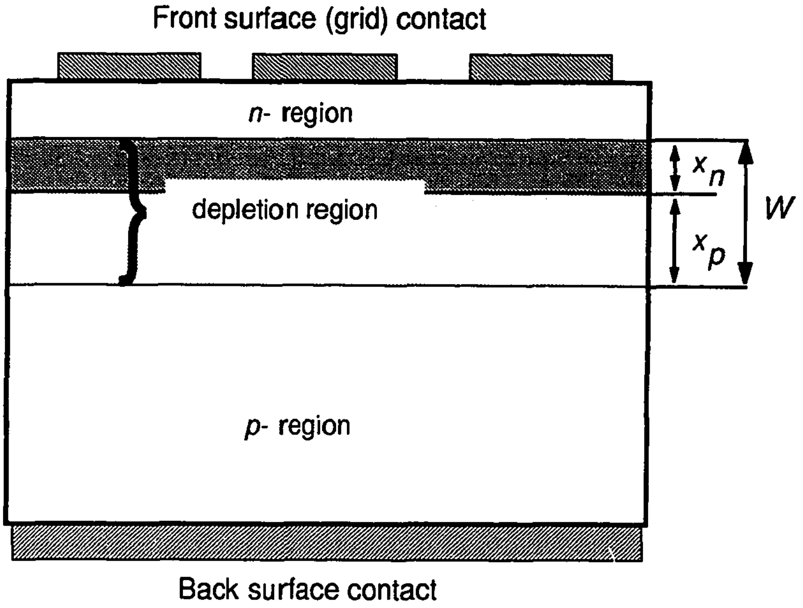

Figure 2.16: Layer diagram of a *p*-*n* junction solar cell.

and the n_i is the intrinsic carrier concentration:

$$n_i = \sqrt{N_V N_C} e^{\frac{-E_{gap}}{2k_B T}} \tag{2.84}$$

where N_V and N_C are the density of states (DOS) for valence and conduction bands, respectively.

The principle of operation of the diode is illustrated in Fig. 2.17. The absorbed photons generate electron-hole pairs inside the charge-depleted region denoted by two vertical dotted lines. The electric field, which was created as a result of the doping gradient, acts as a physical mechanism, which separates carriers and sweeps them across the depleted region. If the device is connected to an external load, a current is flowing. The voltage drop V is determined by the resistance of the external load. The illumination thus produces an output voltage V and a photocurrent $I_{ph} = I_{el} + I_{hole}$.

The amplitude of the photocurrent depends on the incident radiation as well as on the

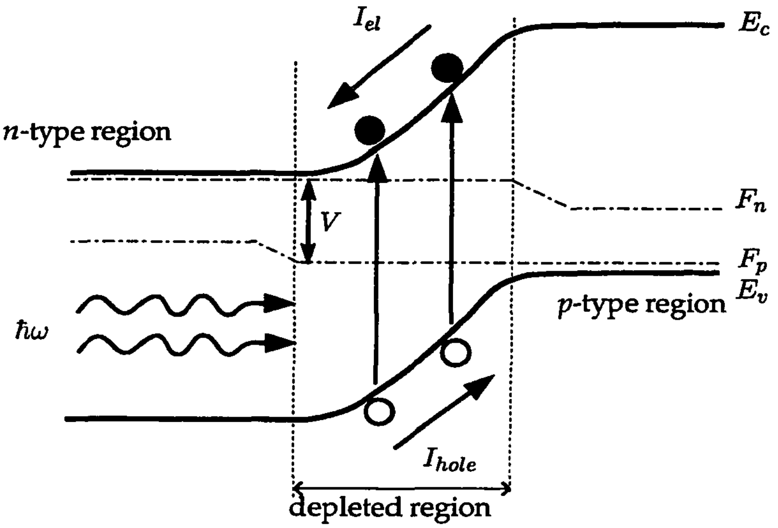

Figure 2.17: Schematic representation of the semiconductor p-n junction under illumination. E_c and E_v are conduction and valence band edges, F_n and F_p are the quasi-Fermi levels.

spectral response of the solar cell $SR(E)$. If one defines $SR(E)$ as a number of carrier pairs registered at the device's terminals per incident photon of energy E, then the photocurrent I_{ph} can be written:

$$I_{ph} = q \int_0^\infty SR(E)\Phi(E)dE \tag{2.85}$$

where q is an electron charge and $\Phi(E)$ is a photon flux. Generation of the photocurrent thus requires a matching of the spectral response with the solar spectrum.

The basic equations that describe the flux of carriers in a semiconductor under illumination are the current density equations:

$$\boldsymbol{I}_n = -q(\sigma_n \mu_n \boldsymbol{E} - D_n \nabla \sigma_n) \tag{2.86a}$$

$$\boldsymbol{I}_p = q(\sigma_p \mu_p \boldsymbol{E} - D_p \nabla \sigma_p) \tag{2.86b}$$

and continuity equations:

$$\frac{\partial \sigma_n}{\partial t_n} = +\frac{1}{q}\nabla \cdot \boldsymbol{I}_n + G - \frac{\delta \sigma_n}{\tau_n} \tag{2.87a}$$

$$\frac{\partial \sigma_p}{\partial t_p} = -\frac{1}{q}\nabla \cdot \boldsymbol{I}_p + G - \frac{\delta \sigma_p}{\tau_p} \tag{2.87b}$$

where σ_n, σ_p are the carrier densities, μ_n, μ_p are the carrier mobilities, D_n, D_p is the diffusion coefficient, G is the carrier generation rate, τ_n, τ_p is the relaxation time and $\boldsymbol{E}$ is the effective electric field, n and p indices stand for the negative and positive charges, respectively.

Under steady-state condition and using the depletion approximation one can obtain current-voltage characteristics for an ideal *p*-*n* junction solar cell:

$$I = I_s \left\{ \exp\left[\frac{eV}{kT}\right] - 1 \right\} - I_{ph} \tag{2.88}$$

where the reverse saturation current I_s is related to the device energy bandgap E_{gap} through:

$$I_s \approx \text{const} \cdot \exp\left[-\frac{E_{gap}}{kT}\right] \tag{2.89}$$

For non-ideal device with recombination losses one has to take these losses into account by adding a recombination current:

$$I_{rec} = qA \int_{-X_n}^{X_p} R(x)dx \tag{2.90}$$

where $R(x)$ is the recombination rate and A is the device area.

The maximum of the recombination rate (Eq. 2.56) occurs when $p = n$, then for the recombination current near $E_{tr} = E_{gap}/2$:

$$I_{rec} = I_{SR}\left\{\exp\frac{qV}{2k_BT} - 1\right\}; \qquad I_{SR} = \frac{qAWn_i}{2(\tau_p + \tau_n)} \tag{2.91}$$

The I–V characteristic of the *p*-*n* junction is further modified because of parasitic series, R_{ser}, and shunt, R_{shunt}, resistances, the latter is associated with the surface leakage current around the edges of solar cell device. The origin of the series resistance is a bulk resistance of semiconductor plus a contribution from the finite resistance of metal contacts and interconnections. The total expression for the current becomes:

$$\begin{aligned} I \;=\;& \text{const}_1 \cdot I_s\left\{\exp\left[\frac{e(V - IR_{ser})}{kT}\right] - 1\right\} + \\ & \text{const}_2 \cdot I_{sr}\left\{\exp\left[\frac{e(V - IR_{ser})}{kT}\right] - 1\right\} + \frac{V - IR_{ser}}{R_{sh}} - I_{ph} \end{aligned} \tag{2.92}$$

where the second term and the third term of the RHS of the equation describe a contribution from the recombination current and parasitic resistances, respectively. Fig. 2.18 shows the equivalent circuit of the solar cell based on the Eq. 2.92.

The efficiency limitations of the typical solar cell and the ways to improve the cell performance are discussed in the Section 2.3.5.

2.3.4 Fundamental Solar Cell Parameters

Before we discuss the efficiency limitations of the solar cells, we have to introduce several parameters used to describe solar cell performance. Based on the current-voltage characteristics, there are three parameters which fully characterize solar cell:

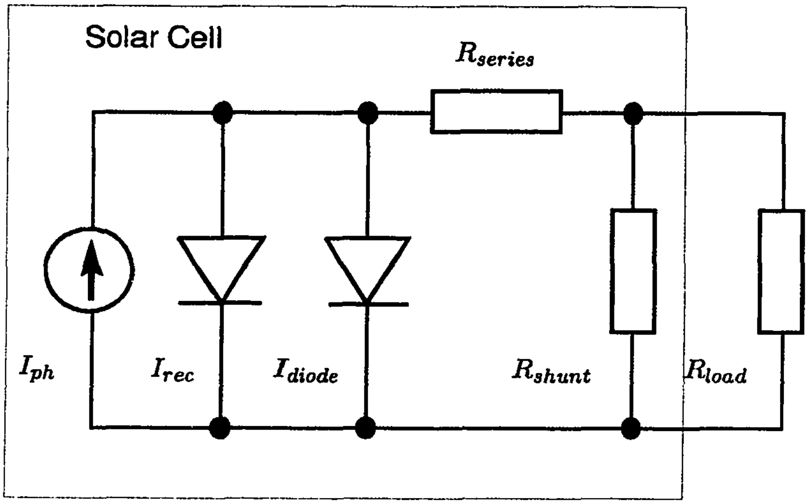

Figure 2.18: Equivalent circuit of the *p-n* junction solar cell.

1. Open circuit voltage, V_{oc}, which is measured at $I = 0$. For the ideal case, when $R_{shunt} = \infty$ and $R_{ser} = 0$, the analytical expression for the V_{oc} can be derived:

$$V_{oc} = \frac{kT}{q} \ln \left[\frac{I_{ph}}{I_s} + 1 \right] \tag{2.93}$$

2. Short circuit current, I_{sc}, which is measured at zero bias $V = 0$. For the ideal case of $R_{ser} = 0$, this parameter is equal to the photocurrent $I_{sc} = I_{ph}$.

3. In general, a solar cell should operate under conditions which produce maximum power output. To characterize how far the maximum possible power $P_{max} = I_{max} \cdot V_{max}$ for a given I-V characteristic deviates from the idealistic cell with the same I_{sc} and V_{oc} but "square" I-V curve the third parameter – fill factor FF – is introduced, which describes the "squareness" of I–V curve. The fill factor is in many ways related to the total quality of the cell - series resistance, surface leakage current and so on:

$$FF = \frac{V_{max} I_{max}}{V_{oc} I_{sc}} \tag{2.94}$$

These three parameters completely define the photovoltaic conversion efficiency of the solar cell η:

$$\eta = FF\frac{V_{oc}I_{sc}}{P_{inc}} \tag{2.95}$$

where P_{inc} is an incident solar power per unit area.

It can be seen that the improvement in η may be achieved by increasing any of these three parameters. In practice, as it will be discussed in the next section, the increase in one parameter tend to decrease the value of other parameters and vice versa.

2.3.5 Efficiency Limitations of An Ideal Single Band Solar Cell.

Several factors severely restrict the maximum efficiency achievable in any photovoltaic device. To help us to describe these factors we have adopted a graphical technique used by C. H. Henry [5] for analysis of the ideal solar cell. We will consider the case of E_{gap} = 1.32 eV (InP energy bandgap). This method is graphically illustrated in Fig. 2.19. The top curve is the photon flux $N_{ph}(E_{gap})$ absorbed by a semiconductor with an energy gap E_{gap}:

$$N_{ph}(E_{gap}) = \int_{E_{gap}}^{\infty} \Phi(E)dE dE \tag{2.96}$$

The total area under this curve is equal to the total solar power per unit area. One can identify the following power losses associated with the operation of solar cell device:

- The first and most important fundamental limitation imposed by a single-band solar cell device is that all photons with energy $\hbar\omega$ below energy gap E_{gap} ($\hbar\omega < E_{gap}$ area) are not absorbed.

- The second loss happens because of the very rapid relaxation of carriers towards their respective band edges. Thus all energy in excess of E_{gap} is lost to the heat ($\hbar\omega > E_{gap}$ area).

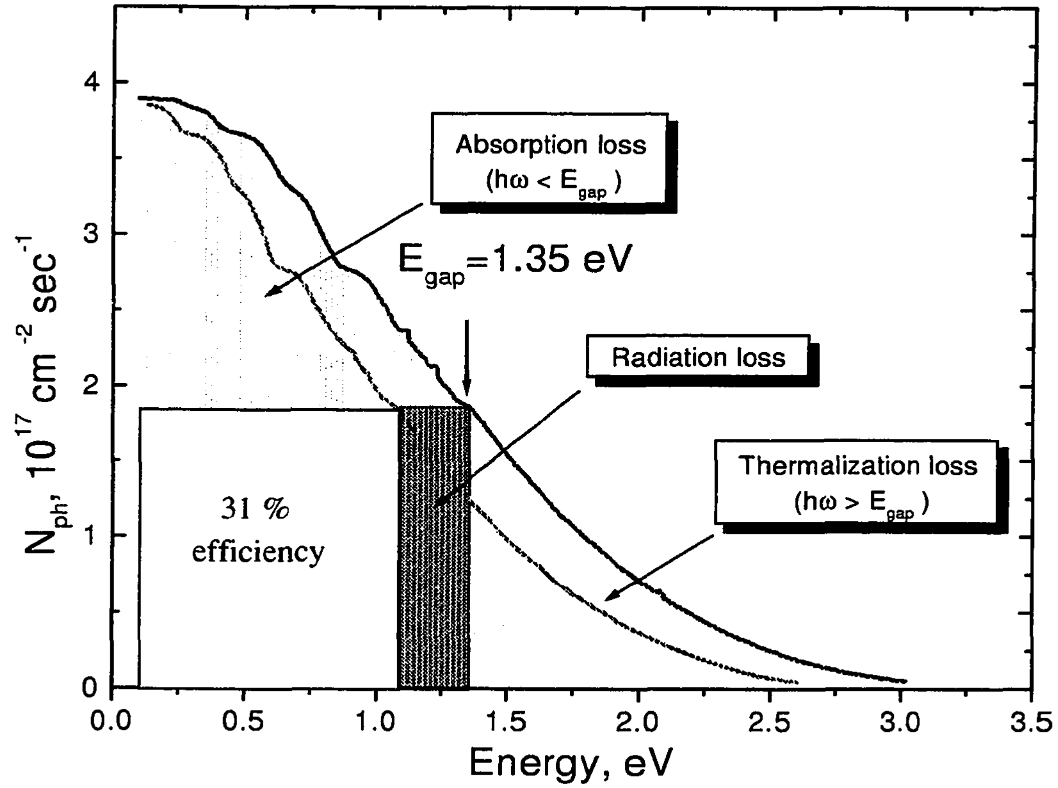

Figure 2.19: Graphical analysis of the photovoltaic efficiency of solar cell. The top curve is cell's energy bandgap E_{gap} versus absorbed photon flux $\Phi(E)$. The lower curve is a work done per absorbed photon. The area under top curve is the solar power per unit area. The shaded areas are different losses.

- Radiative recombination of the photogenerated carriers is responsible for the third kind of loss as it reduces the number of electron-hole pairs. Radiative current subtracts from the total current delivered to the load by the cell.
- For not ideal case of solar cell, one must consider various non-radiative recombination losses due to contact resistance, impurities, interface roughness and so on.

High conversion efficiency requires both high current and high voltage, however reduction of the energy gap produces not only the increase in photocurrent but also a reduction in the voltage, due to decreasing of the potential energy of collected carriers. Increasing the bandgap produces a gain in the voltage but a loss in the photocurrent. It suggests the existence of an optimum energy bandgap. Fig. 2.20 [40] shows that for a 1 sun illumination intensity the optimal band gap is $\approx$ 1.3eV. This implies that GaAs and InP are a better material choice for solar cells than Si.

2.4 Multiple Quantum Well Solar Cells

2.4.1 Multigap Solar Cells

The efficiency of ideal single band solar cell is limited to 31% (at one sun concentration). This results mainly from the *mismatch* between the broad solar spectrum and the narrow absorption spectrum of a semiconductor. Better photovoltaic efficiencies can be achieved using multiple bandgap solar cells as it is illustrated in Fig. 2.21. Fig. 2.21 shows the advantages of using multi-gap solar cells over single bandgap devices: the efficiency of a tandem cell (two bandgap) is 50% versus 37% (at 1000 sun concentration) for the single bandgap cell. The idea is to stack together several solar cells with different bandgaps in such a way that the cell with the widest gap comes topmost. The underlying cells with lower bandgaps absorb the photons which have come through the previous cells. To maximize output, all cells must be current-matched and connected in a series. In an optimally

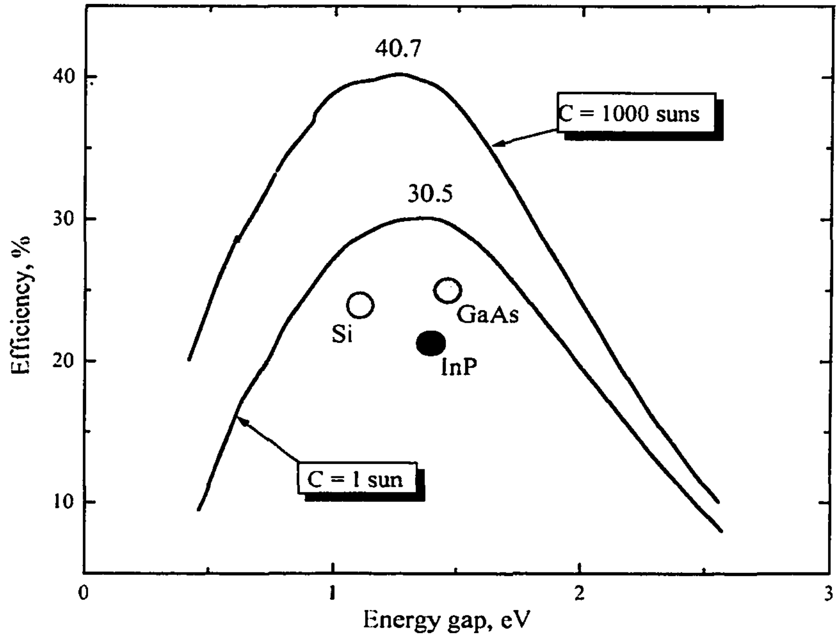

Figure 2.20: Solar cell efficiency versus device energy gap for the solar concentration of 1 and 1000 suns [5].

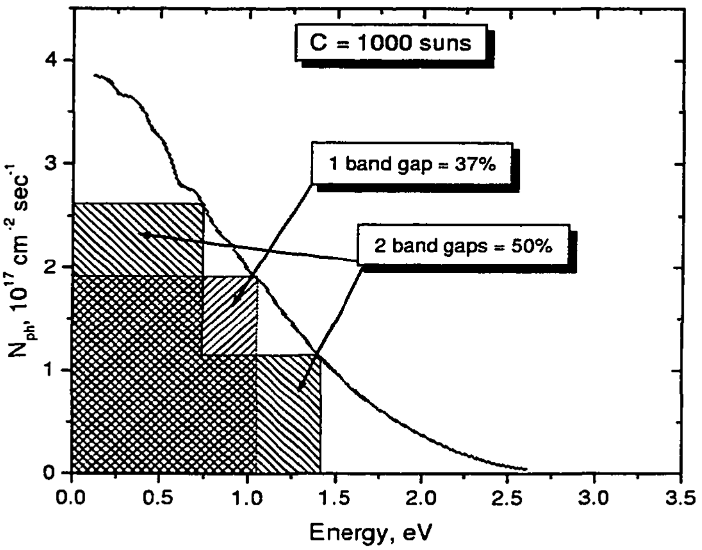

Figure 2.21: Two-band gap versus single bandgap solar cell efficiency.

designed device, all the subcells should be operated at maximum power point. In practice, it is difficult to produce good performing multi-band solar cell even in the simplest two bandgap case because of high interconnection losses.

2.4.2 MQW Solar Cells

The quantum well solar cell (QWSC) was initially proposed as an alternative multiband solar cell without disadvantages of making lossy intercell electrical connections. Typical quantum well solar cells consist of an MQW structure embedded in an undoped region (*i*-layer) of a *p*-*i*-*n* diode. Introduction of the QWs into the host *p*-*i*-*n* diode is essentially analogous to the two bandgap solar cell. *The QWs extend the lower limit of the absorption spectrum which results in the additional carrier generation and higher output current.* However, this current increase is usually accompanied by a drop in output voltage. The net result of adding QWs may or may not show an increase of performance over conventional (no

QWs) *p-i-n* structures. This condition for efficiency increase can be expressed as [41]:

$$\frac{\Delta V_{oc}}{V_{oc}} < \frac{\Delta I_{sc}}{I_{sc}} \tag{2.97}$$

It has been established experimentally [7] that quantum wells can increase the photovoltaic conversion efficiency for wide bandgap materials (AlGaAs); however for materials with a bandgap closer to the optimum (GaAs and InP) the results were rather disappointing. For instance, for the InP/InGaAs combination several authors reported [8,9] *a decrease* in the efficiency compared to a control sample. The best efficiency reported for QWSCs is an AlGaAs/GaAs 50 quantum well device with a 14% efficiency [10].

The main positive effect of the MQW region is the extension of the cell's absorption spectrum. As it was mentioned before, it is not enough. The prompt collection of the photoexcited carriers is another key ingredient of high efficiency. This is the weakest point of MQW solar cells. A characteristic feature of the QW is that it acts as a carrier trap and so to guarantee efficient operation one must provide means for efficient carrier escape and collection. The issue of efficient escape becomes very critical in the deep-well system (InP/InGaAs(P)).

Dark Current Reduction in the QWSC

Barnham *et al.* [42] have done a systematic study of the dark current in QWSCs and in homogeneous, control samples without wells formed from either the well or barrier material alone. They have measured the dependence of dark current on the band gap. Fig. 2.22 shows the dark currents of AlGaAs/GaAs SQW, MQW and control AlGaAs and GaAs samples at a fixed reference voltage (+0.6 V) plotted vs. the effective band gap for absorption E_a. E_a is taken to be an absorption onset. It is seen that the dark current of quantum well devices lie below the line joining the dark currents of the control cells. Comparisons with other material combinations (InGaAs/InP and GaInP/GaAs) have shown the same

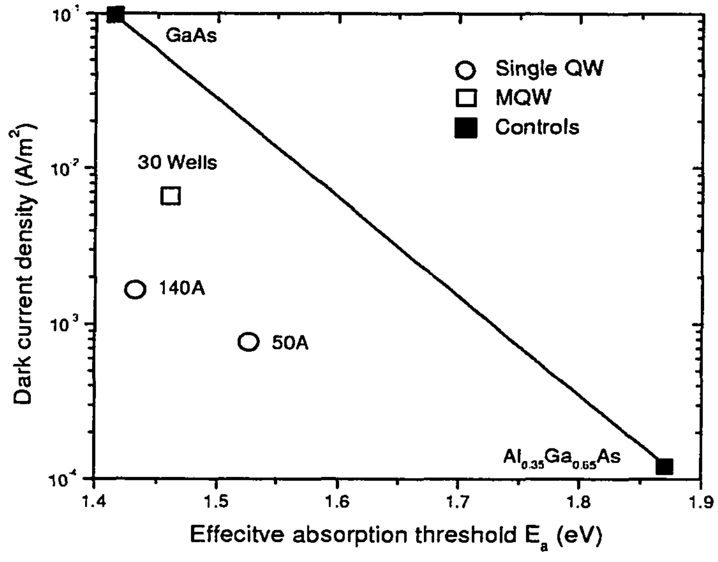

Figure 2.22: Dark current of AlGaAs/GaAs SQW, MQW and control samples at fixed bias 0.6 V plotted as a function of the effective bandgap for absorption (E_a) (from [42]).

results. The control and QW cells have demonstrated a similar exponential dependence of the dark current on the E_a, however the QW devices have a dark current more than an order of magnitude lower than the control samples. It means that the dark currents of the MQW solar cells are *significantly reduced* compared to the homogeneous cells with the same effective band gap.

The reduction of the dark current in the MQW solar cells have been related to the fact that open-circuit voltage of these cells does not fall linearly with E_a. Fig. 2.23 shows open-circuit voltages for the same samples as in Fig. 2.22. V_{oc} of the QWSCs lie *above* the line joining the V_{oc} of the control cells. Also, the increase in the V_{oc} of the QWSC is greater than increase in the E_a, i.e. $\Delta V_{oc} > \Delta E_a$.

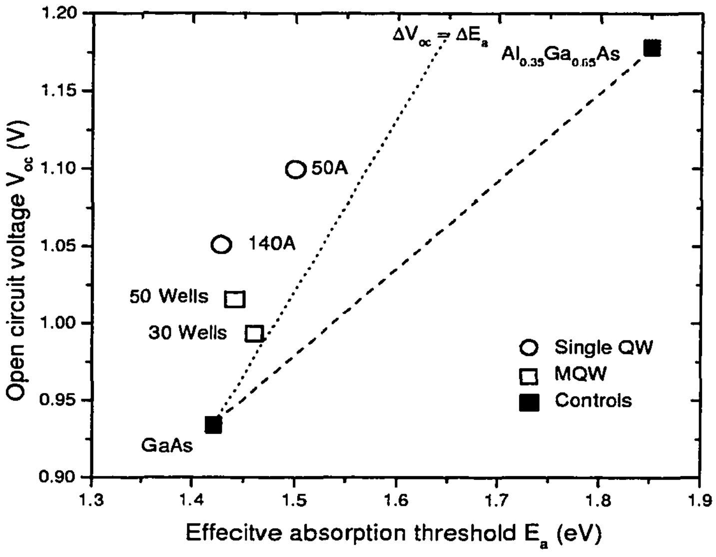

Figure 2.23: Open circuit voltage of AlGaAs/GaAs SQW, MQW and control samples vs. the effective bandgap for absorption (E_a) measured in a 3200K black body spectrum. The dotted line indicates the enhancement, above that of the control cell constructed from the well material, expected if V_{oc} is proportional to the E_a(from [42]).

2.4.3 An Ideal Model of a Quantum Well Solar Cell

Accurate modeling of MQW solar cells requires a comprehensive numerical model which, to the best of our knowledge, does not exist. Although there are some reliable solar cell simulators none of them can handle MQW heterostructures. This is not a surprise considering the complexity of the task and its relative novelty. In our work we have used an analytical model of an ideal quantum well solar cell proposed by N. G. Anderson [43] in 1995. This model was applied to study I-V characteristics of the QWSC and compared them to a bulk *baseline* cell, a solar cell without QWs.

In this model, the following simplifying assumptions are made:

1. Both cells are treated as in the ideal diode model based on the depletion approximation (see Section 2.3.3).
2. Only radiative recombination is considered. Recombination rates in the baseline and QW solar cells are described by constant radiative coefficients B_b and B_w, respectively.
3. Carrier distribution throughout the structure is described by non-degenerate Maxwell-Boltzmann statistics and quasi-Fermi levels.
4. Ohmic losses are assumed to be negligible - infinite mobility approximation.
5. The doping of n- and p-type region is the same and the valence band structure is a mirror image of the conduction band structure (the same effective masses for holes and electrons).

Within the approximations made in this model, the terminal characteristics of the quantum well solar cells are relatively insensitive to exact values of material parameters except for band gaps.

Baseline Cell Model

The current-voltage characteristic of the baseline cell is given by:

$$J(V) = J_0(e^{qV/k_bT} - 1) - J_{gen} + J_{rec} \tag{2.98}$$

where J_0 is the reverse saturation current density, and J_{rec} and J_{gen} are current densities corresponding to carrier recombination and generation in the intrinsic region, respectively. The generation current can be written as

$$J_{gen} = qW(G_B^{opt} + G_B^{th}) \tag{2.99}$$

where W is the intrinsic region width and G_B^{opt} and G_B^{th} are the average optical and thermal generation rates in the intrinsic region. The recombination current can be written as

$$J_{rec} = qWB_B n_B p_B = qWB_B n_{iB}^2 e^{qV/k_BT} \tag{2.100}$$

where n_B and p_B are the net electron and hole concentrations in the intrinsic region of the baseline cell. At $V = 0$ and no optical excitation there is an equilibrium between thermal generation and recombination rates

$$G_B^{th} = B_B n_{iB}^2 \tag{2.101}$$

The current-voltage relation for the ideal baseline cell ($J_B(V)$) then

$$J_B(V) = J_0(1+\beta)(e^{qV/k_BT} - 1) - qWG_B^{opt} \tag{2.102}$$

where

$$\beta = \frac{qWB_B n_{iB}^2}{J_0} \tag{2.103}$$

Without optical generation, Eq. 2.102 is identical to the ideal diode equation Eq. 2.88 except for the effective increase in the reverse saturation current J_O by a factor $(1+\beta)$ due to the presence of additional intrinsic layer. Then the short-circuit current and open-circuit voltage for the baseline cell are

$$\begin{aligned} J_{sc,B} &= -qWG_B^{opt} && (2.104) \\ V_{oc,B} &= \frac{k_BT}{q}\ln\left[\frac{|J_{sc,B}|+J_0(1+\beta)}{J_0(1+\beta)}\right] \approx \frac{k_BT}{q}\ln\left[\frac{|J_{sc,B}|}{J_0(1+\beta)}\right] && (2.105) \end{aligned}$$

Quantum Well Cell Model

A quantum well cell is considered to be identical to the baseline except that a fraction f_W of the intrinsic region is replaced by a quantum well material with a bandgap E_W $(E_A < E_B)$. The Eq. 2.98 is modified to include recombination and generation currents in the QWs

$$J_{QW}(V) = J_0(e^{qV/k_bT}-1) - J_{gen,B} + J_{rec,B} - J_{gen,W} + J_{rec,W} \qquad (2.106)$$

Defining generation and recombination rates G_W and R_W for the quantum wells, get

$$J_{QW}(V) = J_0(e^{qV/k_bT}-1) + qW[f_W(R_W-G_W) + (1-f_W)(R_B-G_B)] \qquad (2.107)$$

This equation can be rewritten introducing the following ratios: $\gamma_B \equiv B_W/B_B$ "oscillator enhancement factor" and $\gamma_{DOS} \equiv g_W/g_B$ "density-of-states enhancement factor", where g_W and g_B are the volume densities of states for the wells and barriers, respectively. The intrinsic carrier concentration in the quantum well material is

$$n_{iW}^2 = n_{iB}^2\gamma_{DOS}^2 e^{\Delta E/k_BT} \quad \text{where } \Delta E = E_B - E_W \qquad (2.108)$$

The Eq. 2.107

$$J_{QW}(V) = J_0[1 + r_R\beta](e^{qV/k_bT} - 1) - qW[f_W G_W^{opt}) + (1 - f_W)G_B^{opt})] \tag{2.109}$$

where r_R is the "radiative enhancement ratio"

$$r_R = 1 + f_W[\gamma_B \gamma_{DOS}^2 e^{\Delta E/k_BT} - 1] \tag{2.110}$$

This factor represents the relative increase in the net intrinsic region recombination at equilibrium due to the presence of the quantum wells. The r_R is significant even for the small bandgap differences due to its exponential dependence on the ΔE. *It is this parameter that reduces V_{oc} in this model and, consequently, the efficiency, as it is seen from the Eq. 2.112.*

The short-circuit current and open-circuit voltage for the ideal quantum well solar cell

$$J_{sc,QW} = -qW[f_W G_W^{opt} + (1 - f_W)G_B^{opt}] \tag{2.111}$$

$$V_{oc,QW} = \frac{k_BT}{q} \ln\left[\frac{|J_{sc,QW}| + J_0(1 + r_R\beta)}{J_0(1 + r_R\beta)}\right] \tag{2.112}$$

Unity Quantum Efficiency Limit

It is assumed that all incident photons with energies above the absorption edge of the cell are absorbed. In this unity quantum efficiency limit

$$J_{sc,B} = -q\Phi_B \quad \text{and} \quad J_{sc,W} = -q\Phi_W \tag{2.113}$$

where Φ_B and Φ_W are the total flux of incident photons with energies greater or equal to E_B and E_A, respectively. Defining the "generation enhancement ratio" as

$$r_G = \Phi_W/\Phi_B \tag{2.114}$$

the Eqs. 2.102, 2.105 and 2.105 become

$$J_B(V) = J_0(1+\beta)(e^{qV/k_bT}-1) - q\Phi_B \quad (2.115a)$$

$$J_{sc,B} = -q\Phi_B \quad (2.115b)$$

$$V_{oc,B} = \frac{k_BT}{q}\ln\left[\frac{q\Phi_B + J_0(1+\beta)}{J_0(1+\beta)}\right] = \frac{k_BT}{q}\ln\left[\frac{q\Phi_B}{J_0(1+\beta)}+1\right] \quad (2.115c)$$

and for the quantum well cell

$$J_{QW}(V) = J_0[1+r_R\beta](e^{qV/k_bT}-1) - qr_G\Phi_B \quad (2.116a)$$

$$J_{sc,QW} = -q\Phi_W = -qr_G\Phi_B \quad (2.116b)$$

$$V_{oc,QW} = \frac{k_BT}{q}\ln\left[\frac{qr_G\Phi_B + J_0(1+r_R\beta)}{J_0(1+r_R\beta)}\right] = \frac{k_BT}{q}\ln\left[\frac{qr_G\Phi_B}{J_0(1+r_R\beta)}+1\right] \quad (2.116c)$$

Comparison of Eq. 2.115 and Eq. 2.116 reveals that MQW solar cell *will* outperform only if the increase in the current described by the parameter r_G (absorption enhancement) will not be shadowed by the decrease in the output voltage due to the introduction of r_R, a radiation rate increase.

2.5 Numerical Solution of the Poisson's Equation in Semiconductor Heterostructures

Knowledge of the charge and field distribution inside a *p*-*n*-junction is essential in semiconductor device modeling. We felt it was necessary to develop a software capable of calculating these functions. The model described here is based on the Lundstrom and Schuelke work [44]. Carrier transport is described in terms of drift and diffusion. High-field transport and all quantum mechanical effects (quantum confinement and transport) are not included. Despite these limitations the model proved to be very useful in interpretation of experimental data.

In a compositionally nonuniform semiconductor, a nonlinear one-dimensional Poisson equation for the electrostatic potential $V(\vec{r})$ can be written as

$$\nabla[\varepsilon(x)\nabla V(x)] = -\rho(V(x)) = e(-n(V(x)) + p(V(x)) + N_D^+(V(x)) - N_A^-(V(x))) \quad (2.117)$$

where $\varepsilon(x)$ is the position-dependent dielectric constant, ρ is the total charge density, n and p electron and hole concentrations, and N_D^+ and N_A^- ionized donor and acceptor concentrations.

In addition to forces from the macroscopic electric field, forces associated with structure non-uniformity are accounted for by two band parameters, V_n and V_p

$$\begin{aligned} qV_p &= -(\chi(x) - \chi_r) - (E_g(x) - E_{gr}) + k_BT\log\left[\frac{N_v(x)}{N_{vr}}\right] && (2.118a) \\ &\quad + k_BT\log\left[\frac{\mathcal{F}_{1/2}(\eta_v)}{\exp(\eta_v)}\right] \\ qV_n &= \chi(x) - \chi_r + k_BT\log\left[\frac{N_c(x)}{N_{cr}}\right] + k_BT\log\left[\frac{\mathcal{F}_{1/2}(\eta_c)}{\exp(\eta_c)}\right] && (2.118b) \end{aligned}$$

where

$$\begin{aligned} \eta_c &= (F_n - E_c)/k_BT && (2.119a) \\ \eta_v &= (E_v - F_p)/k_BT && (2.119b) \end{aligned}$$

and $\mathcal{F}_{1/2}$ is the Fermi-Dirac integral of order 1/2. The last terms in Eq. 2.118 are due to the influence of Fermi-Dirac statistics and are zero when Boltzmann (non-degenerate semiconductor) statistics is assumed. The subscript r refers to the values of the various parameters at the reference location within the heterostructure. The position-dependent parameter χ is the difference between the conduction band edge and an internal reference energy level.

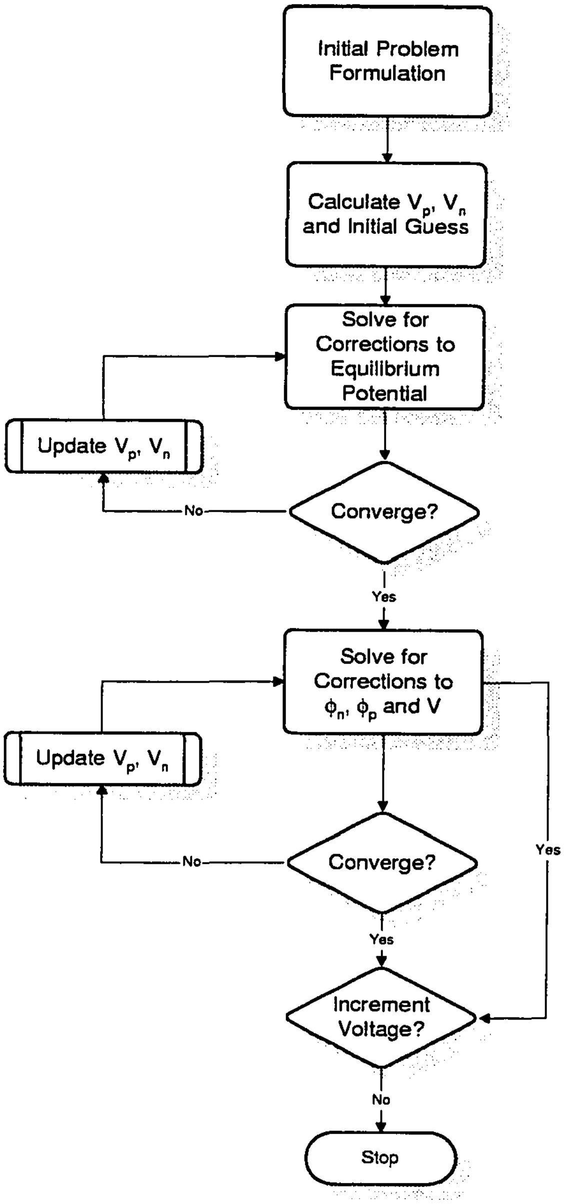

Figure 2.24: Flowchart of the Poisson solver.

It is useful to relate the carrier densities to the quasi-Fermi levels

$$\phi_p = (E_f - F_p)/q \quad (2.120a)$$

$$\phi_n = (E_f - F_n)/q \quad (2.120b)$$

where E_f is the equilibrium Fermi level and F_p and F_n are the quasi-Fermi levels for holes and electrons. Substituting Eq. 2.120 in expressions for p and n

$$p = n_{ir}e^{-q(V-V_p-\phi_p)/k_BT} \quad (2.121a)$$

$$n = n_{ir}e^{q(V+V_n-\phi_n)/k_BT} \quad (2.121b)$$

Poisson's equation becomes

$$\nabla^2 V + \frac{1}{\eta}\nabla\eta \cdot \nabla V = -\frac{q}{\eta\eta_0}(n_{ir}e^{-q(V-V_p-\phi_p)/k_BT} - n_{ir}e^{q(V+V_n-\phi_n)/k_BT} + N_D^+ - N_A^-) \quad (2.122)$$

$\phi_p = \phi_n = 0$ describes heterostructure in equilibrium.

Boundary conditions are obtained from the requirement of the space-charge neutrality and assuming equilibrium at the contact. Then both sides of Eq. 2.122 are zero, and V

$$V = \frac{V_p - V_n}{2} + sign(D)\frac{k_BT}{q}\log\left[|\frac{1}{2}D|e^{-q(V_p+V_n)/2k_BT} + \sqrt{\frac{1}{4}D^2e^{-q(V_p+V_n)/2k_BT} + 1}\right] \quad (2.123)$$

where $D = (N_D^+ - N_A^-)/n_{ir}$ is the net normalized doping density.

The Eq. 2.122 is discretized by the finite difference technique and solved using Newton-Raphson iteration method [45]. The flow chart of the program code written in *Mathematica®* language is shown in Fig. 2.24. The code of the program is on the accompanying floppy disk.

2.6 Conclusions

- Optoelectronic devices based on quantum well structures offer flexibility and tunability not easily available in conventional (non-QW) devices.
- Multiband solar cells promise to deliver significantly higher photoconversion efficiencies.
- MQW-based solar cells have a potential of multiband solar cells without difficulties associated with conventional non-QW multiband solar cells.
- The main obstacle to achieve high efficiency in MQW solar cells - increased radiative and non-radiative losses compared to non-QW devices.
- New designs and approaches are needed to overcome these shortcomings.

Chapter 3

Experimental Setup

3.1 Introduction

In our study we have employed several experimental techniques to conduct our investigations. Photoluminescence (PL) measurements were used to determine fundamental energy gaps E_{gap} of the samples. Temperature dependence of the PL was studied to investigate carrier escape and radiative recombination processes. For multilayer samples, bias dependence of PL has helped to identify the origin of various bands in the PL spectra.

Photocurrent (PC) measurements were crucial in investigating spectral response (photogenerated current as a function of exciting wavelength) of the samples. Rich PC MQW spectra were used to identify various energy states in the quantum well. Temperature and bias dependence of PC were measured to investigate carrier escape processes in the MQW samples and to investigate resonant transfer alignment. Information extracted from PC spectra were used to estimate the effect of the strain and electric field (Quantum Confined Stark Effect) on quantum well states.

I-V or dark current measurements has been used to characterize the properties of semiconductor $p-n$ junction, as well as to provide an estimate of the quality of contact wiring. Temperature dependence of I-V curves was measured to study resonant transfer in MQW samples.

Solar cell efficiency measurements, which are essentially I-V measurements conducted under illumination by standard white light source, were performed to determine photovoltaic parameters such as V_{oc}, I_{sc}, FF and η of all samples.

3.2 Photoluminescence Measurements

PL measurements were conducted for the following purposes:

- To measure the fundamental energy gap E_{gap} of semiconductor samples
- To estimate a relative strength of radiative recombination
- To study temperature dependence of E_{gap} of InGaAsP MQW samples
- To investigate resonant tunneling transfer in MQW samples

The experimental setup for measuring photoluminescence spectra is shown in Fig. 3.1. The photoluminescence emission excited by a **Laser** beam is collected and focused on the entrance slit of the spectrometer by two lenses, **L1** and **L2**. Since the QW PL spectra can easily span a wavelength range of 1 μ and more, achromatic lenses have been used to reduce spectral chromatic abberation. The pump laser emission is blocked by an appropriate longpass filter **F** placed in front of the entrance slit. Sample emission, passed through the entrance slit, is dispersed on the spectrometer grating **G** and detected on the exit slit by a **Photodetector**. The signal from the **Photodetector** is processed by a **Lock-In** amplifier and stored in a computer **(PC)**. A Source–Measure Unit **(I–V)** is used to control voltage bias applied to the **Sample**. For low temperature measurements, the **Sample** has been placed in a **Cryostat**. A neutral density wheel **(ND Filter Wheel)** was used to control incident light intensity.

3.2.1 Description of the Major Components

TRIAX-320 spectrometer

TRIAX-320 [46] is a 0.32 m Ĉzerny-Turner scanning imaging spectrometer equipped with an automated on-axis triple grating turret and a direct grating drive mechanism. Table 3.1 contains a complete list of the TRIAX specifications. The front exit port can be fitted with an optional detector array or a charge-coupled device (CCD) camera to provide multichannel detection capability. The slit width can be varied in the range of 0...2 mm in steps of 12.5 μm.

All functions of the spectrometer (wavelength positioning, slit width, choice of grating, exit swing away mirror) are controlled via an IEEE-488 interface. Three different gratings were installed on the turret:

1. 250 nm blazed (1200 grooves/mm)
2. 500 nm blazed (1200 grooves/mm)
3. 1000 nm blazed (600 grooves/mm)

This allows us to cover 200-2800 nm range of wavelengths.

Parameter	**Nominal value**
Focal Length	0.32 meter
Entrance Aperture Ratio	f/4.1
Image Magnification on Exit	1.00
Scanning Range	0-1400 nm
Focal Plane	30 mm × 12 mm
Spectral Dispersion with 1200 g/mm grating	2.64 nm/mm
Wavelength Positioning Accuracy	±0.3 nm
Wavelength Repeatability	±0.06 nm

Table 3.1: Specifications of the TRIAX 320 spectrometer

Keithley 236 Source–Measure Unit

The Keithley 236 Source–Measure Unit [47] (SMU) has been used to measure the *dc* current through the samples in all I-V and solar cell efficiency measurements. In photocurrent measurements, it has served as the *dc* voltage source. The Keithley 236 SMU is really four sensitive instruments in one: electrometer, digital multimeter (DMM), current source, and voltage source. The 236 SMU is fully programmable instrument, capable of sourcing and measuring voltage and current simultaneously. The SMU can source voltage from 100 μV to 110 V, and current from 100 fA to 100 mA. It can also measure voltage from 10 μV to 110 V and current from 10 fA to 100 mA.

The measurements can be taken and recorded in an internal memory along with corresponding values of the source voltage or current and time. Up to 1000 values of each variable correlated in time can be stored in the internal buffer and later obtained over the IEEE-488 bus. The SMU can be programmed to perform source-measurement as a function of a stepped voltage or current (sweep measurements). Voltage and current can be swept linearly, logarithmically, or pulsed.

Stanford Research Lock–In Amplifier SR830

The SR830 lock-in amplifier was used to detect PL and PC signals coming either from the photodetector (PL measurements) or directly from the sample (PC measurements). Lock-in amplifiers use a technique known as phase-sensitive detection to single out the component of the signal at a specific reference frequency and phase. The sample is excited at a fixed frequency ω_{ref} (provided by a **Chopper** in our case) and a lock-in detects the response from the experiment at the reference frequency. $V_{sig}(t)$ is the true signal amplitude and $V_{sig}(t)\sin(\omega_{ref}t + \theta_{sig})$ is the total signal seen on the lock-in input. The lock-in generates its own reference signal $V_L(t)\sin(\omega_L t + \theta_{ref})$. The SR830 [48] amplifies the input signal and multiplies it by the lock-in reference using a *phase-sensitive detector* (PSD) and integrates over *integration time*, T_{int}. The output of the PSD is the product of two sine waves, which can be written as a sum of two cosines:

$$\begin{aligned} V_{psd} &= \frac{1}{2}V_{sig}V_L\cos[(\omega_{ref}-\omega_L)t+\theta_{sig}-\theta_{ref}] - \\ &\frac{1}{2}V_{sig}V_L\cos[(\omega_{ref}+\omega_L)t+\theta_{sig}+\theta_{ref}] \end{aligned} \tag{3.1}$$

If $\omega_{ref}=\omega_L$, the difference frequency term $(\omega_{ref}-\omega_L)$ in Eq. 3.1 will be a DC signal which can be extracted using a low-pass filter. The SR830 is equipped with two PSDs. The second PSD multiplies the signal with the reference oscillator shifted by 90°, so its low pass filtered output will be

$$V_{psd2}=\frac{1}{2}V_{sig}V_L\sin(\theta_{sig}-\theta_{ref}) \tag{3.2}$$

By computing the square root of the sum of V_{psd} and V_{psd2} the original signal can be restored:

$$R=\sqrt{V_{psd}^2+V_{psd2}^2}=V_{sig}V_L \tag{3.3}$$

R measures the signal amplitude and does not depend on the phase between the signal and lock-in reference.

The PSD and low pass filter only detect signals whose frequencies are very close to the lock-in reference frequency. Noise signals at frequencies other than the reference are rejected and do not affect the measurement. SR830 implements digital signal processing (DSP), which allows us to eliminate the drift, offset and nonlinearities inherent in analog lock-ins.

Laser

Two laser sources were used in the experiment:

- **Spectra Physics** Nd^{3+}:YAG mode-locked laser (λ = 1064 nm, P_{max} = 8 W) with a second harmonic generation system (λ = 532 nm, P_{max} = 1.5 W).

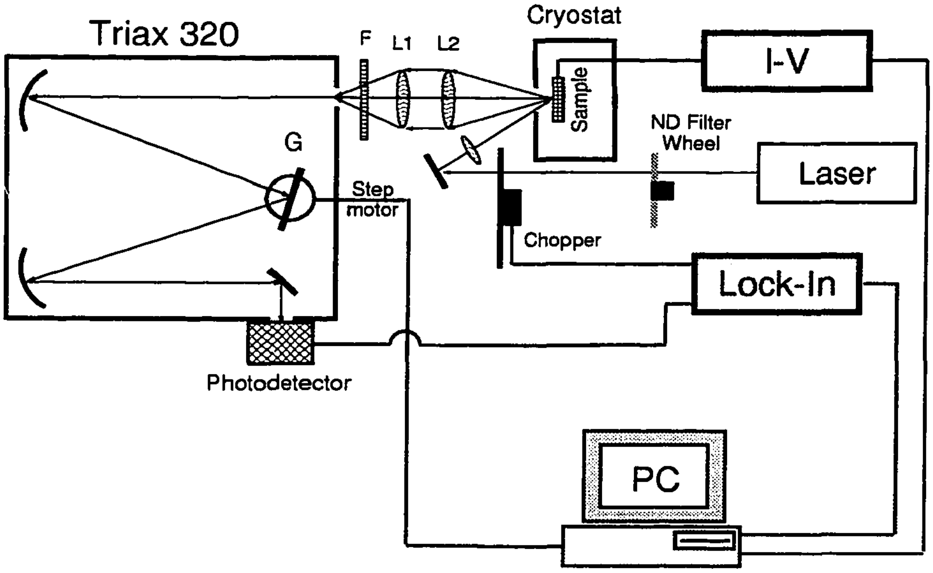

Figure 3.1: Experimental setup for photoluminescence measurements. F is the long pass filter, L1 and L2 – the achromatic lenses, G – the grating turret.

- **SDL** AlGaAs/GaAs diode laser ($\lambda = 681$ nm, $P_{max} = 0.5$ W).

Due to high divergence of the diode laser beam, a short focused lens ($F = 4$mm) was used to collimate the beam.

Photodetector

For PL measurements ranging from 800 nm and above, thermoelectrically cooled InGaAs photodetector was used. The working range of this detector is 800-1800 nm. In the visible range (400-800 nm), Si detector was used.

Optical Cryostat

In low temperature experiments we have used a Janis Research ST-4 cryostat equipped with a Lake Shore Cryotronics 805 temperature controller. For I-V measurements the cryostat cooling finger was fitted with additional necessary wires and contacts.

PC with the GPIB controller card

Most experiments were controlled by a personal computer PC (Micron® Millennia Xru with Intel® Pentium II 266MHz). The PC was equipped with National Instruments® IEEE-488 General Purpose Interface Bus (GPIB) controller card, which allowed one to control simultaneously up to 15 GPIB instruments.

All major components of the experimental setup were equipped with a GPIB interface which greatly facilitated the task of data acquisition. GPIB devices communicate with other GPIB devices by sending device-dependent messages and interface messages through the interface system. The GPIB controller placed inside the PC manages all communication exchange.

To control the experiment we have written software (*Ke236*) using National Instruments® LabWindows/CVI IDE [49] (Integrated Development Environment). Full C code of the program *Ke236* (see Appendix B) is provided on the accompanying floppy disk due to its

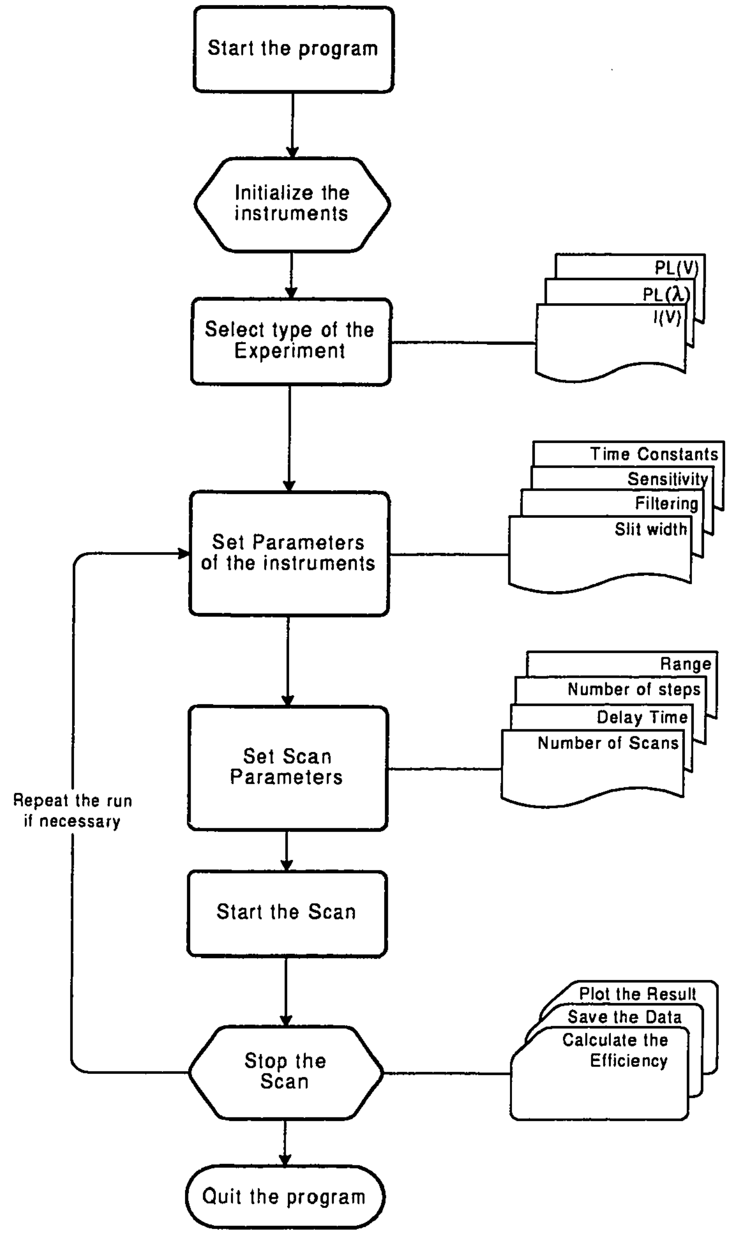

Figure 3.2: Flowchart of the *Ke236* program - the program to control a data acquisition using the Keithley 236 SMU, SR830 Lock-In and Triax-320.

large printed size (about 120 pages). Fig. 3.2 shows a flowchart of the program. The program provides remote control over most of the functions of the spectrometer, the lock-in amplifier and the SMU unit.

Using this program the following types of measurements can be made:

- Current-voltage measurements
- Photoluminescence intensity as a function of wavelength
- Photoluminescence intensity as a function of bias
- Photocurrent intensity as a function of wavelength
- Photocurrent intensity as a function of bias
- Solar cell performance measurements

3.3 Photocurrent Measurements

Photocurrent measurements were conducted for the following purposes:

- To get information about spectral response of the sample.
- In MQW samples, PC spectra were used to identify various optical transitions occurring inside quantum well. This information was later used to completely characterize quantum well energy states and to investigate the effect of strain, temperature and electric field on these states.
- PC spectra were also used to investigate resonant enhancement of PC occurred in MQW samples with built-in sequential resonant tunneling.

Information learned from the PC measurements led to an improved MQW solar cell design. PC measurements have employed the setup shown in Fig. 3.3. The light from a quartz halogen tungsten lamp (**QHT lamp**) is collected and focused by condenser optics

(Condenser) on the entrance slit of the spectrometer. To avoid the interference from the second order detection, a longpass filter **F** was placed in front of the slit. The light from the QHT lamp was then dispersed in the monochromator and focused on the sample. The generated photocurrent was detected using lock-in technique described earlier.

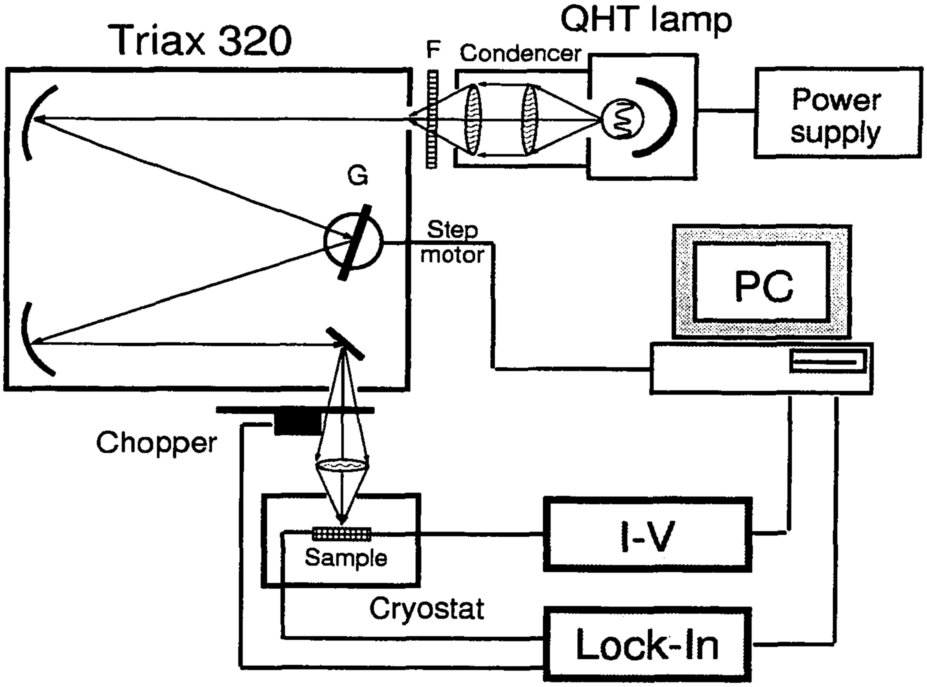

Figure 3.3: Experimental setup for the photocurrent measurements. F is the longpass filter, G – the grating turret

The scheme of the sample electrical connections is shown in Fig. 3.4. The **Sample** was connected in a series with a 100 Ω load resistor $\mathbf{R}_{load}$. The lock-in amplifier measured the voltage difference between $\mathbf{R}_{load}$ terminals. The advantage of the differential amplifier is that a noise pick-up on the shields does not translate into signal noise since the shields are ignored. Both signal connections were shielded from spurious pick-up. The voltage signal has been later converted to the current values.

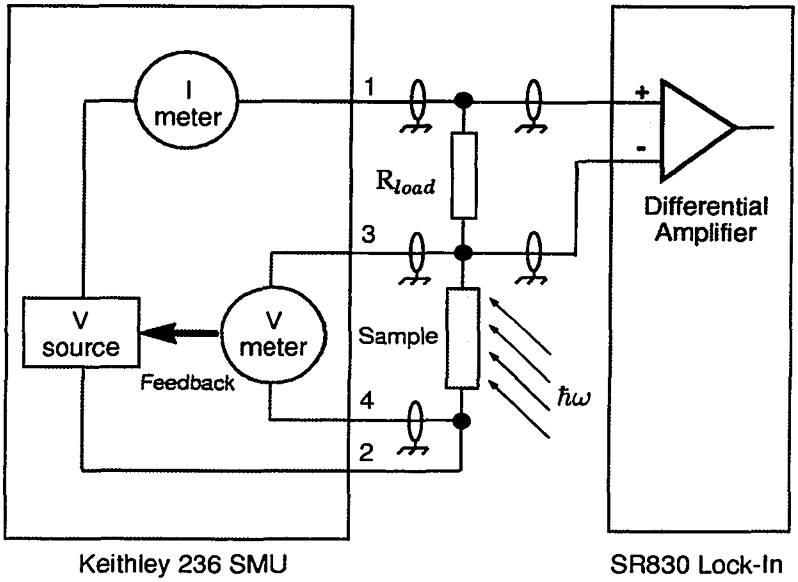

Figure 3.4: Electrical circuitry of I–V measurements.

To control voltage bias on the sample, a four-wire source-measurement method (*Kelvin measurements*) was employed. It allowed us to bypass the voltage drop across the source wire leads (1 and 2 in Fig. 3.4) by bringing two high impedance voltage measurement wire leads out to the sample. Since there is very little current in the measurement circuit, there is effectively no I–R drop in the measurement leads, and the voltage seen by the measurement terminals is the same as the voltage developed across the sample.

3.3.1 Description of the Major Components

Aside from the quartz halogen tungsten (QHT) lamp all components shown in Fig. 3.3 were the same as described in the Sec. 3.2.

QHT lamp

Quartz halogen tungsten lamps are popular visible and near-IR light sources because of their smooth spectral curve and stable output. The spectrum emitted by the QHT lamps resembles that of the ideal black body. The spectral output of the QHT lamp is characterized by its *color temperature* T_{color}. This is the temperature in K of a black body object which emits light of similar color balance as the tungsten halogen lamp. The typical color temperature of the QHT lamp is 2800-3000 K.

The light source used in our experiments was a 100 W Instruments S.A. LSH-T100 Tungsten Source. The lamp was mounted in the air-cooled housing, and the housing itself was designed to be $f/\#$-matched to the spectrometer.

3.4 Current-Voltage and Photovoltaic Efficiency Measurements

Current-voltage (I-V) measurements are important in investigation of the properties of $p-n$ junction and the overall quality of the sample wiring. Temperature dependence of the I-V curves has helped to identify the origin of non-radiative recombination in some samples. Photovoltaic efficiency measurements is a variation of I-V measurements performed under illumination by a standard white light source with a known spectral distribution.

Fig. 3.5 shows the experimental setup used to perform I-V measurements. The sample is illuminated by the high-power 1kW QHT lamp. To achieve high illumination uniformity a scattering plate (Scatterer) was introduced in the optical path between the light source and the sample. The current-voltage characteristic is then recorded on the SMU using the *Ke236* program described before. Before the actual measurements were done, the sample was replaced with a Newport Optical Meter Detector [50] and the whole system was tuned to the required light intensity – typically, 100 mW/cm^2, which corresponds to approximately AM1.0 condition. The intensity of the light can be adjusted using an ND filter wheel. After measurements are taken, the solar cell parameters are automatically calculated by the *Ke236* program.

The following describes steps taken to calculate the efficiency:

1. The area of the sample is measured.
2. The intensity of the white light is set to the required level using ND filter set and a Newport Optical Meter.
3. The sample is placed in the holder, illuminated and the I-V characteristic is taken using the setup shown in Fig. 3.5 and the *Ke236* program.
4. *Ke236* finds I_{sc}, V_{oc} on the I-V curve, finds the maximum power point on the I-V curve and corresponding V_m and I_m. The maximum power point is found by searching for the maximum of the $I \times V$ product. The search routines are the standard functions of the *LabWindows* analysis library.
5. After calculating V_m and I_m, the user must enter the sample area, S, and illumination intensity, P_{inc}, into the program which then calculates the efficiency η and fill factor FF according the formula:

$$\eta = \frac{V_m I_m}{S P_{inc}} \times 100 \qquad FF = \frac{V_m I_m}{V_{oc} I_{sc}} \times 100 \tag{3.4}$$

3.5 Sample Growth and Preparation

3.5.1 Growth and Processing

Both sample growth and metallization were done by Dr. C. L. Reynolds's group of Lucent Technologies in Breinigsville, PA. All samples were grown in a low-pressure metalorganic chemical vapor deposition (MOVPE) reactor. MOVPE is a common method of growing *epitaxial* structures. To ensure high quality of the grown thin layer, the crystal

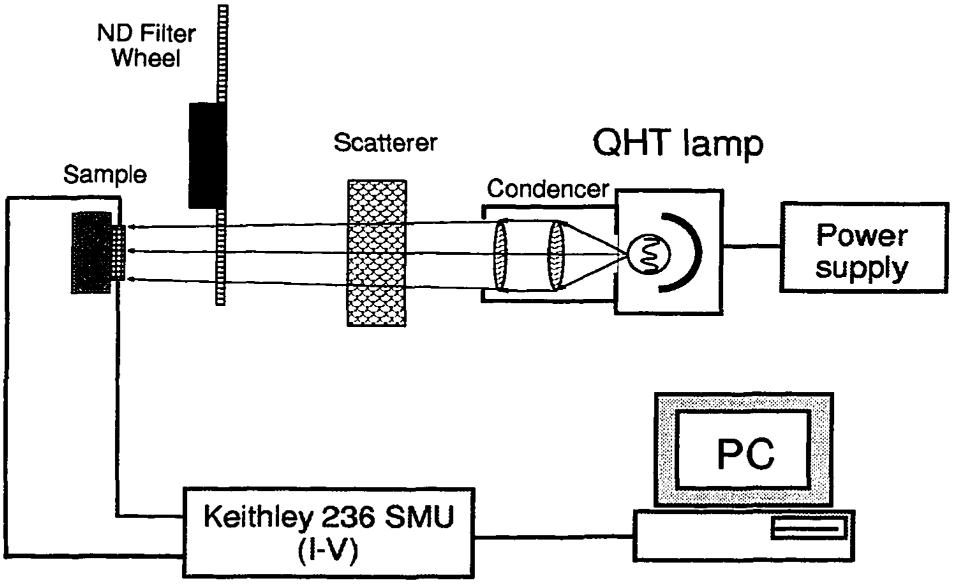

Figure 3.5: Experimental setup for current-voltage and photovoltaic efficiency measurements.

structure of this layer should be similar to the underlying bulk substrate. In such cases the atoms forming the thin layer will arrange themselves to form a single crystal with the same crystal orientation as the substrate. The resulting layer is said to be deposited *epitaxially* on the substrate. The deposition of a layer on a bulk substrate of the same chemical composition is known as a *homoepitaxy* (e.g. GaAs on GaAs), while the deposition of the layer of similar structure but different chemical composition is known as a *heteroepitaxy* (e.g. InGaAs on InP).

Epitaxial layers or *epilayers* can be grown from solid, liquid or gas phases. In gas phase epitaxy the growth rate is controlled by the amount of gas flow. The method of growing epitaxial layers from metalorganic gases is known as *metalorganic chemical vapor deposition* or MOVPE for short.

To make a grid metal contact on the top of the cell a process known as *photolithography* was used. The process is very similar to conventional photo film processing. Photolithography involves the photographic transfer of a pattern to the semiconductor wafer that will later be removed. The process consists of the primary steps shown below:

1. Deposition of a SiO_2 layer on the wafer.
2. Creation of a pattern mask. In our case it was a grid pattern.
3. Special polymer *photoresist* is applied to the surface of the wafer to form a thin film.
4. The film is exposed to a light source, typically UV, that shines through the pattern mask.
5. The film is developed. The exposed areas of the photoresist (where metal will be deposited) are removed.
6. The SiO_2 is etched off.
7. The metal is deposited.
8. Lift-off of the mask.
9. The metal is annealed to form an alloy.

Consequent sample preparation included cutting the wafer into manageable pieces, and wiring and placing samples into the standard holder.

3.5.2 Cutting

Fig. 3.6 shows pictures (top side) of two InGaAsP/InP wafers. The diameter of the wafer is 2 inch. The wafer has to be cut into smaller pieces ($\approx 10 \times 5$ mm) for the following reasons:

- The upper measurable current limit for the Keithley 236 SMU is 100 mA. Typical current density in the solar cell can easily reach 200 mA/cm^2. This makes it impossible to handle samples with the area more than 0.5 cm^2.

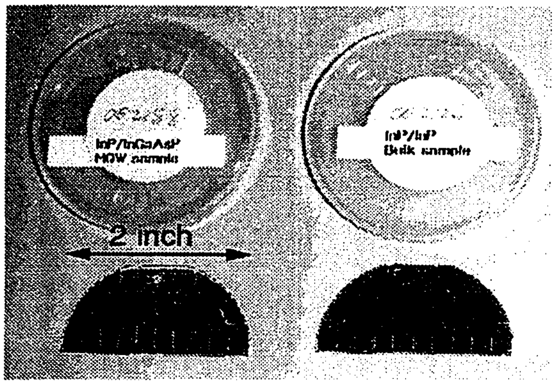

Figure 3.6: Top view of the MQW InGaAsP/InP sample #OE2188 (left) and InP control sample #OE2126 (right)

- Convenience. All samples were cut to fit into the standard DIP plug.
- Difficulty to produce a uniform illumination on the wide area while measuring photovoltaic conversion efficiency.

3.5.3 Wiring

All samples were wired using 0.127mm diameter gold wire (Aldrich® catalog #32,652-6) and placed into standard DIP gold-plated 14-pin header plug (JAMECO® catalog #37129). Fig. 3.7 shows one of the samples in the DIP plug. Wires were attached using either soldering iron or conductive silver paint.

Soldering was done using In 0.5mm wire on the XY-TRONICS temperature controlled soldering station XY9-60D with temperature set to 450 F (just above In melting point). Due to fragile nature of the epitaxial layers *extreme caution* must be taken to prevent samples from damage. Soldering must be done as quickly as possible using the smallest available soldering tip. Overexposing a sample to heat will cause In diffusion inside the sample and partial shorting of the *p-n* junction. The sense of the "right" amount of time and heat can only be acquired by making several test samples. Fig. 3.8 shows the effect of heating on

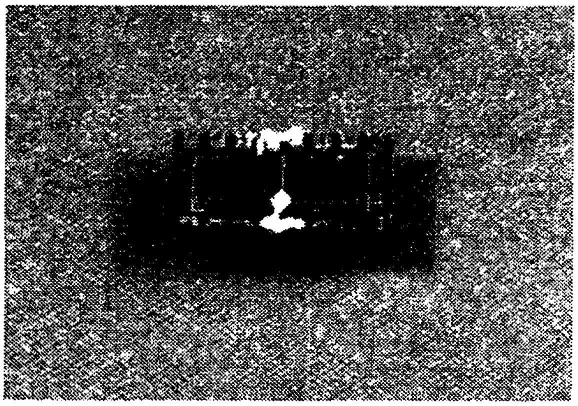

Figure 3.7: View of the InGaAsP/InP sample wired and placed in the DIP header plug.

the current voltage characteristics. "Bad" wiring resulted in significant (almost 2 order) increase of the current magnitude in the bias range of -1.5... +0.7V.

The alternative to the soldering is gluing the wires using high-conductive silver paint (GS Thorsen, Inc. catalog #22-202). Since this does not involve any heating the results are more consistent. At the same time I-V characteristics of the samples wired with the silver paint can be used as a reference for the samples wired with soldering. However, the experiment showed that silver paint contacts does not withstand low temperature and all low temperature experiments were made with "soldered" samples.

Fig. 3.9 shows a DIP plug with the solar cell placed in the sample holder. The holder was built around Aries® Universal ZIF (Zero Insertion Socket) which allowed safe, reliable and convenient sample holding and exchanging.

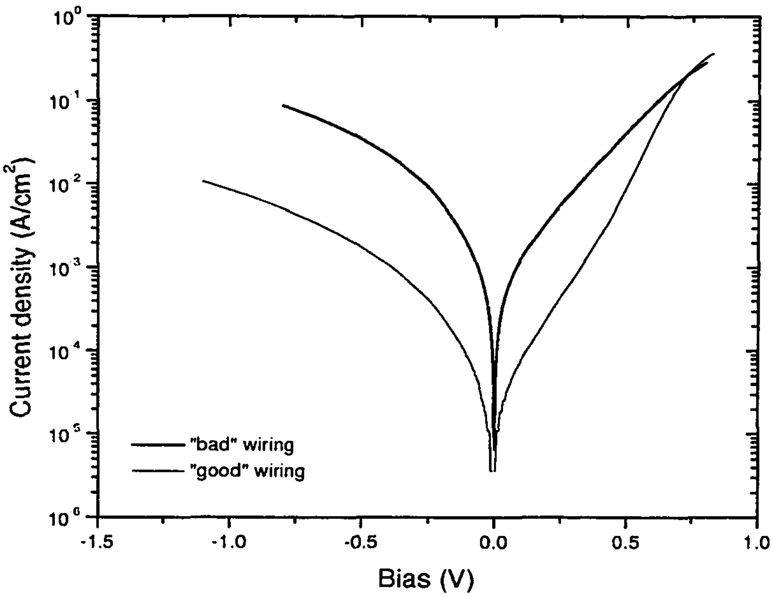

Figure 3.8: Effect of the heat on the I-V characteristics of the samples.

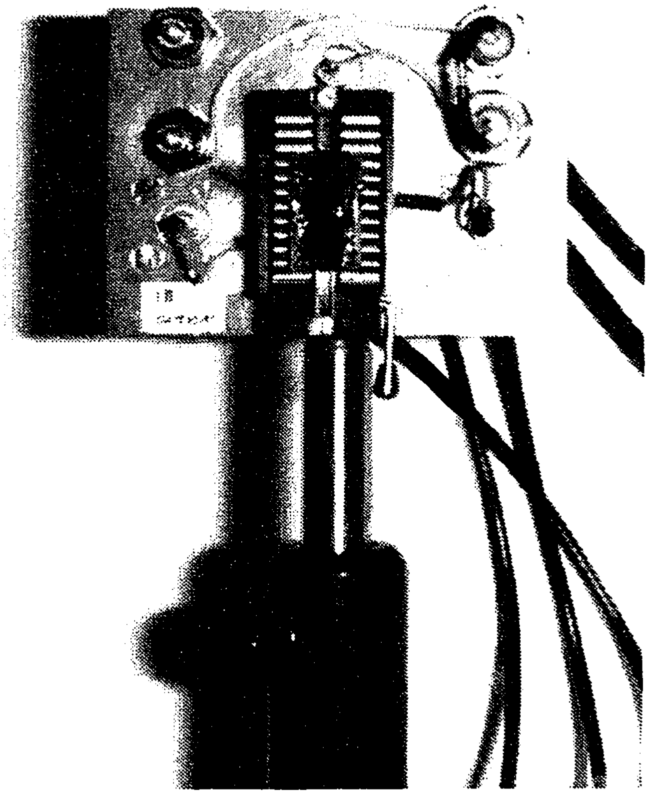

Figure 3.9: View of the InGaAsP/InP sample inserted in the ZIF socket.

Chapter 4

Investigation of Photoluminescence and Photocurrent in $In_xGa_{1-x}As_yP_{1-y}$ Strained MQW Heterostructures

4.1 Introduction

In this chapter we present our studies on the photoluminescent and photoconductive properties of MQW InGaAsP/InP *p-i-n* heterostructures. Two samples with different barrier width were investigated using photoluminescence, photocurrent and dark current measurements [51]. The focus of the study is the basic properties of the MQW structures: quantum well energy states, the effect of the strain, temperature and electric field on these states, and the escape processes in quantum wells. The origin of recombination losses is analyzed. The relation of these properties with structural and compositional parameters of heterostructures is also a subject of investigation as it is important for an understanding of the basic physics of MQW devices.

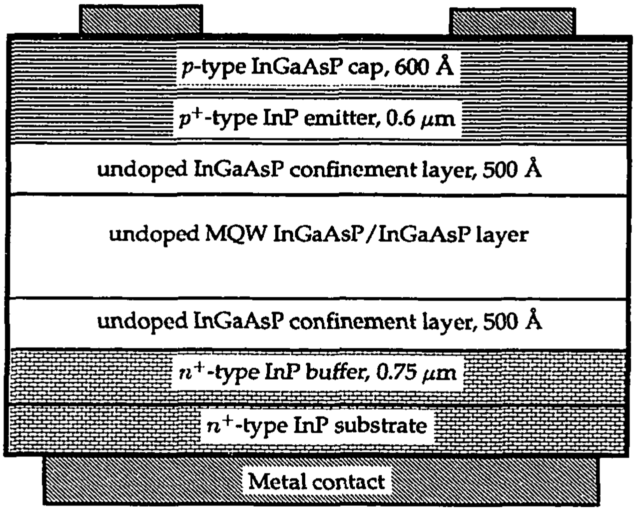

Figure 4.1: Layer diagram of the InGaAsP/InP MQW heterostructures (samples #381 and #382).

4.2 Samples

$In_xGa_{1-x}As_yP_{1-y}$ quaternary alloy is a material of choice for manufacturing semiconductor lasers emitting in the 1.3–1.7 μm, infrared detectors, light emitting diodes (LEDs) and high-speed heterojunction devices.

Two MQW samples with an identical well width and different barrier thickness (see Fig. 4.1) were grown on n^+-type InP substrates in a low pressure (60 Torr) metalorganic chemical vapor deposition (MOVPE) reactor [52]. The unintentionally doped (light p-type) active MQW region consisted of 9x70 Å compressively strained wells of InGaAsP (λ = 1.35 μm) and 8x80(8x150) Å lattice-matched barriers of InGaAsP (λ = 1.12 μm), samples #382 and #381, respectively.

The MQW region was confined by 500 Å undoped InGaAsP (λ = 1.12 μm) separate confinement layers and embedded between n- and p-InP ($1.5 \cdot 10^{18}$ cm^{-3}) cladding layers. To create an ohmic contact, the p-type top InP layer was covered with a 600 Å thick InGaAsP ($\lambda = 1.12$ μm). For current-voltage measurements contacts on both MQW samples were formed by evaporating gold at 10^{-6} Torr. Top contact was O-shaped (inner radius = 2 mm) to let the light penetrate inside the structure.

4.3 Experiment

An experimental setup used here was similar to the one described in Section 3.2. A mode-locked Nd^{3+}:YAG laser (82 MHz repetition rate, 8 W maximum output, $\lambda = 1064$ nm) with a second harmonic generation system (1.5 W maximum output, $\lambda = 532$ nm) was used as an excitation source in all PL measurements. The PL spectra were measured using lock-in technique. The current-voltage and spectral response were measured using Keithley 236 SMU with a combination of the quartz tungsten halogen lamp and 0.25 m SPEX spectrometer.

4.4 Results

4.4.1 Photoluminescence Measurements

Photoluminescence spectra for both InGaAsP MQW samples at 77 K and zero voltage bias are shown in Fig. 4.2. Peaks at 1.23-1.24 μm are assigned to the radiative recombination of photocarriers in the quantum wells (a transition between electron and heavy hole ground states). A peak at $\sim 1.07\mu$m (later referred as "barrier") is attributed to the cumulative emission from the InGaAsP cap, barriers and confinement layers. The relative strength of the QW PL peak is higher for the 150 Å sample than that for the 80 Å barrier sample. This observation is based on a stronger carrier confinement and lower escape rate for the first sample (150 Å). For both samples the observed full width at half maximum (FWHM) of the QW peaks is within 10-12 meV, which indicates good structural and optical quality of the quantum wells.

Temperature dependence of the PL spectra for the 150 Å sample at zero voltage bias is

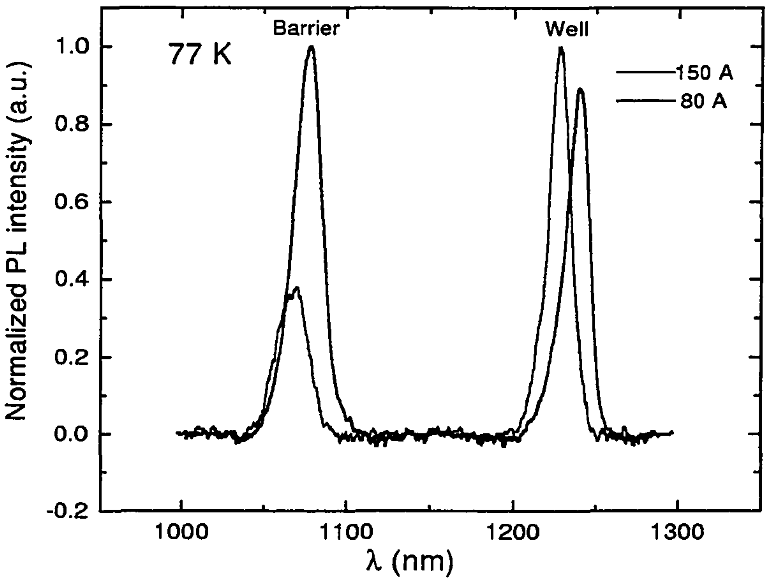

Figure 4.2: Photoluminescence spectra of the InGaAsP/InP MQW heterostructures at T = 77 K. Thick line – the 80 Å barrier sample; thin line – the 150 Å barrier sample

shown in Fig. 4.4. As the temperature increases, the following changes are observed in the PL spectra. First, the PL peak positions shift to the longer wavelength side, consistent with changes in the energy bandgap; second, the PL line intensities significantly decrease; and third, the PL peak widths broaden. Closer to room temperature, the thermal spreading of the carrier population contributes to an increased radiation from the excited QW states as well as to a general broadening of the PL lines.

Fig. 4.4 presents the temperature dependence of the QW PL peak position for both samples, where the symbols represent experimental data and the solid lines are the values of the energy bandgap for the corresponding bulk InGaAsP (with the same E_{gap}) alloy calculated using the phenomenological Varshni equation [53]

$$E_{gap}^{IGAP}(T) = E_{gap}^{IGAP} - \frac{\alpha T^2}{\beta + T} \tag{4.1}$$

where T is the temperature in K, $\alpha = 6.9 \times 10^{-4}$ eV/K^2 and $\beta = 327$ K. The experimental data show essentially the same temperature behavior as the bandgap of the bulk InGaAsP alloy, which allows us to conclude that the QW energy subbands remain unaffected by the temperature changes. This behavior is similar to the results reported for InGaAs/InP MQW structures [54].

The ratio of well-to-barrier PL peak intensities I_w/I_b shown in Fig. 4.5 provides information about interrelationship between carrier capture and escape times, τ_{cap} and τ_{esc}, respectively. This ratio can be written as a function of the $(n_w p_w)/(n_b p_b)$ [55]

$$\frac{I_w}{I_b} \propto \frac{n_w p_w}{n_b p_b} \propto \frac{\tau_{esc}^n \tau_{esc}^p}{\tau_{cap}^n \tau_{cap}^p} \tag{4.2}$$

where n_w, p_w, n_b and p_b are electron and hole densities in the quantum well and barrier, respectively, and n and p indices stand for electron and hole. Taking the ratio of the intensities instead of just I_w or I_b alone also reduces the effect of the temperature dependence of radiative recombination rate on the analysis as well as eliminates errors due to the pump

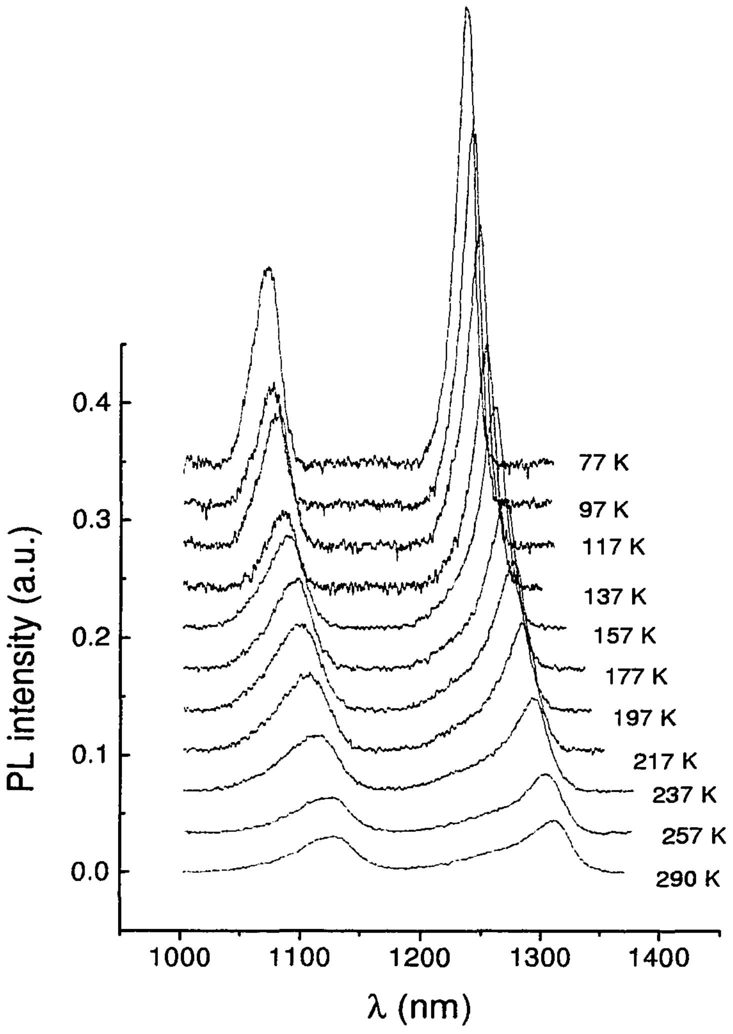

Figure 4.3: Evolution of the PL spectra with temperature (sample #381, InGaAsP/InP MQW heterostructure)

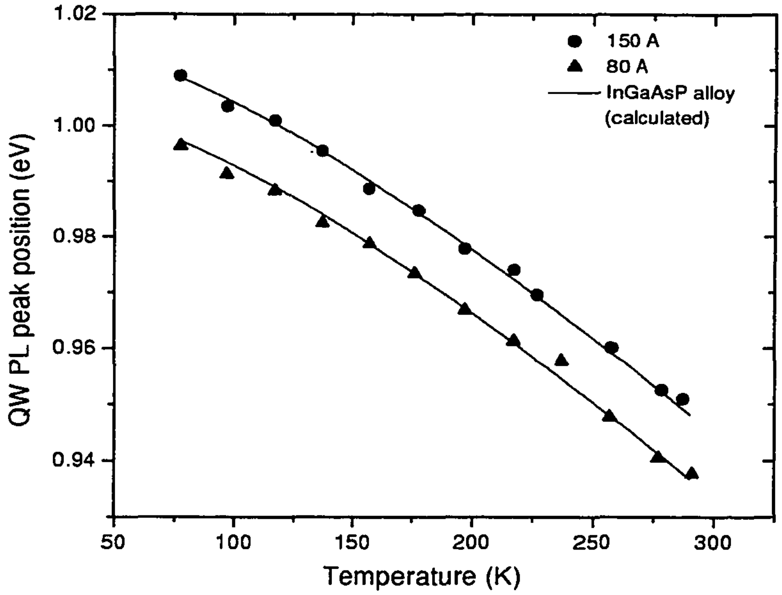

Figure 4.4: QW PL peak position versus temperature. Circles – the 80 Å barrier sample; triangles – the 150 Å barrier sample; solid lines – calculated values for the bandgap of InGaAsP bulk alloy.

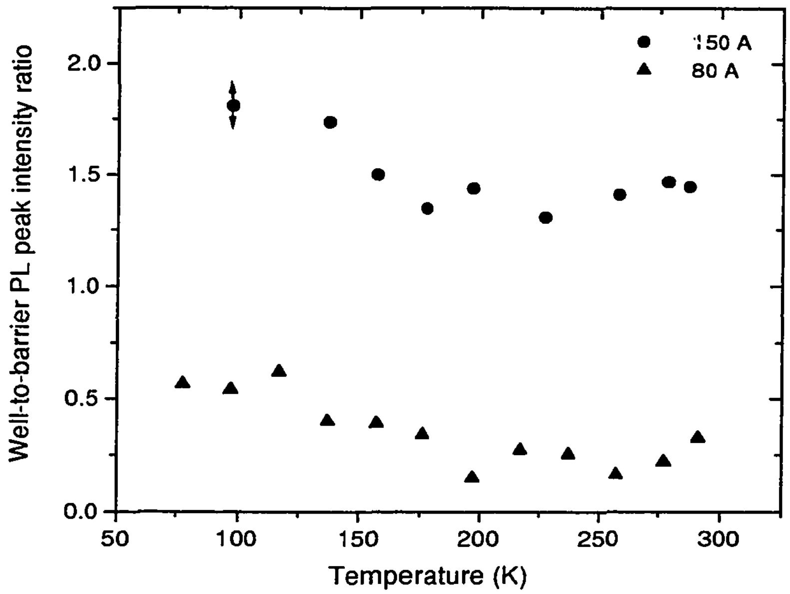

Figure 4.5: Plot of the ratio of the well-to-barrier PL intensities versus temperature. Circles – the 150 Å barrier sample; triangles – the 80 Å barrier sample.

power fluctuations. As it is seen in Fig. 4.5, this ratio predictably lowers with rising temperature as more and more carriers are thermally excited out of the quantum well, thus effectively decreasing $n_w p_w$ and I_w. This can be also interpreted as a reduction of the carrier escape time over capture time.

The voltage bias has a very pronounced effect on the PL spectra. Fig. 4.6 shows photoluminescence spectra of the 150 A MQW sample taken at zero bias (dotted line) and -1 V bias (solid line). The change in the bias significantly reduced the magnitude of the QW peak and had relatively no effect on the barrier peak. More detailed view of the bias effect is shown in Fig. 4.7 which shows a plot of the intensities of barrier and QW PL peaks versus bias. In a negative bias region, the separation of electron-hole pairs generated inside the undoped MQW region increases, such that the excited carriers can escape before they

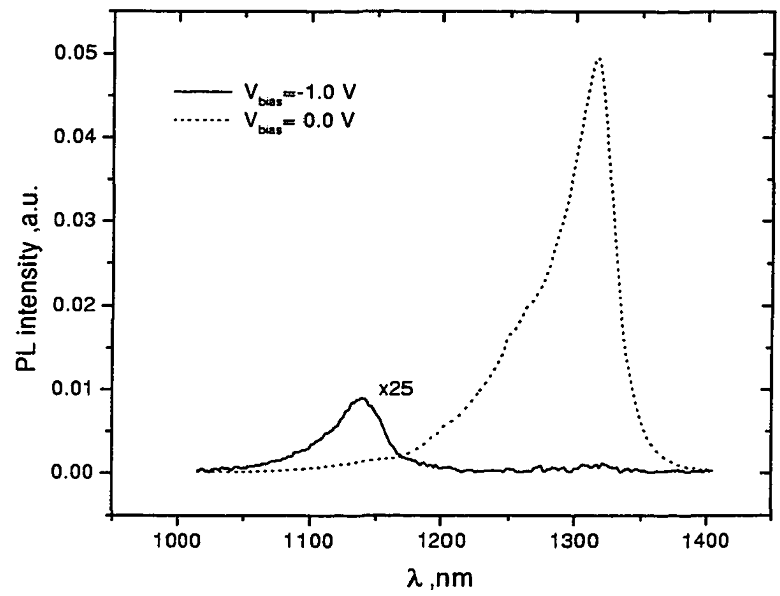

Figure 4.6: InGaAsP/InP MQW Photoluminescence at 0 V bias (dotted) and -1.0 V bias (solid, x25 magnified).

recombine in the quantum well. The high-doped layers remain relatively unaffected by the bias and should not exhibit any significant changes in the photoluminescence. From the Fig. 4.7 it can be seen that the QW emission is very sensitive to bias, whereas the barrier PL intensity is almost unaffected. This suggests that most of the barrier PL emission comes from the topmost InGaAsP cap and confinement layers rather than barriers.

For high excitation intensities the photogenerated carriers in the MQW region can effectively screen the built-in field and thus, cause changes in the measured spectra. To account for this effect, a series of PL spectra at different excitation intensity was measured. Over 2.5 decades of the excitation power (0.3-45 W/cm^2), no noticeable line shape or position changes were observed, indicating that the excited carrier densities were relatively low and did not affect the internal potential distribution.

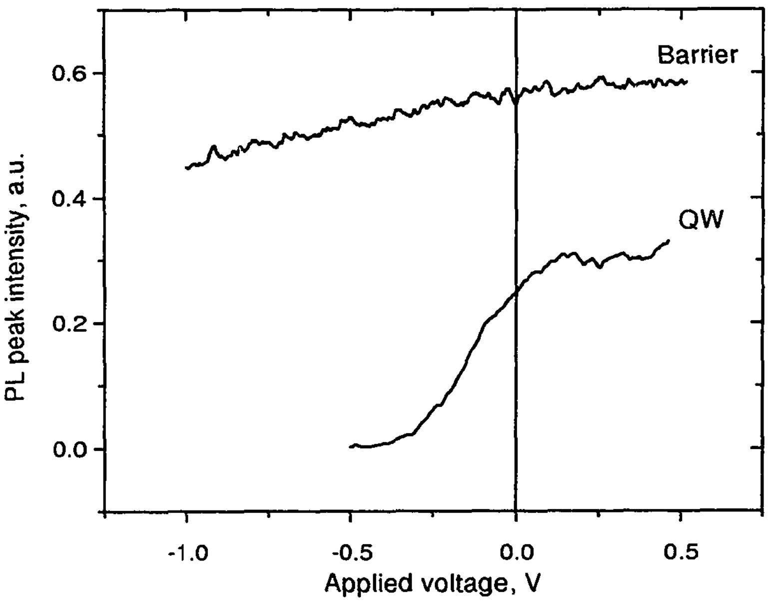

Figure 4.7: QW and barrier PL peak intensities versus applied voltage bias.

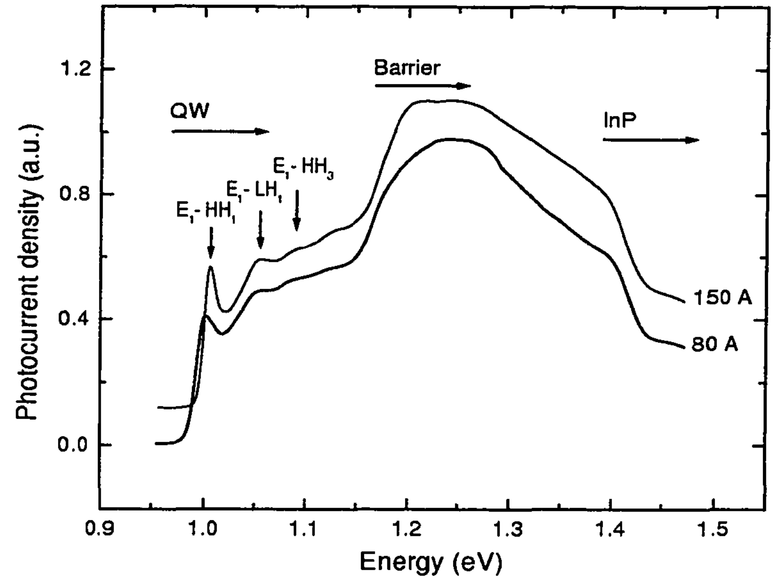

Figure 4.8: A plot of the photocurrent density versus excitation energy for InGaAsP MQW samples. The "80 Å" curve is shifted down for better view.

4.4.2 Photocurrent Measurements

The photocurrent density versus an irradiative wavelength $J_{ph}(\lambda)$ measured at 77 K and zero voltage bias is plotted in Fig. 4.8. The curves were normalized to the maximum, the "80 Å" curve is shifted down for better view. It can be seen that, compared to the InP part, the QW and barrier regions make a significantly more contribution to the total current, which has been observed throughout the entire investigated temperature range. The differences between the 150 Å and 80 Å samples are easily identifiable: the 150 Å sample produces sharper $E_1 \rightarrow HH_1$ and $E_1 \rightarrow LH_1$ QW peaks and more pronounced barrier line, which is consistent with thicker barriers in this sample.

Fig. 4.9 shows plots of normalized QW photocurrent density J_{ph}^{qw} versus temperature

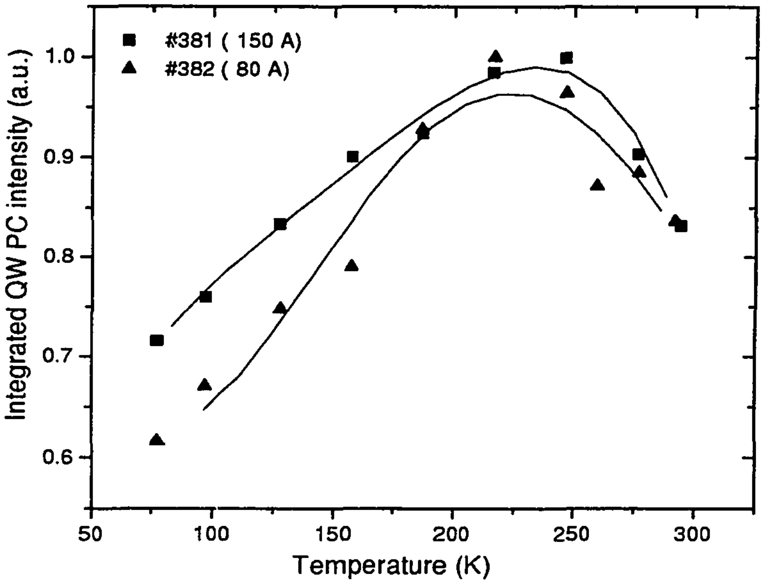

Figure 4.9: A plot of the normalized QW PC intensity versus temperature.

for both samples. The J_{qw} is an integral

$$J_{ph}^{qw}(T) = \int_{E_{gap}^{qw}}^{E_{gap}^{b}} J_{ph}(E,T)dE \tag{4.3}$$

where the integral limits are quantum well and barrier energy bandgaps, E_{gap}^{qw} and E_{gap}^{b}. Both curves shows similar behavior: an initial rise to a maximum near $\approx$ 220 K, and a decline towards room temperature. The rise portion can be attributed to the thermal activation of photoexcited carriers out of the well; the decline portion is most likely due to some thermally-activated non-radiative process.

4.4.3 Dark Current Measurements

Fig. 4.10 shows plots of the dark (unilluminated) current-voltage characteristics of both samples measured at room temperature. The differences between samples are most noticeable in the reverse bias portion of the I-V curves. For the given negative voltage, a larger dark current is observed for the sample with more narrow barriers.

In the forward bias domain, three components can be distinguished, denoted by I, II and III in Fig. 4.10, which are common to both samples. The relative strength of each component depends differently on the temperature as it is seen in Fig. 4.11, which shows the temperature evolution of dark I-V characteristic of the 80 Å sample. The second component (II) begins to appear for $T \geq 200$ K and completely vanishes below this temperature. Similar behavior was observed for the other sample. This fact is compared with the observed PC decrease for $T > 200$ K in Fig. 4.9, and, it is concluded that these trends in PC and dark current are related to each other and probably caused by the same thermally activated process. The value of the diode ideality factor for the second component is estimated to be ≈ 2, which indicates that this component is due to the contribution from the recombination-generation current.

4.5 Discussion

Effect of the Electric Field on Optical Properties

An important issue in the analysis of device properties is the adequate assessment of internal build-in field. Different thickness of the *i*-layer and background doping of the MQW region results in a variation of the built-in electric field, and thus the calculation of energy states and escape rates in a *p-i-n* structure requires some knowledge about the distribution of this field. Fig. 4.12 presents the calculated field distribution and conduction band profile in the MQW region of two samples using the method described by Lundstrom and Schuelke [44](see Sec.2.5). It can be seen that the difference in the barrier thickness has

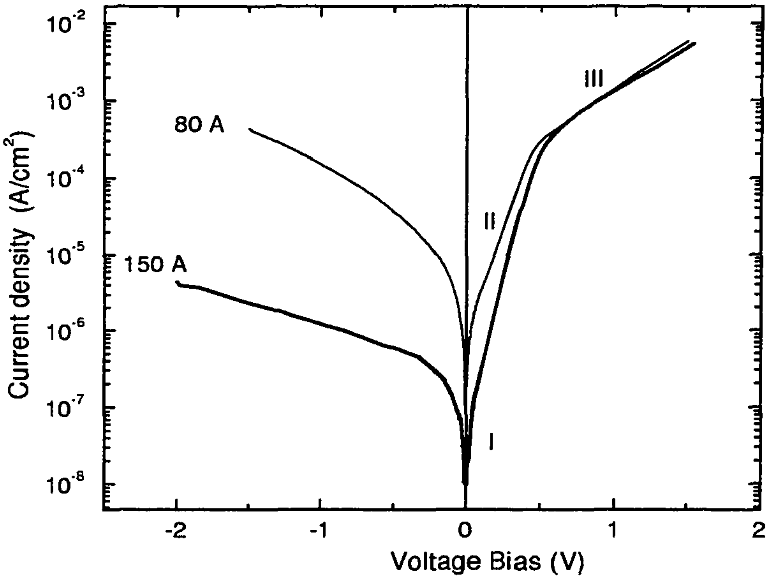

Figure 4.10: Dark current density for the InGaAsP MQW samples at room temperature. Thick line – the 150 Å barrier sample; thin line – the 80 Å barrier sample.

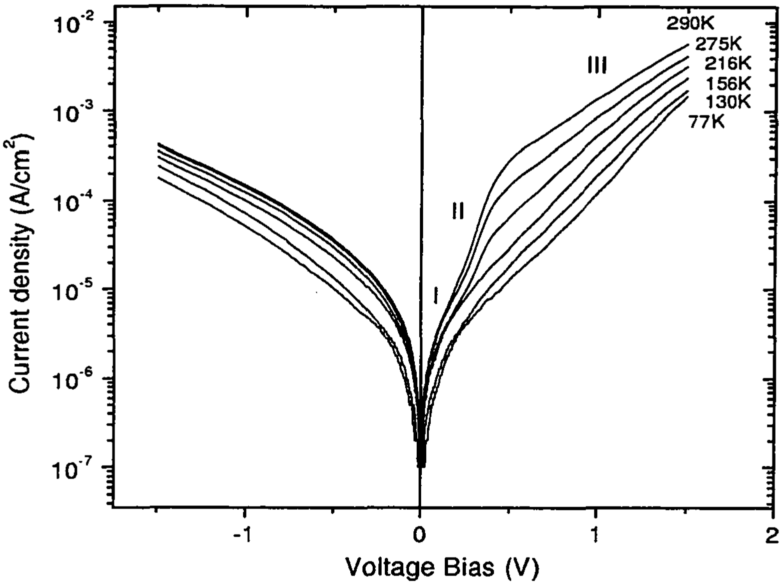

Figure 4.11: Temperature dependence of the dark current density for the InGaAsP MQW sample with a barrier thickness of 80 Å.

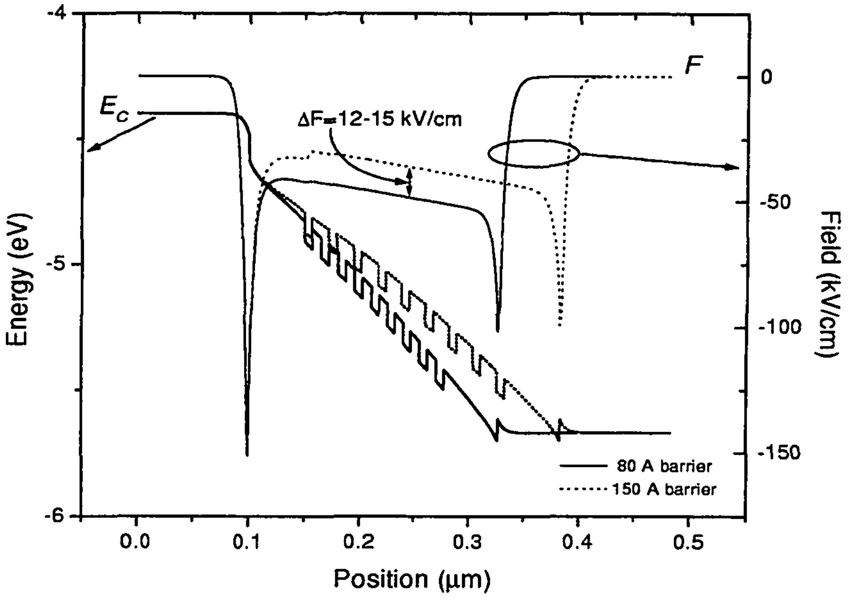

Figure 4.12: Calculated conduction band diagram and internal electric field distribution for InGaAsP/InP MQW samples. Dotted line – #381 sample (150 Å), solid line – #382 sample (80 Å). E_c is the conduction band edge, F is the internal field.

resulted in a difference of field magnitude: the average internal field for the sample #381 is ≈ 36 kV/cm, while for the sample #382 it is ≈ 46 kV/cm. Higher field in the latter sample has produced a stronger red shift for the $E_1 \rightarrow HH_1$ transition as it is seen in Fig. 4.8. The estimated red shifts due to the quantum confined Stark effect were 20 meV and 26 meV for #381 and #382 samples, respectively.

The effect of varying voltage bias on the total recombination rate is shown in Fig. 4.13.[1] Changing bias from 0 V to –0.5 V the recombination rate inside the MQW layer was reduced by a factor of 5, and at the same time the rate had remained unchanged inside *n,p*-InP layers. That is exactly the same behavior observed in Fig. 4.7, where QW PL intensity was decreasing with the bias, while "barrier" PL remained essentially unaffected.

---

[1] The data were calculated using David Winstone's **SimWindows32.**

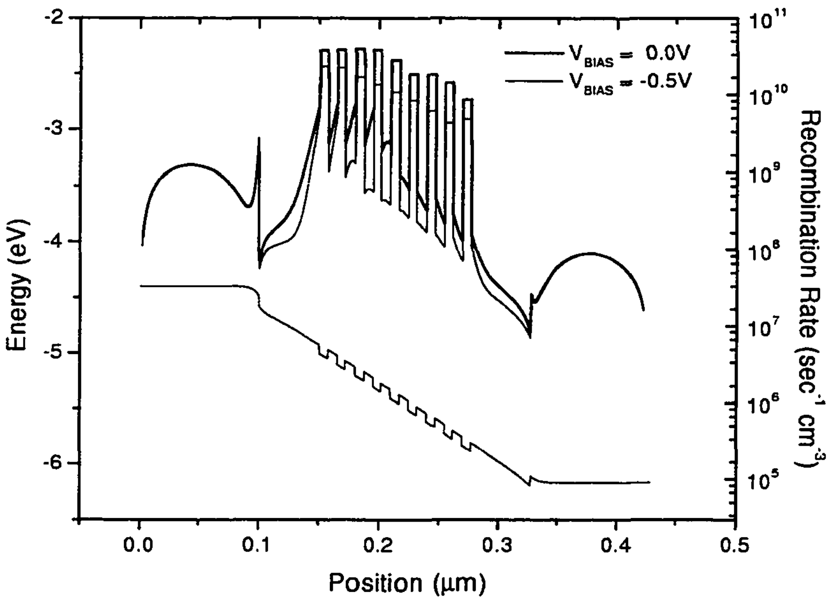

Figure 4.13: Calculated effect of the bias on the total recombination rate in the InGaAsP/InP MQW sample.

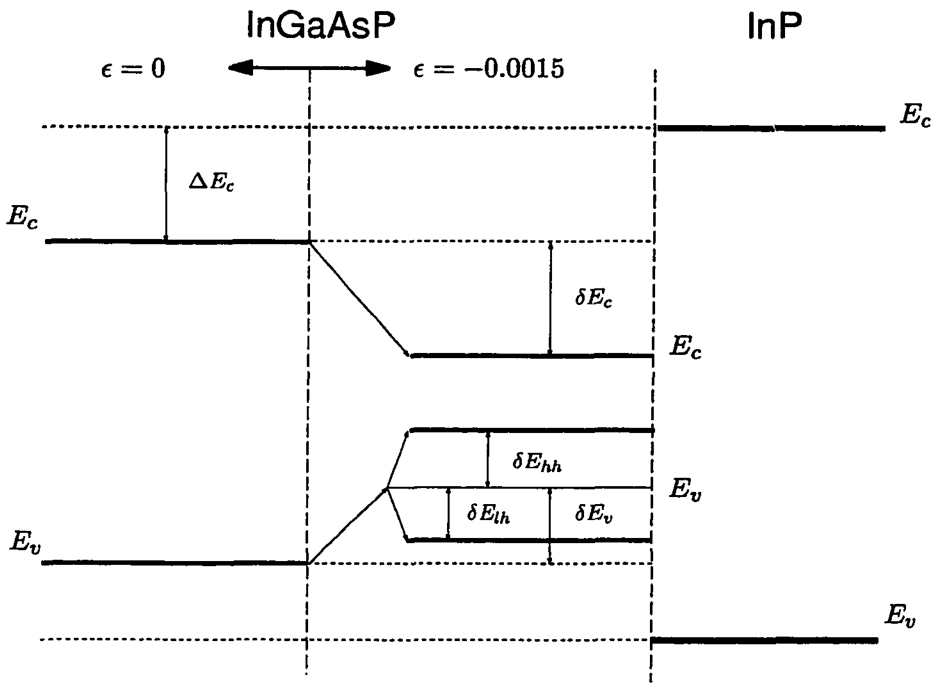

Figure 4.14: Effect of the strain on the band edges of InGaAsP. ΔE_c is the conduction band offset in unstrained InGaAsP, δE_c is the shift of the InGaAsP conduction band edge due to the strain, δE_{hh} and E_{lh} are the shifts of heavy and light hole valence band edges, respectively.

The Effect of the Strain on the Optical Properties

To calculate the effect of the strain on the band structure we have employed the approach described in Sec.2.2.4. For compressive strain of $\epsilon = -0.0015$ we have obtained the following figures: total bandgap reduction $\Delta E_{gap} = 0.020$ eV, shift of the conduction band edge $\delta E_c = -0.017$ eV, and shifts of the heavy hole band and light hole band edges $\delta E_{hh} = 0.010$ eV and $\delta E_{lh} = 0.010$ eV, respectively. Fig. 4.14 illustrates the strain effect on the band edges of the sample under investigation.

4.6 Calculations of the Energy States and Escape Rates

To calculate QW energy states we have used the transfer matrix technique described in Appendix A. In the transfer matrix calculations the inhomogeneous field inside the MQW region is replaced with some constant field obtained by averaging over the MQW region. The resulting error in energy subbands was estimated to be less than 5%. Using results of the previous section, the conduction, heavy hole and light hole valence band offsets were found to be 0.092, 0.123 and 0.097 eV, respectively. The next section describes in detail an interpolation procedure used to determine material parameters of InGaAsP alloys.

Material Parameters

The material parameters of the quaternary alloys, such as effective mass and bandgap, are a function of their composition (x and y parameters). Since it is cumbersome to measure the material parameters for every possible combination of x and y, the usual approach is to interpolate these parameters from the known constants of binaries and ternaries. We have used an interpolation scheme described by D. Gershoni, C. H. Henry and G. A. Baraff [56]. They have treated the InGaAsP alloy as if it were composed of the lattice-matched to InP ternary $In_{0.532}Ga_{0.468}As$ and InP, which properties have been well documented:

$$In_{1-x}Ga_xAs_yP_{1-y} = (In_{0.532}Ga_{0.468}As)_z(InP)_{1-z} \tag{4.4}$$

The single composition parameter z is used, since for a lattice-matched composition x and y are not independent and are related through $y = 2.137x$

Table. 4.1 lists the material parameters of several compound semiconductors used in our calculations.

Any material parameter for the quaternary A^{IGAP} alloy is linearly interpolated be-

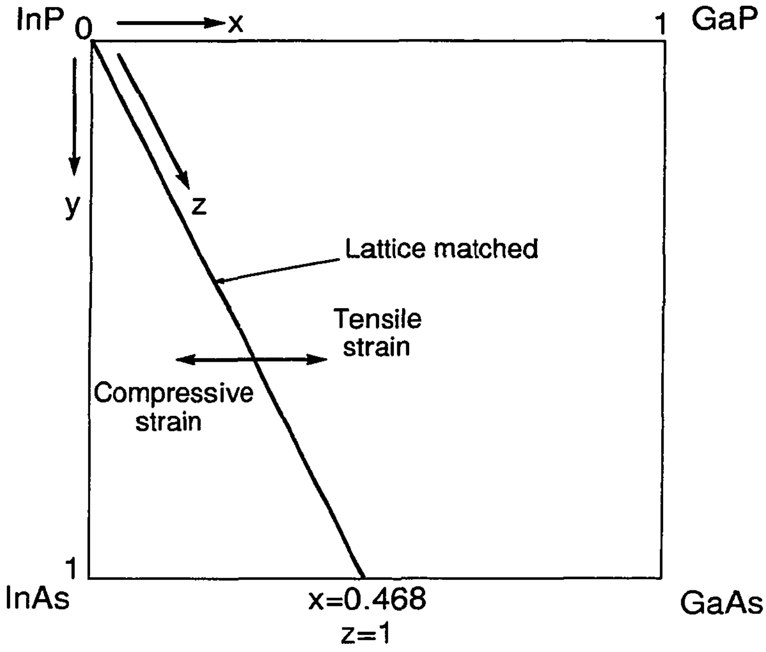

Figure 4.15: Diagram of the InGaAsP quaternary alloy showing lattice-matched composition and the composition of compressive and tensile strain [56].

Parameter	GaAs	GaP	InAs	InP	$In_{0.532}Ga_{0.486}As$
E_{gap}, eV	1.424	2.74	0.354	1.351	0.75
m_e^*	0.067	0.17	0.023	0.079	0.041
m_{hh}^*	0.62	0.79	0.60	0.85	0.46
m_{lh}^*	0.074	0.14	0.027	0.089	0.079
a, Å	5.6532	5.4512	6.0583	5.8587	5.8687

Table 4.1: Material parameters of GaAs, GaP, InAs, InP and $In_{0.532}Ga_{0.486}As$. m_e^*, m_{lh}^* and m_{hh}^* are effective masses (given in free electron mass m_0 units) for electrons, light holes and heavy holes, respectively.

Alloy	z	ΔE_c	ΔE_{hh}	ΔE_{lh}	m_e	m_{hh}	m_{lh}
InGaAsP (1.3 mm)	0.668	0.189	0.269	0.242	0.055	0.46	0.072
InGaAsP (1.1 mm)	0.353	0.0976	0.146	0.146	0.067	0.46	0.072

Table 4.2: InGaAsP alloy (1.3 μm – strained, 1.1 μm – unstrained)parameters used in calculations. z is the composition parameter, ΔE_c, ΔE_{hh} andΔE_{lh} are the conduction, heavy hole and light hole band offsets, respectively, m_e, m_{lh} and m_{hh} their corresponding effective masses.

tween at of InP A^{IP} and that of InGaAs A^{IGA}

$$A^{IGAP}(z) = (1 - z)A^{IP} + zA^{IGA} \tag{4.5}$$

For the quaternary bandgap, the interpolation is parabolic, to account for the bowing of the bandgap

$$E_{gap}^{IGAP} = (1 - z)E_{gap}^{IP} + zE_{gap}^{IGA} - z(1 - z)B \tag{4.6}$$

where $B = 0.012$ eV.

The procedure for determining of z_{barr} is very straightforward: the value of bandgap obtained from the PL or PC spectra is substituted in the LHS of Eq. 4.6 and the equation is solved for z. For z_{well} the procedure gives an effective z, because Eq. 4.6 doesn't take into account strain, quantum confinement and Stark effects. To get a correct value of z_{well} the following procedure was adopted: after finding first z_0, all these corrections are added to E_{gap}^{IGAP} and a new value of z_1 is calculated. z_1 is then used to calculate updated material parameters and band offsets. The procedure was repeated until required self consistency is achieved (usually 2-3 iterations is enough). Table 4.2 shows the results for z and other material parameters of both 1.1 μ and 1.3 μ InGaAsP alloys.

To calculate the carrier escape rates, the confined energy states for electrons and holes were first found using the same transfer matrix technique. In our calculations it is assumed

	#381		#382	
Transition	Experiment	Calculation	Experiment	Calculation
$EE_1 \rightarrow HH_1$	1.006	1.006	1.000	1.000
$EE_1 \rightarrow LH_1$	1.052	1.060	1.049	1.047
$EE_1 \rightarrow HH_3$	1.089	1.079	1.083	1.083

Table 4.3: Calculated and experimentally measured energies of the optical interband transitions in InGaAsP/InP MQW samples

that $\Delta E_v = 0.61\Delta E_{gap}$, where ΔEv is a valence band offset for InGaAsP/InP systems and ΔE_{gap} the total band gap discontinuity. The calculations showed that the effect of different barrier thickness on peak positions was considerably small (less than 1 meV shift) compared to the uncertainties in material parameters. Table 4.3 lists calculated and experimentally measured energies of the interband optical transitions. There is a good agreement between the experiment and calculations.

We assume that the photoexcited carriers successfully escaping from the quantum wells contribute to the QW part of the photocurrent. The photocurrent density J_{ph} can then be written as $J_{ph} \approx qn_{2D}\frac{1}{\tau_{esc}}$ [12], where q is the electron charge, n_{2D} is the 2D density of the photogenerated carriers and $\frac{1}{\tau_{esc}}$ is the escape rate. The n_{2D} is assumed to be a relatively weak function of the temperature and electric field. It is clear that, for given excitation intensity, to increase the output current one should increase carrier escape rate.

The calculated temperature dependence of the carrier escape rate $1/\tau_{tot}(T)$ has been compared with the measured QW photocurrent density $J_{ph}(T)$ in Fig. 4.16. It is found that the change of the measured photocurrent with temperature mostly follows the changes of the electron escape rate. This is expected, since in InGaAsP/InP QWs, electrons are the carriers with the lowest escape time. The activation energy obtained from single exponential fitting to the $J_{ph} \propto f(1/T)$ plot gives a value of 33±2 meV for the effective barrier height, which tends to be somewhat more than our calculated value of 25 meV. Since the effective barrier height is directly proportional to the electric field, this discrepancy may be a result of the averaging procedure we attempted earlier. In order to explain the reduction of $J_{ph}(T)$ for $T > 200$ K, our model should be considerably expanded and take into account various non-radiative recombination processes, which is out of scope of this work. As mentioned earlier, this reduction of $J_{ph}(T)$ may occur when the photogenerated carriers get trapped or recombine on impurity levels located inside the energy band gap, which effectively diminishes or eliminates their contribution to the total PC.

From this investigation of InGaAsP/InP based MQW heterostructures, information was learned which can be important for designing efficient MQW devices, such as photodiodes and solar cells. This study showed that lowering temperature below 200 K had an overall degrading effect on the photocurrent in InGaAsP/InP based MQW; however, in the range of 200-250 K small rise of PC magnitude was observed which was attributed to the reduction of losses due to the carrier recombination on impurity levels. The difference in barrier thickness – 80 Å versus 150 Å – has the most profound effect on amplitude of PL and PC. The sample with 150 Å barriers had ≈1.8 more intense QW PL and twice as less PC compared to the 80 Åbarrier sample under the same experimental conditions. Because barrier thickness mostly affects tunneling, this means that tunneling through the barriers is a crucial element in carrier escape for this particular range of thickness 80–150 Å. The electrons appeared to play a more significant role in defining the photoconductive properties in these InGaAsP/InP heterostructures than their hole counterpart, as it was discussed above for the case of escape rates. The transfer matrix method and interpolation scheme used to calculate energy subbands in the InGaAsP QW show good agreement with the experiment.

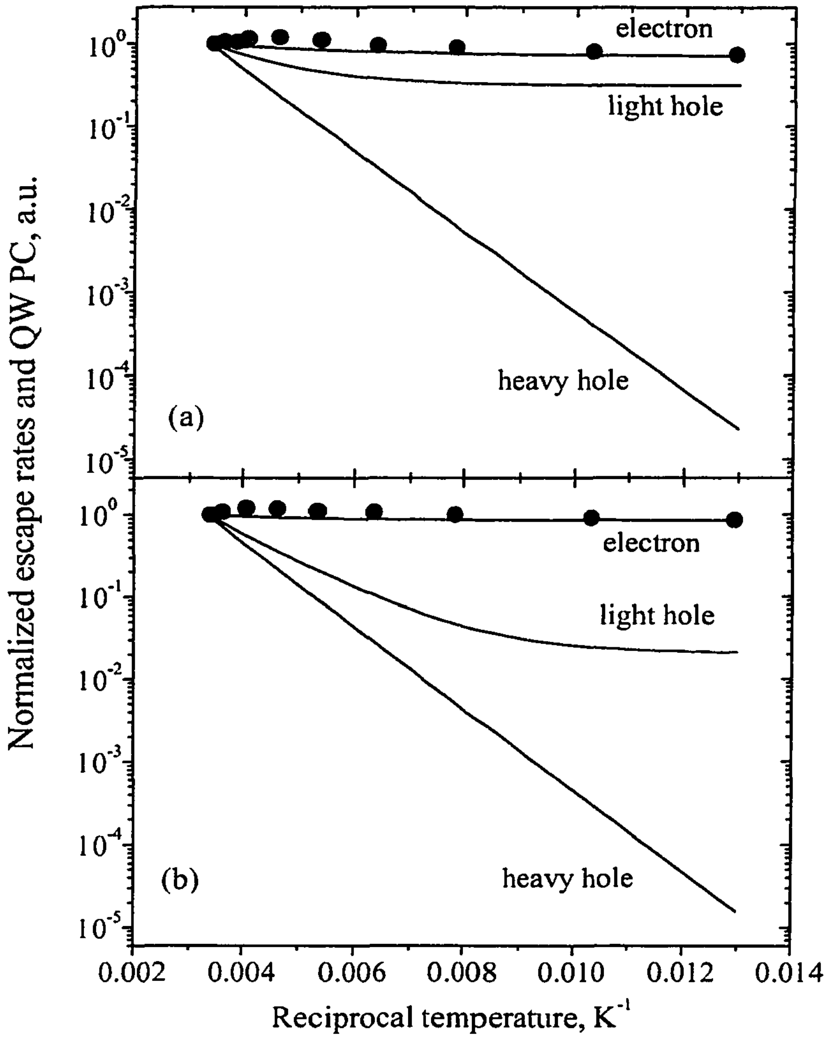

Figure 4.16: Calculated escape rates $1/\tau$ (solid lines) and experimental photocurrent (circles). All curves were normalized to their respective values at room temperature. (a) sample 381 (150 Å barrier), (b) sample 382 (80 Å barrier).

4.7 Conclusion

In conclusion, MQW InGaAsP/InP *p-i-n* heterostructures with different barrier thickness have been investigated by measuring PL, PC and DC. The observed PL and spectral line positions were found to be in good agreement with those obtained from transfer matrix calculations. Comparing the measured QW PC with calculated carrier escape rates, the photocurrent changes were found to be governed by the temperature dependence of the electron escape time. An activation energy obtained from the PC data seems to support this conclusion.

Chapter 5

Investigation of the $\mathrm{In}_x\mathrm{Ga}_{1-x}\mathrm{As}_y\mathrm{P}_{1-y}$ MQW Solar Cell Structures

5.1 Introduction

This chapter's focus is on InGaAsP/InP MQW-based solar cells. We describe our measurements of the photovoltaic efficiency of the InGaAsP/InP (well – InGaAsP, barrier – InP) MQW device structures and compare its efficiency with that of the InP-based control samples as shown in Fig. 5.1.

The MQW cell was designed to facilitate transport and increase collection rates of the photogenerated carriers in the MQW region, in which the well and barrier widths were chosen to permit a *sequential resonant tunneling* (see Chapter 2.2.8) between adjacent wells [15]. An increase of 13% in efficiency for the MQW device was observed over the control sample [57]. Photocurrent and photoluminescence spectra measured at the different bias and excitation wavelengths were used to investigate carrier escape and recombination processes.

The prospect of using multiple quantum well (MQW) structures in solar cells has been a subject of active research interest. It has been shown that MQW solar cells can improve

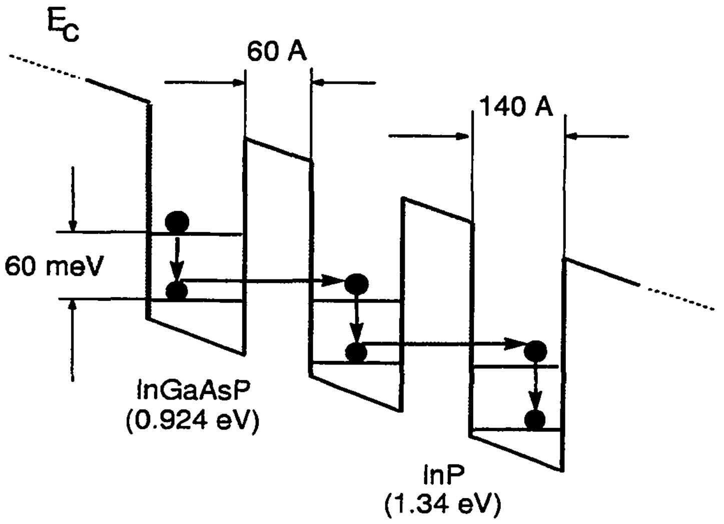

Figure 5.1: Conduction band edge diagram of the $In_{1-x}Ga_xAs_{1-y}P_y$/InP MQW solar cell sample. Shown is a part of the MQW layer.

the photovoltaic efficiency over comparable non-MQW cells by a factor of two [41]. The main effect of the inclusion of quantum wells (QWs) into the structure is the extension of the solar cell absorption spectrum, which results in a higher short circuit current (I_{sc}). When there is no significant reduction in the open circuit voltage (V_{oc}), the net result is an enhancement of the photovoltaic conversion efficiency (η).

An efficiency increase was reported for AlGaAs/GaAs-based cells [7]. InP-based solar cells have a potential advantage over GaAs and Si-based cells, due to its possible higher efficiency and proven higher radiation resistance [58]. The latter is mostly important for extraterrestrial space applications. Several groups have investigated MQW solar cells based on the InGaAs/InP system [8,9,59]. Anderson and Wojtczuk [9] reported a *drop* in the efficiency compared to the control InP samples, which was attributed to the large well/barrier bandgap differences and a possible unintentional increase in the background doping. It has been pointed out by Anderson [9] that high recombination rates in the MQW cells (compared to the non-MQW devices) may preclude possible efficiency enhancements. For the InP-based QW solar cell it has been suggested to use shallow-well systems, which implies that the $In_{0.53}Ga_{0.47}As/InP$ combination is not a very good choice for the efficient InP-based MQW solar cell. In more recent work on this combination Zachariou and coworkers [59] found an increase of the efficiency for samples with an unconventional diffusion doping of the top InP layer.

An efficient escape and transport of the photoexcited carriers across the MQW region determine the performance of the QW solar cell. The carrier escape mechanisms fall into several categories: thermionic emission of carriers above the barrier, tunneling out of the well, absorption of optical phonons, and the combination of the last two (thermally assisted tunneling) [14]. These processes are competing against radiative and non-radiative recombination, which tends to diminish the photocurrent.

To enhance the carrier collection rate and reduce recombination losses one can implement *resonant tunneling* transfer inside the MQW structure. In resonantly coupled wells, the electron transfer time between adjacent wells is reduced by several orders of magnitude compared with a non-resonant transfer, which can produce a large amplification of the photocurrent [15].

In 1990, Barnham and Duggan (B&D) [6] suggested resonant tunneling for efficient carrier collection in MQW solar cells as shown in Fig. 1.2a. Resonantly enhanced photocurrent in the MQW structures was observed by several groups [16,17] in GaAs/AlAs MQW samples. However, the number of QWs, which can be simultaneously aligned in a resonance with each other, is limited to 5-6. That corresponds to the $\sim$0.1 μm thickness of the intrinsic layer and it is not acceptable for photovoltaic devices due to the low absorption. To compensate for low absorption B&D suggested to add several *not-in-resonance* wells to the end of the MQW stack. However, in our opinion, it defeats the whole purpose of having resonant tunneling transfer in the first place. After passing through the first "resonant" region, carriers will tend to accumulate in the region with slow transfer capabilities. One would overcome insufficient thickness by putting together several lattice-matched materials, e.g., II–VI and III–V group semiconductors. However at the current state of semiconductor growth, it is difficult to combine more than three lattice-matched materials. To overcome this deficiency we have proposed an MQW solar cell with sequential resonant tunneling.

The choice of well/barrier combination can be a significant factor. In 1994, Mohaidat *et al.* [11] theoretically investigated the dependence of the MQW solar cell efficiency operated under resonant tunneling condition on the barrier potential V_b. Based on the calculation of the time-dependent short-circuit current density at the collector side of an MQW solar-cell structure using the time-dependent Schroedinger equation and the relation between the output voltage at maximum power and the barrier potential, the role of electron resonant tunneling and barrier potential in the solar-cell efficiency was determined. It was shown that for solar-cell MQW structures made with a small quantum-well band gap, such as that of InAs in InAs/$\mathrm{In}_{1-y}\mathrm{Ga}_y\mathrm{As}$ structures, the efficiency will peak at a specific value of y or equivalently at a specific barrier potential. Fig. 5.2 shows the results of these calculations. This barrier potential value for InAs/$\mathrm{In}_{1-y}\mathrm{Ga}_y\mathrm{As}$ MQWs was found to be about 450 meV. For structures with large quantum-well band gap, such as that of GaAs in GaAs/$\mathrm{A1}_x\mathrm{Ga}_{1-x}\mathrm{As}$, the efficiency declines linearly as the value of x or the barrier potential is increased.

Incorporating resonant tunneling in the MQW structure imposes many limitations on what well and barrier widths, and band offsets that can be used. Using ternary lattice-matched InGaP and InGaAs alloys only, one can change the band offset by varying well widths, which is not always acceptable, because it changes the thickness of the *i*-layer, and, consequently, the built-in electric field. $\mathrm{In}_{1-x}\mathrm{Ga}_x\mathrm{As}_{1-y}\mathrm{P}_y$ quaternary alloy used in our MQW sample appears to be a better choice, as it permits us to choose the appropriate bandgap value and maintain the lattice matching condition at the same time by varying its stoichiometry.

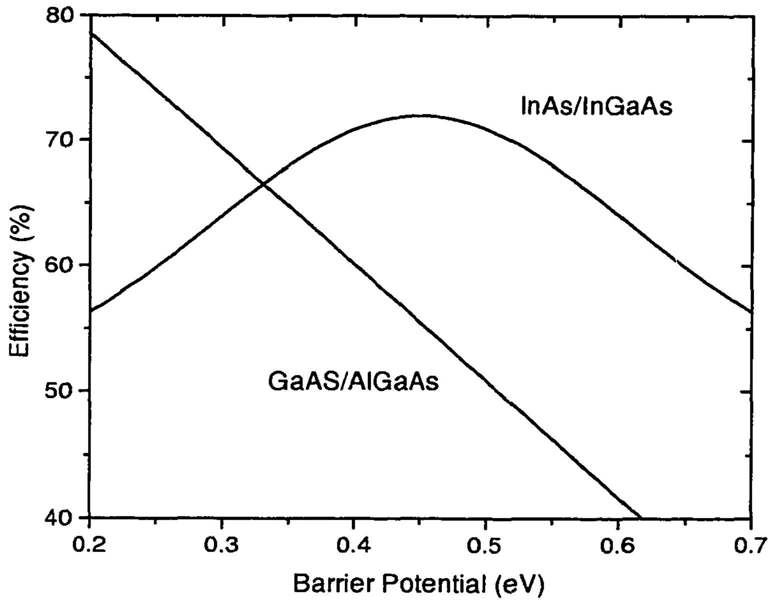

Figure 5.2: The photovoltaic energy conversion efficiency of InAs/$In_{1-y}Ga_yAs$ and GaAs/$Al_xGa_{1-x}As$ MQW solar cell (from [11]).

5.2 Theoretical Background

Efficiency of an Ideal Quantum Well Solar Cell

In order to better understand advantages and disadvantages of quantum well solar cells (QWSC) we have modeled the photovoltaic characteristics of an ideal InP-based QWSC. This was done in the framework of Anderson's work described earlier (see Sec.2.4.3). The key parameter of the model is the difference between bandgaps of the base (barrier) and quantum well materials $\Delta E_{gap} = E_{gap}^{base} - E_{gap}^{qw}$.

We have assumed that incident radiation is that of an ideal black body at T=5800 K. The number of photons emitted per unit area and unit time N_{ph} is

$$N_{ph}(E,T) = 2\pi \frac{E^2}{c^2 h^3 (e^{\frac{E}{k_B T}} - 1)} \tag{5.1}$$

The total incident power P_{inc} is

$$P_{inc} = \int_0^\infty N_{ph}(E,T) E dE = \frac{2\pi}{c^2 h^3} \int_0^\infty \frac{E^3 dE}{e^{\frac{E}{k_B T}} - 1} = 140\, mW/cm^2 \tag{5.2}$$

which is close to air-mass zero (AM0) conditions (135 mW/cm$_2$).

The following parameters were calculated: $\eta^{qw} = \frac{P_{max}^{qw}}{P_{inc}}$ – the photovoltaic efficiency of the ideal QWSC, where $P_{max} = (I(V)V)_{max}$; $\eta_R = \eta^{qw} - \eta^{base} = \frac{P_{max}^{qw} - P_{max}^{base}}{P_{inc}}$ – the relative increase in the QWSC efficiency over the base (control) solar cell, and V_{oc}^{qw} and I_{sc}^{qw} – the open-circuit voltage and short-circuit current, respectively. In these calculations we have used the following parameters: $T = 300$ K, $E_{gap}^{base} = 1.34$ eV, radiative recombination coefficient $B_{rec} = 5 \cdot 10^{10}\ cm^3/s$, doping density $N_{dop} = 1 \cdot 10^{18}\ cm^{-3}$, carrier mobility $\mu = 1000\ cm^2/V\ s$, intrinsic layer width $W_i = 0.5\ \mu$, ratio of well-to-barrier material inside the intrinsic layer $f_W = 2/1$, "density-of-states" enhancement factor $\gamma_{DOS} = g_W/g_B = 0.5$, where g_W and g_B are the effective volume densities of states for the wells and barriers, and "oscillator" enhancement factor $\gamma_B = 1$, the ratio of recombination coefficients B_W/B_B in the well and barrier.

Fig. 5.3 presents the calculated results for η(a), I_{SC}(b) and V_{OC}(c). The following trends are easily identified:

- V_{oc} exponentially decreases with ΔE ($\propto -\frac{\Delta E}{k_BT}$)
- I_{sc} rises almost linearly following the downshift of the QW absorption edge.
- $\eta(\Delta E)$ shows a very well defined maximum at ≈ 0.3 eV.

The maximum relative increase of η achieved with these parameters is about 4-5%. The increase is purely due to expanding of the absorption band. The gain in the efficiency is certainly too small to justify the expenses of making MQW solar cells.

The questions are

1. Can we improve the relative efficiency increase over 4-5%?
2. What parameters can we adjust to achieve the desirable effect?

It is obvious that if we can find a way to slow down the rapid decrease of $V_{oc}(\Delta E)$ we would get much better efficiency. In Anderson's model the parameter which affects V_{oc} most is the exponential term in the "radiative enhancement ratio" r_R

$$r_R = 1 + f_W[\gamma_B \gamma_{DOS}^2 e^{\Delta E/k_BT} - 1] \tag{5.3}$$

(Eq. 2.112). By changing the magnitude of this term we can effectively control radiative recombination losses. We will keep all parameters in this equation fixed except for γ_B, radiative enhancement ratio. The curves in Fig. 5.4 shows the effect of varying γ_B on the relative efficiency increase. Clearly the effect is very significant. Besides the increase in the amplitude of the maximum, we can observe a shift of the maximum position towards a deeper well combination. The $\gamma_B = 0$ curve is a highly unrealistic case when V_{oc} does not depend on ΔE at all.

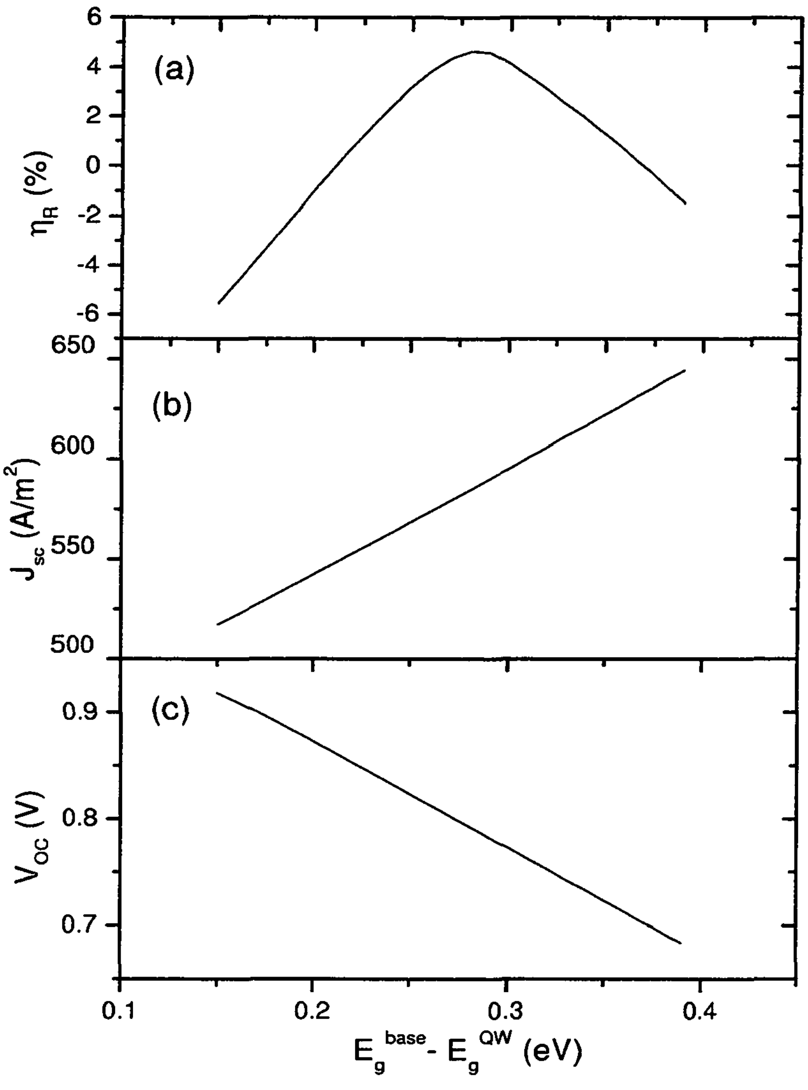

Figure 5.3: Calculated photovoltaic parameters of the ideal InP-based quantum well solar cell plotted vs QW-base bandgap difference: (a) – η the photovoltaic conversion efficiency, (b) – J_{sc} short-circuit current density, (c) – V_{oc} open circuit voltage.

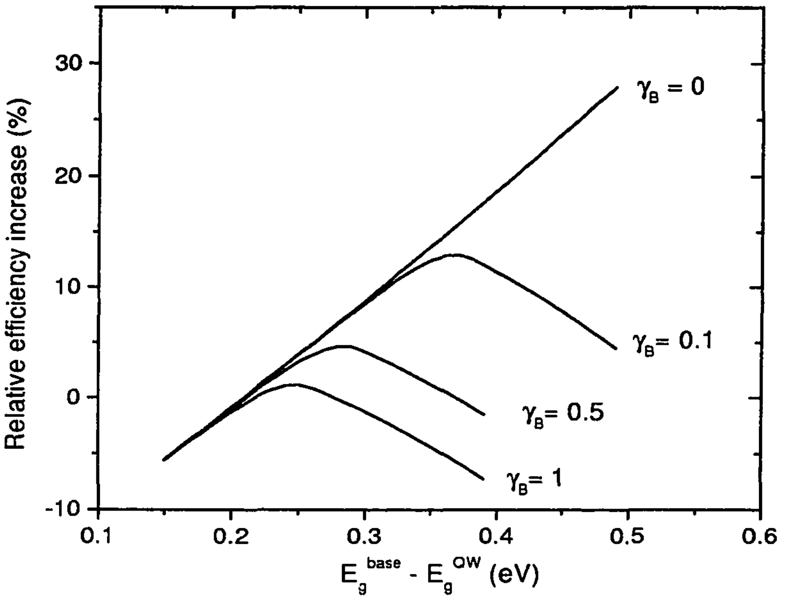

Figure 5.4: Calculated relative increase in photovoltaic efficiency $\eta^R = \eta^{QW} - \eta^{base}$ vs QW-base bandgap difference for different values of γ_B.

These results mean that in the framework of this idealistic model a reduction of the radiative recombination rate can significantly improve characteristics of the MQW solar cell.

Having identified these trends we have to find a way to change the radiative recombination rate in real devices. One way is to increase carrier escape/collection rates over the recombination rate. The next section describes how it can be done using accelerated collection rate via resonant tunneling transfer.

Resonant Tunneling Transfer

Under a steady-state situation, the carrier generation rate G inside a quantum well is balanced by the three possible carrier escape/recombination channels:

$$G = \nu_{esc} + \nu_{rad} + \nu_{nonrad} \tag{5.4}$$

where ν_{esc}, ν_{rad} and ν_{nonrad} are carrier escape, radiative and non-radiative recombination rates, respectively. The photocurrent and photoluminescence intensities, to a reasonable degree of accuracy, can be regarded as a measure of carrier escape and radiative recombination efficiency, respectively. Given that the non-radiative rate remains unchanged, for any increase in PL intensity one should expect to find a corresponding decrease in the PC magnitude and vice versa.

To achieve better performance, all recombination losses in solar cell should be minimized. Solar cells operate under the condition that there is an internal electric field, which separates carriers and produces the photocurrent. To generate power, solar cells should be operated in a forward bias range. This may result in a reduction of this field, and, consequently, of the photocurrent, compared to a zero or negative bias situation.

In the MQW devices, unlike the single quantum well, carriers, once escaped from the quantum well, can be recaptured again in the neighboring wells, which may have a negative effect on the carrier collection efficiency. The effects of the field reduction and transfer losses can be partially compensated by aligning wells in a resonance, as proposed by Barnham and Duggan [6] (Fig. 5.5a). Resonantly enhanced photocurrent in the MQW structures was observed by several groups [16,17] in GaAs/AlAs MQW samples. Increase in the collection rate is effectively equivalent to the reduction of the total recombination rate. In terms of the MQW solar cell model described earlier it means a decrease in γ_B. The number of QWs, which can be aligned in resonance with each other, is limited to 5-6. This corresponds to $\sim$0.1 μm thickness of the intrinsic layer and it is not enough for sufficient absorption.

Sequential resonant alignment appears to be free of thickness limitations (see Fig. 5.5b). Sequential resonant tunneling happens if the following condition is satisfied: $E_{e2} - E_{e1} = |q\vec{F}d|$, where $E_{e1,e2}$ are the ground and first excited subband energy of the quantum well,

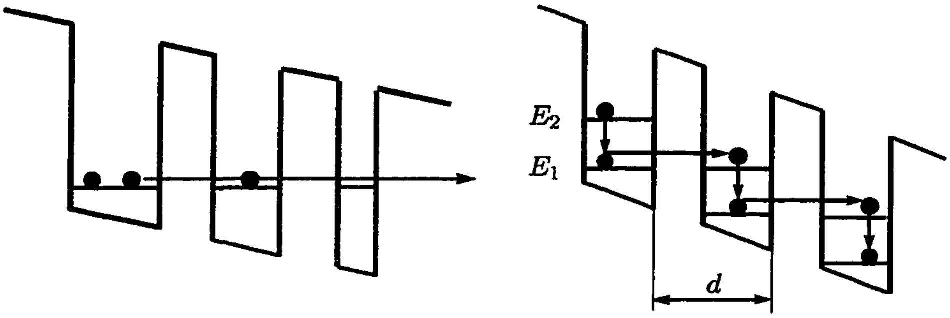

(a) Non–sequential tunneling (b) Sequential tunneling

Figure 5.5: Multiple quantum well structures with the resonant tunneling alignment: (a) – non-sequential, (b) – sequential

q – the electron charge, $\vec{F}$ – the internal electric field, and d – the MQW spatial period. It is assumed that $|\vec{F}| = (V_{app} - V_{bi})/L$, where V_{app} is the applied voltage, V_{bi} is the built-in voltage and L is the total thickness of the undoped layer. The field value used by us for calculating "resonant" barrier and well widths was chosen to be $|\vec{F}| = 0.8V_{bi}/L$. This result corresponds to a situation when a InGaAsP/InP solar cell operates approximately at a maximum power point under AM1.5 conditions [9].

5.3 Samples

Two samples were used in our experiments: one with the InGaAsP/InP MQW structure embedded inside an undoped i-layer of n-i-p diode and the other, the control InP sample, without MQWs. The layer diagrams of both samples are shown in Fig. 5.6. Both samples were grown by low-pressure metal organic chemical vapor deposition (MOVPE) on p-type (100) InP substrates. The MQW structure (Fig. 5.6a) contains 16 periods of 140 Å InGaAsP wells ($E_{gap} = 0.95$ eV), separated by 60 Å InP barriers with a total thickness of 0.31 μm. The MQW region is confined by undoped InP 500 Å buffer layers to prevent unwanted Zn diffusion [60] and to preserve uniformity of the internal electric field. The total thickness of the undoped layer was 0.41 μ. The emitter was formed from 0.25 μm thick n-type InP layer, which also served as the contact layer.

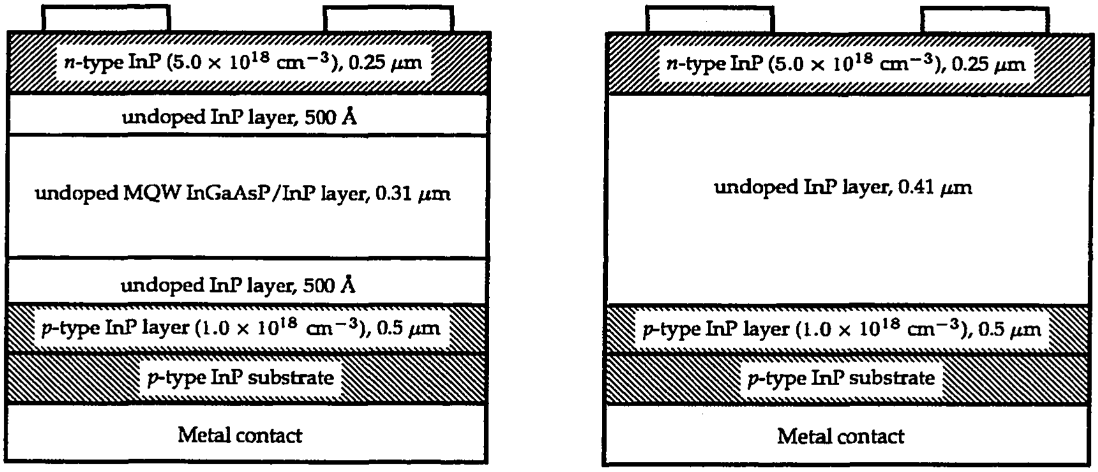

(a) InGaAsP/InP sample (b) InP sample

Figure 5.6: Layer diagrams of (a) the $In_{1-x}Ga_xAs_{1-y}P_y$/InP MQW and (b) InP control solar cell samples.

The control InP bulk sample (Fig. 5.6b) has a similar structure with 0.41 μm thickness of i-layer. The wafers were metallized to form a contact grid with a ≈ 10 × 4.5 mm cell size with ≈5 % shaded area. Each wafer was cut into several cells of different sizes (multiples of the grid cell), and each cell was wired and investigated.

5.4 The Top Grid Contact

The design of the top grid contact is an important area of any solar cell device. The contact shape has to be optimized to provide: (1) minimal shading of the top cell surface and (2) minimal losses due to contact resistivity. The following section describes the procedure used for designing an optimal grid [31]. A schematic diagram showing the rectangular metal grid adopted for our samples is shown in Fig. 5.7. It is made of relatively wide sparsely placed *busbars* and narrow frequently drawn *fingers*. The size of the grid cell is

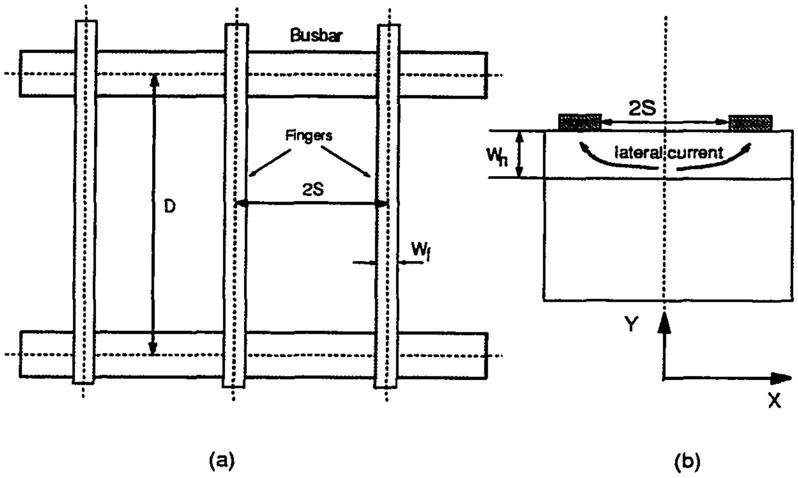

Figure 5.7: Design of the top grid contact for InGaAsP MQW solar cells: (a) top view of rectangular grid, $2S$ is the distance between the fingers, D is the distance between the busbars, and W_f is the finger width; (b) side view of the cell with the current flow.

$2S \times D$. Ignoring the resistivity losses in busbars, the total relative power loss (normalized to the power at the maximum point $P_{max} = SDJ_{max}V_{max}$) in a single grid cell consists of the resistive power losses in the fingers p_f and the emitter (top n-type InP layer) region p_s, the contact resistance loss p_c, and the loss due to shadowing of the fingers p_{sh}.

The power loss in the metal fingers:

$$p_f = \frac{I_{max}^2 R_f}{SDJ_{max}V_{max}} = \frac{J_{max}^2 S^2 D^2 R_f}{SDJ_{max}V_{max}} = \frac{\rho_f D^2 S J_{max}}{W_f V_{max}} \tag{5.5}$$

where $R_f = \rho_f D / W_f$ is the finger resistance. The loss due to the contact resistance ρ_c is given by

$$p_c = \frac{\rho_C S J_{max}}{W_f V_{max}} \tag{5.6}$$

and the resistivity loss due the lateral flow of the current in the emitter is

$$p_s = \frac{\int_0^S I^2 dR}{SDJ_{max}V_{max}} = \frac{J_{max}^2 D \rho_s \int_0^S x^2 dx}{SDJ_{max}V_{max}} = \frac{\rho_s S^2 J_{max}}{3V_{max}} \tag{5.7}$$

where $I = JDx$ is the lateral current, $R = \rho_s x/D$ the lateral sheet resistance and $\rho_s = (q\mu_n N_D W_n)^{-1}$ is the sheet resistivity of the top n-type layer, W_n its thickness. The shadowing losses are

$$p_{sh} = W_f/S \tag{5.8}$$

The total loss $p = p_c + p_{sh} + p_f + p_s$ in a single $S \times D$ cell can be minimized with respect to the finger distance $2S$. Neglecting busbar and contact resistivities, the minimum power loss is

$$p_{min} = \sqrt[3]{\frac{9\rho_S J_{max} W_f^2}{4V_{max}}} \tag{5.9}$$

which occurs for

$$S = \sqrt[3]{\frac{2V_{max} W_f}{2J_{max}\rho_s}} \tag{5.10}$$

The optimal value of S was calculated to be 2.5 mm. In these calculations $\mu = 800\ cm^2/(Vs)$, $N_d = 5 \times 10^{-18}\ cm^{-3}$, $W_f = 0.02\ mm$, $W_n = 0.25\ \mu m$, $V_{max} = 0.4\ V$,$J_{max} = 0.02\ A/cm^2$ and $D = 10\ mm$. Thus the grid cell is $10 \times 5\ mm$ with a total shadowed area of 9%.

5.5 Experimental Methods

The dark and photo I–V characteristics of the samples were measured using a Keithley 236 Source-Measure Unit and a 1 kW quartz halogen tungsten (QHT) lamp as a light source, both were described in Sec. 3.3. The monochromator and detection system consisted of the ISA 0.32 m spectrograph and a cooled InGaAs photodetector. The spectral throughput of the monochromator was calibrated using a Newport NIST traceable power meter. The standard phase lock-in technique was used to register photoluminescence (PL) and photocurrent (PC) spectra. For PL measurements, a 0.5 W diode laser with $\lambda = 681$ nm was used as an excitation source. A set of PL spectra for the different voltage bias and excitation intensity was measured. The PC spectra were measured as a function of bias and excitation wavelength. Power dependence of the photovoltaic efficiency was measured us-

Sample	V_{oc}, V	J_{sc}, mA/cm^2	Fill Factor, %	Abs. Eff., %	Rel. Eff., %
MQW	0.44	12.03	53	3.02	113
control	0.62	6.78	61	2.68	100

Table 5.1: Parameters of the InGaAsP/InP MQW and control InP solar cell samples as measured under 100 mW/cm^2 illumination of the QHT lamp ($T_{col} \simeq 3000^\circ$ K).

ing the QHT lamp and a set of neutral density filters. All measurements were performed at room temperature.

5.6 Results

5.6.1 Efficiency Measurements

Table 5.1 shows the measured (V_{oc}, open-circuit voltage, and J_{sc}, short circuit current density) and calculated (FF and η) parameters of the MQW and control samples under 100 mW/cm^2 illumination of the QHT lamp (color temperature $T_{col} \simeq 3000^\circ$ K).

The MQW sample showed, an average, ~13% increase in the photovoltaic efficiency (η_{inc}) over the control sample. This was calculated using

$$\eta_{inc} = \frac{\sum_i \eta_i^{MQW} - \sum_j \eta_j^{ctrl}}{\sum_j \eta_j^{ctrl}} \times 100 \tag{5.11}$$

It can be seen that this enhancement comes from the two-fold increase in the J_{sc}. It should be noted that these samples were not optimized in terms of the efficiency. They would certainly benefit from optimization of the top emitter layer, *i*-layer and an anti-reflection coating. Based on the model of an ideal QWSC described in Sec. 2.4.3, we have calculated the V_{oc}^{MQW} of the MQW sample and compared it with the experimental results. We found that the measured value of $V_{oc} = 0.44$ V is in a good agreement with the predicted value of 0.43 V, and, as found by other groups, the drop in the open circuit voltage

$\Delta V_{oc} = V_{oc}^{control} - V_{oc}^{MQW}$ is less than the bandgap difference $\Delta E_{gap} = E_{gap}^{InP} - E_{gap}^{InGaAsP}$.

From the measured I–V curves we have calculated the photovoltaic efficiency η versus the QHT lamp light intensity which is plotted in Fig. 5.8.

$$\eta(P_{inc}) = \frac{V_{max}(P_{inc}) J_{max}(P_{inc})}{P_{inc}} \tag{5.12}$$

where V_{max} and J_{max} are measured at the maximum power point, and P_{inc} is an incident power per unit area. Both samples demonstrate an identical behavior: initial rise of the efficiency for 0–50 mW/cm^2 range, which becomes saturated at higher light intensities (200–250 mW/cm^2). Because of this similarity, we believe that this behavior is caused by the same mechanism as is discussed later. The MQW sample showed the higher efficiency than the control sample throughout all investigated range of intensities. The inset shows relative increase η_{inc} as a function of incident power. Note that η_{inc} becomes less at higher power.

5.6.2 Transmission and Reflection Measurements

Fig. 5.9 and Fig. 5.10 show transmission ($\mathcal{T}$) and reflection ($\mathcal{R}$) curves for both samples, respectively. For clarity, the insets show the difference of corresponding curves. Transmission of the control sample in the 970-1300 nm range is 2-3% higher than the transmission of the MQW sample. This is consistent with the band structure of the samples. Slow decay of the $\mathcal{T}$ above 1100 nm is caused by free carrier absorption process, which intensity is proportional to λ^4.

At the same time the reflection difference in that region reveals an interesting fact – the reflection of the MQW sample is higher. It means that compared to the control sample fewer photons are penetrating inside the MQW sample. The absolute values of reflectivity are in between 28 and 40 per cent which means that roughly one third of the incident light is reflected back without producing photocurrent. Both samples would certainly benefit

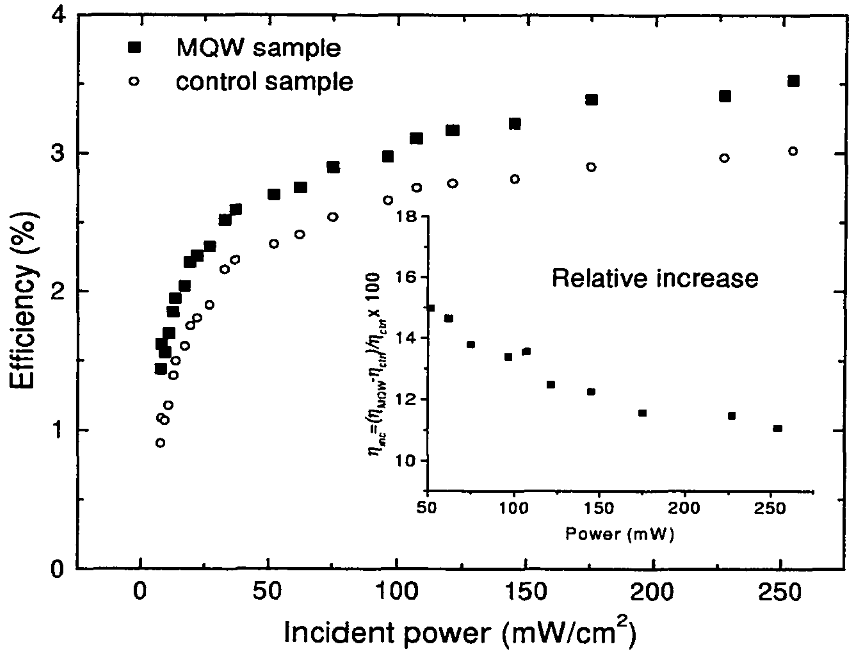

Figure 5.8: Photovoltaic efficiency of the InGaAsP/InP MQW and InP solar cell samples vs. the white light illumination intensity.

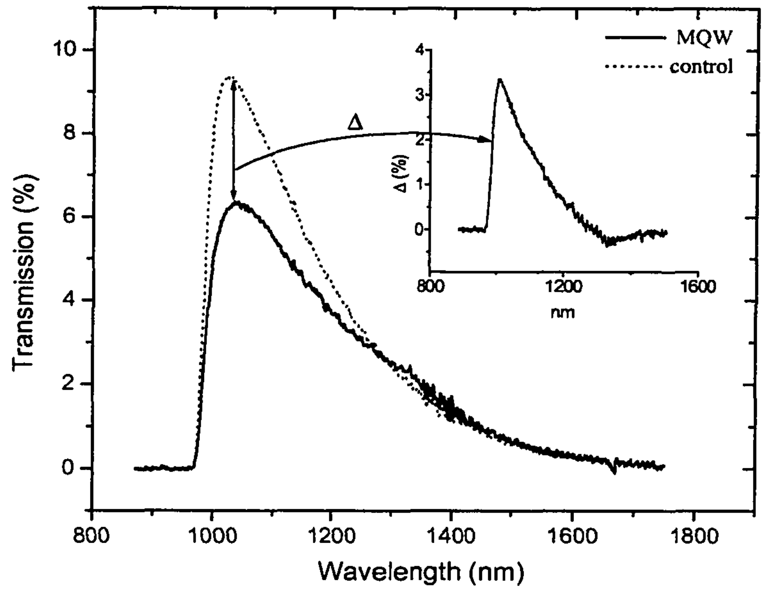

Figure 5.9: Transmission of the MQW and control samples. The inset shows difference. Solid line – MQW; dotted line – control.

from anti-reflection coating.

5.6.3 Effect of the Top Layer on Cell Performance

Resistivity To estimate the effect of the top layer resistivity on sample performance we have conducted the following measurements. A schematic of the experiment is shown in the inset of Fig. 5.11. A piece of the sample wafer with a single strip of gold contact was irradiated by a tightly focused laser beam (diameter of the beam spot is less than 0.05 mm). The position of the sample in relation to the spot was changed in steps of 0.5 mm and at each step the photocurrent was measured. The resulting curves for both samples are shown in Fig. 5.11. The sharp drop in the PC denotes the position where the beam crosses the gold contact. We have found that at the distance 7 mm from the contact the PC

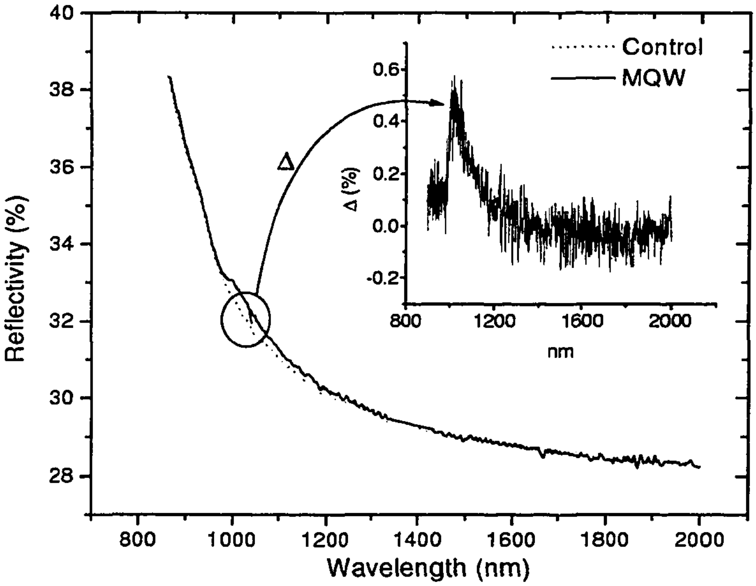

Figure 5.10: Reflectivity of the MQW and control samples. The inset shows difference. Solid line – MQW; dotted line – control.

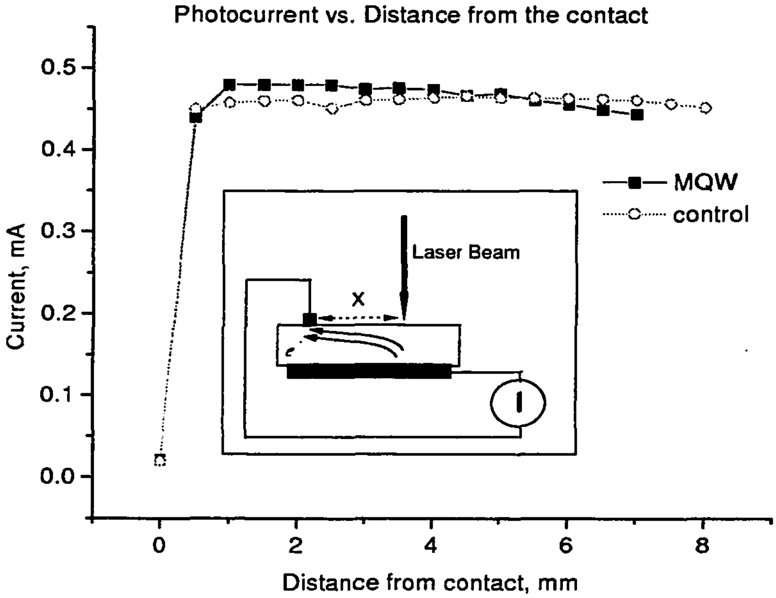

Figure 5.11: Photocurrent versus distance from the metal contact. The inset shows a experiment schematics.

drops by 9% from its maximum value. However, this appears to be not a very important factor because the longest distance the photocarriers have to travel to reach grid contacts is less then 2.5 mm (from the center of 10 x 5 mm grid cell), and at this point the photocurrent is still at its peak value (see Fig. 5.11).

Thickness To estimate the effect of the top layer thickness on the cell performance we have etched off this layer in several steps. At each step the photoresponse was measured. The etching was done in H_2O_2:HBr:H_2O (1:1:25) solution. Prior to etching all parts of the sample not subject to removal were covered with wax. Etching was done for both samples. Fig. 5.12 shows the photoresponse curves taken consequently at the beginning, and after 2 min and 10 min exposure to the etching solution.

The effect of etching is clearly observable in both samples. The control sample shows an

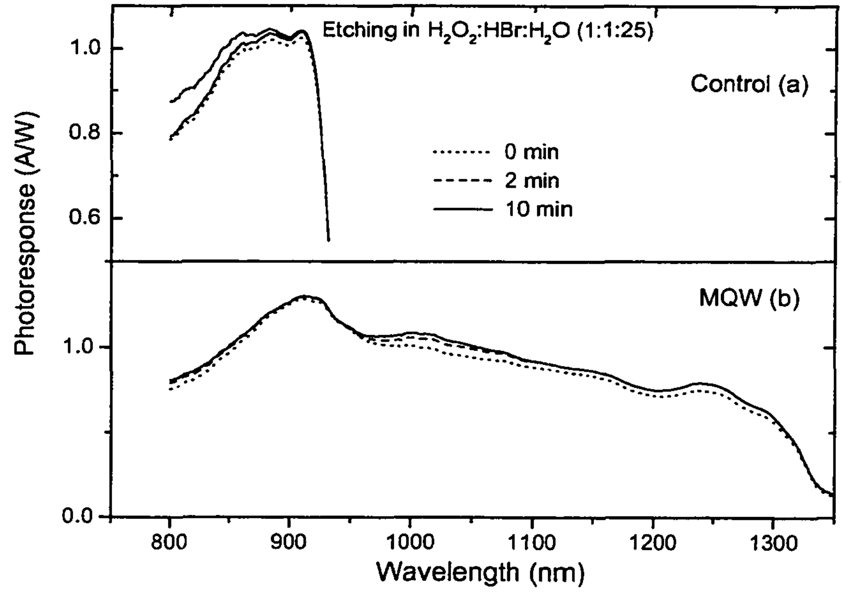

Figure 5.12: Photoresponse curves of the InP (a) and MQW InGaAsP/InP (b) solar cell samples exposed to H_2O_2:HBr:H_2O (1:1:25) etching solution. Dotted lines are the start (no etching done), dashed lines are after 2 min etching, solid lines are after 10 min etching.

improved spectral response in "blue" part of the spectrum, and the MQW sample demonstrates an improvement in all parts of the spectrum. This behavior can be explained by relative ineffectiveness of the top layer in terms of photovoltaic conversion efficiency. Although this layer is essential in creating a $p-n$ junction, due to the lack of electric field inside this layer the only possible transport mechanism is carrier diffusion, which is, in turn, severely affected by the high dopant concentration. Etching off a part of this layer has allowed more photons (especially with the energy $\hbar\omega \geq E_{gap}^{InP}$, InP bandgap) to get inside the high-field region and thus, improve collection efficiency.

Increase of the efficiency as a result of reducing of the emitter thickness was also confirmed by detailed solar cell device simulations[1]. Fig. 5.13 shows the efficiency of the InP solar cell similar to the control sample plotted against the thickness of the top layer. It is seen that the reduction of the thickness has indeed a very dramatic effect on the cell performance.

5.6.4 Photocurrent and Photoluminescence Measurements

Fig. 5.14 shows the spectral photoluminescence and photoresponse (photocurrent as a function of excitation wavelength) for the MQW and control samples measured at zero bias. We have identified the peaks in the PC and PL spectra and found them in good agreement with the calculated values of the optical transitions inside the InGaAsP/InP quantum well. Detailed study of the quantum well states is contained in the next section.

It can be seen that the addition of the quantum wells extended the PC spectral response beyond 920 nm (E_{gap}^{InP}) up to 1300 nm ($E_{gap}^{InGaAsP}$). At the same time, the MQW sample showed a slight decrease in the PC magnitude compared to the control sample for the wavelengths below 920 nm.

Fig. 5.15 shows the PC and PL intensities of the MQW and control samples as a function of the applied bias voltage, measured at the wavelengths corresponding to the PL peaks

---

[1] The data were calculated using David Winstone's **SimWindows32** – optoelectronics device simulator developed at University of Colorado, Boulder.

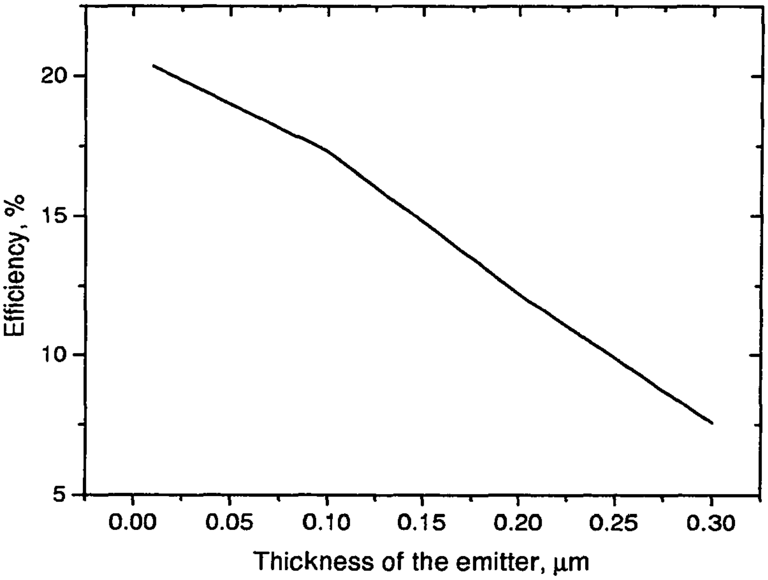

Figure 5.13: Solar cell efficiency vs emitter (top layer) thickness.

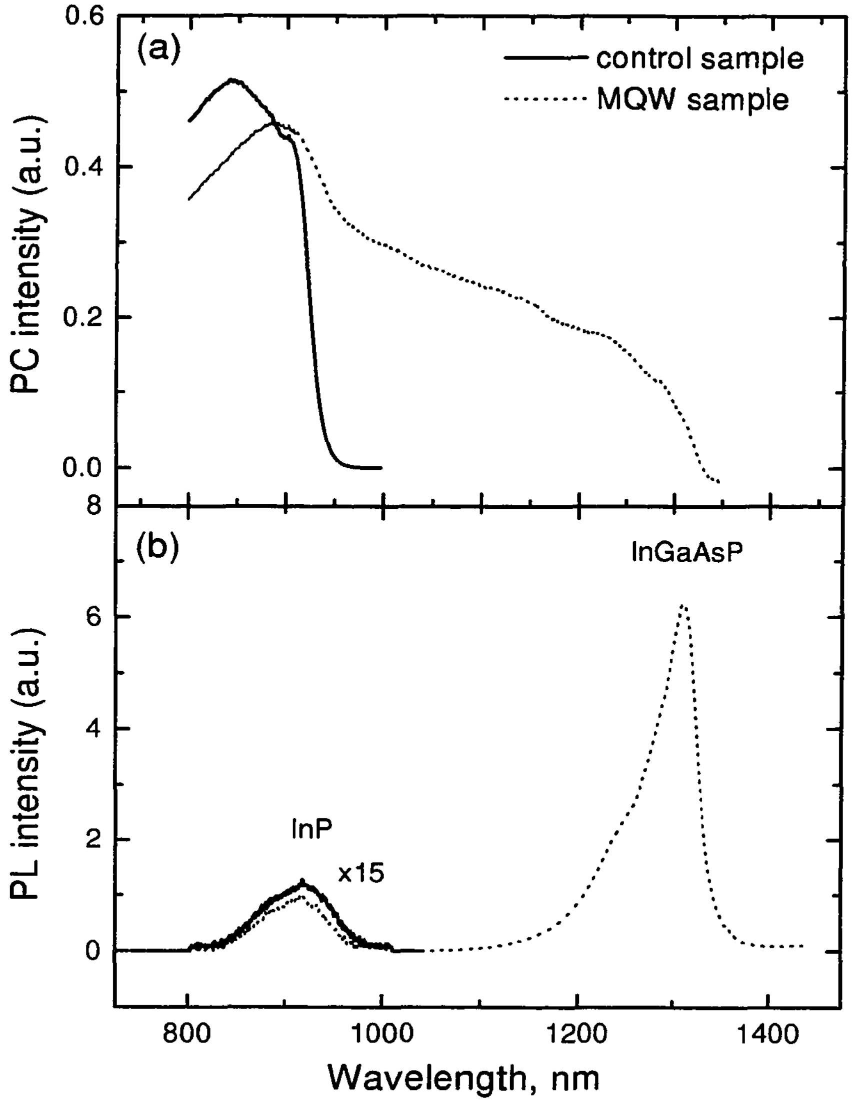

Figure 5.14: Photoresponse (photocurrent vs. excitation wavelength) and photoluminescence intensities of the InGaAsP/InP MQW and InP solar cell samples at zero bias. InP PL peaks are 15 times magnified.

(920 nm for the control sample, 920 nm and 1300 nm for the MQW sample).

The PL intensity I_{PL}^{InP} of the InP control sample displays the following behavior: when $V_{bias} < 0.25$ V, the I_{PL}^{InP} does not change with the bias and has a *non-zero* value, when $V_{bias} > 0.25$ V, I_{PL}^{InP} rises with the bias. It should be noted that all changes happen in the positive bias region. The drop in the PL has a corresponding increase in the PC intensity.

The MQW sample exhibits different behavior from the control sample. The PL intensity of the first peak (920 nm) does not depend on the voltage bias. The intensity of the second PL peak (1300 nm) slowly decreases with decreasing bias and approaches nearly *zero* value. The peak continues to exist in the negative voltage bias region.

The photocurrent of the control sample at 920 nm shows an increase in the intensity towards decreasing values of bias, and the intensity saturates at negative bias. After an initial rise, the photocurrent of the MQW sample at the 1300 nm excitation wavelength reaches a maximum located around zero bias and begins to fall due to the Stark effect. The 920 nm MQW PC behaves more like the analogous peak of the control sample. Both MQW PC plots show an increasing noise level in the negative bias range. We attribute this to the rising influence of the dark current shown in the insert. It is worth to mention that the slopes of the PC increase in both samples are approximately the same and they are different from the corresponding slopes of the PL decrease.

5.7 Discussion

Based on the bias and excitation wavelength dependence, we were able to distinguish the contribution to the PL and PC from the different layers of the samples. To explain PL voltage dependence we assume that the 920 nm peak of the PL spectra arises from the contribution of the top *n*-InP layer and the InP part of the *i*-layer. Due to the high resistance of the undoped layer, most of the voltage drop and, consequently, changes in the electric field experienced by the photocarriers occurs in this region. Since the MQW

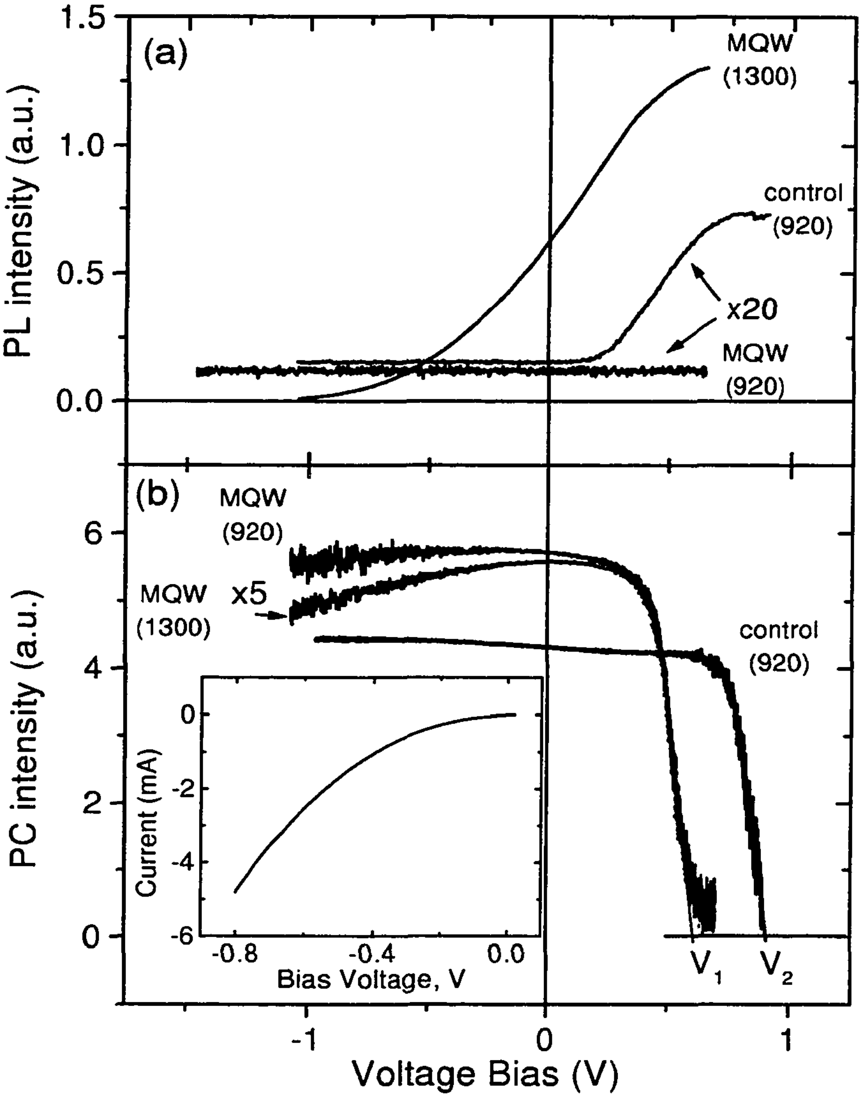

Figure 5.15: Photoluminescence (a) and photocurrent (b) intensities of InGaAsP/InP and InP solar cell samples vs. voltage bias measured at the fixed wavelengths: $\lambda = 920$ nm for the control sample, and $\lambda = 1300$ and 920 nm for the MQW sample. 920 nm PL is 20 times magnified. 1300 nm PL is 5 times magnified. The insert shows the dark current of the MQW sample. V_1 and V_2 are cutoff voltages (see text for the explanation).

PL peak at 920 nm is completely independent of the bias, we can conclude that there is no steady-state photoluminescence from the InP barriers of the MQW sample, which means that the photocarriers generated inside the barriers get captured in the wells on a time scale significantly faster than the radiative recombination lifetime. This process remains unaffected by the changes in the field produced in our experiments.

The control sample, on the other hand, displays strong PL at 920 nm (Fig. 5.15a) from the undoped region, which constitutes approximately 80 % of the total 920 nm emission measured at $V_{bias} = +1.0$ V (when the PC signal is equal to zero). Starting from $V_{bias} = +0.25$ V and below, the radiative recombination inside the undoped layer is effectively suppressed. The shape and the intensity of the 920 nm PL peak at zero bias (see Fig. 5.14a) is almost identical in both samples, which supports the assumption that it has the same origin - top InP layer.

The PL emission at 1300 nm of the MQW sample originates in the quantum wells. It continues to be present even at negative bias, which means that the carriers remain trapped inside the wells, and the field of 50 kV/cm and higher is required to quench radiative emission.

The cutoff voltage V_{cut}, the voltage bias when the photocurrent practically disappears, corresponds to the situation when the internal field is no longer strong enough to separate the carriers and produce the photocurrent. The values of the V_{cut} are different for the MQW and control samples: for the control sample $V_{cut} = 0.91$ V (V_2 in Fig. 5.15b) and for the MQW sample $V_{cut} = 0.62$ V (V_1 in Fig. 5.15b). The equation describing the current-voltage dependence of the *p-n* junction under monochromatic illumination is given by:

$$I_{p-n}(V,\lambda) = I_{dark}(V) - I_{pc}(V,\lambda) \tag{5.13}$$

where I_{dark} and I_{pc} are the dark current and photocurrent, respectively. The V_{cut} can be regarded as an upper limit of V_{oc} for the given sample, that is the value V_{oc} would have reached if there were no dark current present. The difference $\Delta V_{cut} = V_2 - V_1$ is equal to

0.29 V and falls between ΔV_{oc} and ΔE_{gap}. The fact that $\Delta V_{oc} \neq \Delta V_{cut}$ is explained by the differences in the $I_{dark}(V)$ of the samples.

The MQW sample was designed to have the built-in resonant tunneling alignment, which means that if there is any possible photocurrent enhancement, then it should be found at $\approx$ +0.3-0.5 V voltage range. It can be seen that the PC of the MQW sample at 1300 nm excitation wavelength does display a broad peak with a maximum located near the aforementioned region. Although it can not serve as conclusive evidence of resonant alignment (for instance, one would expect the PL intensity at 1300 nm to have a matching minimum, which was not observed), we consider it to be supportive that resonant tunneling occurred in the MQW sample. The next chapter will discuss this issue in greater details.

The presence of significant non-radiative recombination in the MQW sample can be deduced from the fact that despite the decline of the 1300 nm PL emission in the negative bias region, the 1300 nm PC does not experience any rise there. According to the balance equation, the difference is absorbed by increase in the non-radiative recombination rate.

The similarity of the MQW and control samples in the power dependence of efficiency (Fig. 5.8) can be explained in terms of the saturation of carrier traps centers. At low power intensities and low excited carrier densities, these traps are active and limit the current and efficiency; as the power increases, fewer traps remain available and the efficiency saturates.

5.8 Conclusion

We have investigated InGaAsP/InP MQW solar cell samples, which were designed and fabricated to have a sequential resonant tunneling alignment between adjacent wells. The photovoltaic efficiency of the MQW cell showed an average 13% increase compared to the control InP (non-MQW) sample. The voltage bias and excitation wavelength dependence of photoluminescence and photocurrent for the MQW and control samples were measured, and the contributions from the different layers of the samples to the PC and PL were identified. Reflection measurements and etching off the top layer have suggested that the photovoltaic efficiency of the both samples can be improved by: (1) putting on an antireflection coating, and (2) reducing the thickness of the top layer. The latter has to be done in conjunction with grid contact optimization.

Chapter 6

Resonant Enhancement of the Photocurrent in MQW Photovoltaic Devices

6.1 Introduction

This chapter is focused on the investigation of *sequential resonant tunneling* (SRT) inside the InGaAsP/InP MQW solar cell structure and its effect on improving the photovoltaic efficiency. Two samples, an MQW InGaAsP/InP heterostructure with built-in sequential resonant tunneling (SRT) transfer and a control InP sample, were designed, grown and investigated. The samples were fully characterized using photoluminescence and photocurrent spectroscopies [61]. *Electroreflectance spectroscopy* (ER) and *secondary ion mass spectrometry* (SIMS) were used to investigate dopant profiles and electric field distribution in the *i*-region of the samples. ER measurements were conducted by Dr. A. Jaeger in Brooklyn College of CUNY and SIMS profiles were obtained by Dr. M. Geva of Lucent Technologies.

Solar cells based on the multiple quantum well structures have been actively studied for the last decade. It has been shown that the insertion of quantum wells (QW) inside a *p-i-n* structure extends the cell absorption spectrum and increases the short circuit current (I_{sc}).

An efficient escape and transport of the photoexcited carriers across the MQW region strongly determine the performance of the QW solar cell. The carrier escape mechanisms fall into several categories: thermionic emission of carriers above the barrier, a process which depends primarily on barrier height and temperature; tunneling out of the well, which exponentially depends on barrier width; escape via an absorption of optical phonons, a process which is affected by temperature, and the combination of the last two (phonon-assisted tunneling) [14]. These processes are competing against radiative and non-radiative recombination, which tends to diminish the photocurrent.

It is known that the radiative recombination rate in quantum well structures is significantly larger than that in similar non-QW structures due to spatial localization of the carriers. Although it is beneficial for light-emitting devices such as lasers and LEDs, it is a disadvantage for solar cells due to reduction of the photogenerated current. However, in resonantly coupled wells, the electron transfer time between adjacent wells is reduced by several orders of magnitude compared to non-resonant cases, which overcomes large radiative losses and produces a significant amplification of the photocurrent as was observed by Capasso *et al.* [15,16].

Barnham and Duggan (B&D) [6] suggested to build an MQW structure shown in Fig. 6.1 where several QW were chosen in such a way that their ground states were aligned in resonance. This particular design, which we will call *non-SRT* to distinguish it from our proposal has a major drawback: for a sensible range of well widths (30-200 Å) there are only 5 or 6 wells which can be simultaneously put in resonance with each other. It gives a thickness of MQW layer of $\approx 0.1\mu$, which is certainly not sufficient to absorb all solar radiation. To compensate for low absorption B&D suggested to add several *not-in-resonance* wells to the end of the MQW stack. However, in our opinion, it defeats the whole purpose of having resonant tunneling transfer in the first place. After passing through the

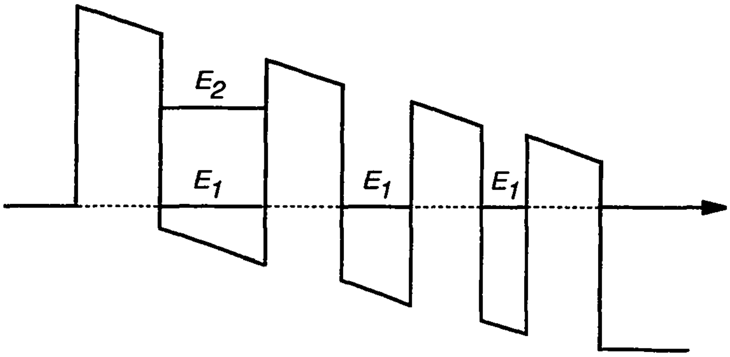

Figure 6.1: Non-sequential resonant tunneling arrangement in MQW heterostructure.

first "resonant" region, carriers will tend to accumulate in the region with slow transfer capabilities. To overcome this deficiency we have proposed a SRT MQW solar cell (see Fig. 6.2).

6.2 SRT in MQW Structures

An MQW structure with SRT is shown in Fig. 6.2a. Electrons tunnel from the ground state of the j-th well ($j = 1, 2, \ldots, N$) into an excited state of the $(j+1)$-th well. The tunneling process is then followed by intraband energy relaxation from the excited state to the ground state. This two-step scheme can be repeated as many times as needed to build the required thickness of the MQW layer for optimum solar absorption. Resonance occurs if the following condition is satisfied: $E_2 - E_1 = |q\vec{F}d|$ where E_1, E_2 are, respectively, the ground and first excited subband energy of the quantum well, q the electron charge, $\vec{F}$ the total electric field in the MQW region, and d the MQW spatial period. For comparison the same structure with non-resonant value of the internal field is shown in Fig. 6.2b.

To obtain possible combinations of barrier and well widths which satisfy the sequential tunneling condition we have graphically solved the aforementioned equation as shown in Fig. 6.3, where the squares represent the calculated difference $\Delta E = E_2 - E_1$ as a function of well width, and the solid lines are qFd for several values of barrier width. The

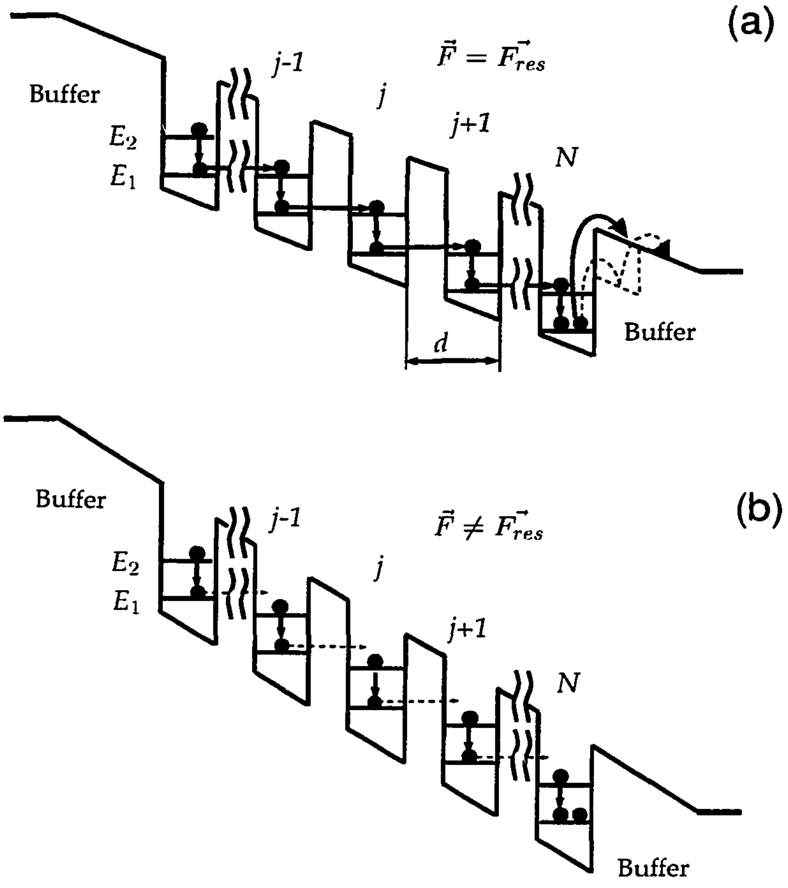

Figure 6.2: Sequential resonant tunneling transfer in an MQW structure. E_1 and E_2 are the energies of the ground and first excited states in the quantum well, respectively, d the superlattice period, and $\vec{F}$ the internal field. (a) – the structure is in a resonance, $F = F_{res}$; (b) – the structure is out of resonance, $F \neq F_{res}$.

actual electric field experienced by the carriers inside the intrinsic layer is reduced from its nominal value because of the photovoltaic effect and:

$$|\vec{F}| = (V_{bi} - V_{pv})/L \tag{6.1}$$

where V_{pv} is the photogenerated voltage, V_{bi} the built-in potential and L the thickness of the intrinsic layer. The field value we used for calculating "resonant" barrier and well widths was $|\vec{F}| = 0.8V_{bi}/L = 25$ kV/cm. This corresponds to a situation when a InGaAsP/InP solar cell with $L = 0.4$ μm operates approximately at a maximum power point where $V_{max} = 0.3 - 0.4$ V [62]. The difference between the ground and first excited subband energies, ΔE, was calculated using the transfer matrix method with the following material parameters: 0.925 eV for the bulk InGaAsP bandgap, 0.170 eV for the conduction band offset, and $0.079m_0$ and $0.056m_0$ for the InP and InGaAsP electron effective masses, respectively. For a given band offset, the lower limit on the width is imposed by the requirement of having at least two subbands inside the well (60 Å in our case). The upper limit was set based on the following arguments.

From Fig. 6.3 it can be seen that the intersubband transition $E_2 \rightarrow E_1$ plays a major part in the SRT. It is generally accepted that the intersubband relaxation in narrow wells, where the subband separation is larger than the polar optical phonon energy is controlled primarily by polar optical phonon emission. Measured values for the electron lifetime in the upper subband are very short, of the order of half of a picosecond [63], which is in good agreement with theoretical estimates of the electron-phonon scattering rate [64].

In wide wells, where the subband separation is smaller than the polar optical phonon energy, electrons at the bottom of the first excited subband are forbidden from the emitting a optical phonon, and thus the intersubband relaxation becomes rather slow, which was indeed observed, on the order of several hundred picoseconds. At the same time, much shorter time constants, between 15 and 40 ps, have been also reported [65]. Dür, Goodnick and Lugli (DGL) have conducted a thorough ensemble Monte Carlo simulation of interband relaxation in wide GaAs/Al$_x$Ga$_{1-x}$As quantum wells. They have studied quantum wells with a subband separation smaller than $\hbar\omega_{LO}$. Intra- and intersubband scattering through polar optical phonons, acoustic phonons, ionized impurities, and electron-electron scattering are included in the simulation. DGL results showed that the intersubband decay of electrons from the first excited subband into the ground subband is limited by ionized impurity scattering. Optical phonons emission also contributes considerably to the electron decay and occurs from the thermal tail of the heated distribution function in both subbands. The heating of the distribution functions is due to ionized impurity intersubband scattering and electron-electron intrasubband scattering, which convert potential energy of an electron to kinetic energy. The phonon induced transition rate of a single transition between two states $|n, \boldsymbol{k}\rangle$ and $|n', \boldsymbol{k'}\rangle$ is given by Fermi's golden rule:

$$W_{n,n'}(\boldsymbol{k}, \boldsymbol{k'}) = \frac{2\pi}{\hbar} |\langle n'\boldsymbol{k'}, N_q \pm 1 | H_{e-ph} | n\boldsymbol{k}, N_q\rangle|^2 \delta(E_{n'} + E_{k'} \pm \hbar\omega - E_n - E_k) \tag{6.2}$$

where E_n and $E_{n'}$ are the band-edge energies of the n-th and n'-th subbands, $\boldsymbol{k}$ and $\boldsymbol{k'}$ are the in-plane wave vectors of the initial and the final states, respectively, $E_k = \hbar^2 k^2/2m$ is the in-plane energy, ω is the frequency of a given phonon mode, and N_q is the phonon population, ± refers to phonon emission (+) and absorption (-) processes. The ratio of the emission and absorption rates is equal to $\exp[\hbar\omega/k_B T]$. For a typical phonon energy of 35 meV and $k_B T \approx 26$meV, this ratio is equal 4. For the sequential resonant tunneling process it is desirable that emission rate was much higher than absorption rate. This can achieved by choosing $E_2 - E_1 > \hbar\omega_{LO}$ so that absorption process is not energetically allowed.

Then the upper limit can be set by demanding that $\Delta E \geq \hbar\omega_{LO}$, where $\hbar\omega_{LO} \approx 35$ meV is the optical phonon energy [20]. This sets an upper limit at about ~ 200 Å. The thickness of the barriers should not be very large (≤ 100 Å) because thick barriers will result in a low

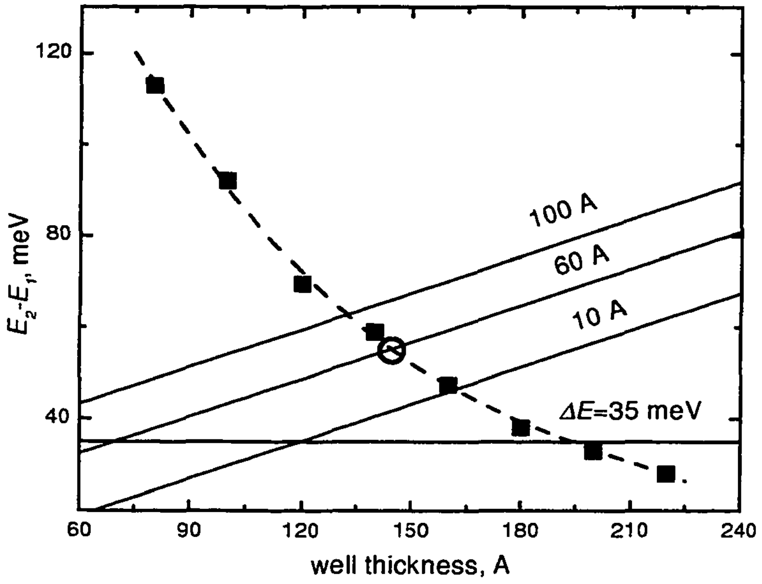

Figure 6.3: Graphical solution of the equation $E_2 - E_1 = |q\vec{F}d|$. Squares show the calculated difference $E_2 - E_1$, where E_1 and E_2 are the energies of the ground and first excited states in the quantum well (the dashed line is the interpolating polynomial); the solid straight lines are $qF(w + b)$ for different values of barrier width; the horizontal line is drawn to mark the $\Delta E = 35$ meV boundary. The open circle marks the intersection 140Å well and 60 Å barrier chosen as "resonant" values for our sample.

tunneling rate, nor it should be too small ($\geq$ 10 Å), as it has been reported that MQW solar cells with narrow barriers do not perform very well in the short wavelength range. This choice of barriers reduces the useful range of the wells to 120–150 Å. For our sample we have chosen 140 Å for the well and 60 Å for the barrier widths (it's marked with an open circle in Fig. 6.3.

6.3 Samples and Experimental Setup

Under these considerations we have designed and investigated an InGaAsP/InP MQW heterostructure solar cell. The MQW layer of the cell consisted of 16 periods of 140 Å InGaAsP wells ($E_{gap} = 0.95$ eV), separated by 60 Å InP barriers with a total thickness of 0.31 μm. The MQW region was confined by undoped InP 500 Å buffer layers, which made the total thickness of the i-layer equal to 0.41 μm. The measured characteristics of this cell were reported in the previous section.

The I–V (dark current) characteristics of the samples were measured using a Keithley 236 Source-Measure Unit. Photoluminescence and photocurrent spectra were measured using a standard phase lock-in technique. The monochromator and detection system consisted of an ISA 0.32 m spectrograph, 100 W quartz halogen tungsten lamp, and a cooled InGaAs photodetector.

Knowledge of the internal electric field and charge distribution is an essential element of solar cell investigation and so the additional methods capable of providing this information have been used to characterize the samples: electroreflectance (ER) and secondary ion mass spectrometry (SIMS). ER measurements were conducted by Dr. A. Jaeger in Brooklyn College of CUNY and SIMS profiles were obtained by Dr. M. Geva of Lucent Technologies. The following briefly describes each technique.

6.3.1 Modulation Spectroscopy: Electroreflectance

Modulation spectroscopy is a very important tool in studying optical properties of semiconductors. It is particularly useful in investigation of semiconductor dielectric function $\varepsilon(\omega) = \varepsilon_r(\omega) + i\varepsilon_i(\omega)$, where ε_i and ε_r are the imaginary and real parts of the dielectric function, respectively. Instead of measuring the dielectric function itself various modulation techniques measure one of its derivatives. This eliminates the background and reveals the interband critical points as the sharp peaks in the modulation spectrum.

Electroreflectance spectroscopy (ER) is one of the various modulation techniques where the modulation is produced by an applied *ac* electric field. The ER signal $\Delta\mathcal{R}$ is detected by a lock-in amplifier and normalized to the average intensity of the transmitted or reflected beam $\mathcal{R}$ and to the amplitude of the modulating agent. In this manner the logarithmic derivative of the reflectance with respect to the modulation signal is obtained while the dependence on the intensity of the incident light is eliminated.

One of the important applications of the ER spectroscopy is its capability to determine the value of the electric field inside semiconductors based on the *Franz-Keldysh oscillations* (FKO). The following paragraph is a brief description of the Franz-Keldysh effect and its relation with oscillations in ER spectra.

Franz-Keldysh effect and ER spectroscopy The effect of the electric field on the absorption edge is known as the *Franz-Keldysh effect*. In the presence of an electric field F, ϵ_i is no longer zero below the band gap E_{gap} but decreases exponentially. The oscillations of $\epsilon_i(\omega)$ above the band gap are known as *Franz-Keldysh oscillations* (FKO). These changes in behavior of ϵ can be explained by spatial band tilting. As a result, the bandgap vanishes, and an electron can make a transition from the valence band to the conduction band by tunneling. It can be shown that around the critical point E_0 the ER spectra should exhibit a sharp peak at the energy E_0, decay rapidly below E_0, and oscillate rapidly above E_0. The ER spectra can be approximated as

$$\frac{\Delta\mathcal{R}}{\mathcal{R}} \propto \frac{1}{E^2(E-E_0)} \exp[\frac{(E-E_0)^{1/2}\Gamma}{(\hbar\Omega)^{3/2}}] \cos(\frac{2}{3}(\frac{E-E_0}{\hbar\Omega})^{3/2}+\theta) \tag{6.3}$$

where E is the photon energy of the probe beam, E_0 is the energy of the critical point responsible for the FKO, Γ is the broadening parameter, Θ is an arbitrary phase factor, and

$$4(\hbar\Omega)^3 = (\frac{(e|F|\hbar)^2}{2\mu}) \tag{6.4}$$

Given the mobility μ the electric field F can be deduced from the curve fitting.

In our work the ER results were used for the following purposes: (1) to test contact quality (ohmic or rectifying) and (2) to evaluate average field inside the intrinsic layer.

6.3.2 SIMS

Secondary ion mass spectrometry (SIMS) is a very powerful technique for the analysis of impurities in solids. This technique relies on removal of material from the sample by sputtering and subsequent analysis of the sputtered ionized atoms. It allows simultaneous detection of different elements and has a depth resolution of 50 to 100 Å. Unlike photoluminescence, electroreflectance or photocurrent spectroscopies, SIMS is a destructive method.

A SIMS doping concentration profile is produced by sputtering the sample with an ion gun (Ar^+ or Ce^+) and monitoring the SIMS signal of a given element as a function of time. The *time axis* is later converted to a *depth axis* by measuring the depth of the crater at the end of the measurement. The SIMS signal is converted to *impurity concentration* through standards of known dopant profile. The proportionality between ion signal and doping concentration is strictly observed if the matrix in which the impurity atom is contained is uniform. The important characteristic of SIMS is that it determines the *total* impurity concentration, not the *electrically active* impurity concentration. SIMS can not be used if the dopant is not a foreign impurity but it is due to a stoichiometric defect (*e.g.* a vacancy).

6.4 Results

6.4.1 Photoluminescence and Photocurrent Measurements

Identification of Quantum Well States We begin with identification of energy states in the quantum well. Fig. 6.4 shows photoresponse $I_{pc}(E)$ of the MQW sample measured at different voltage bias V_{bias}. The effect of the changing bias is clearly observable: as volt-

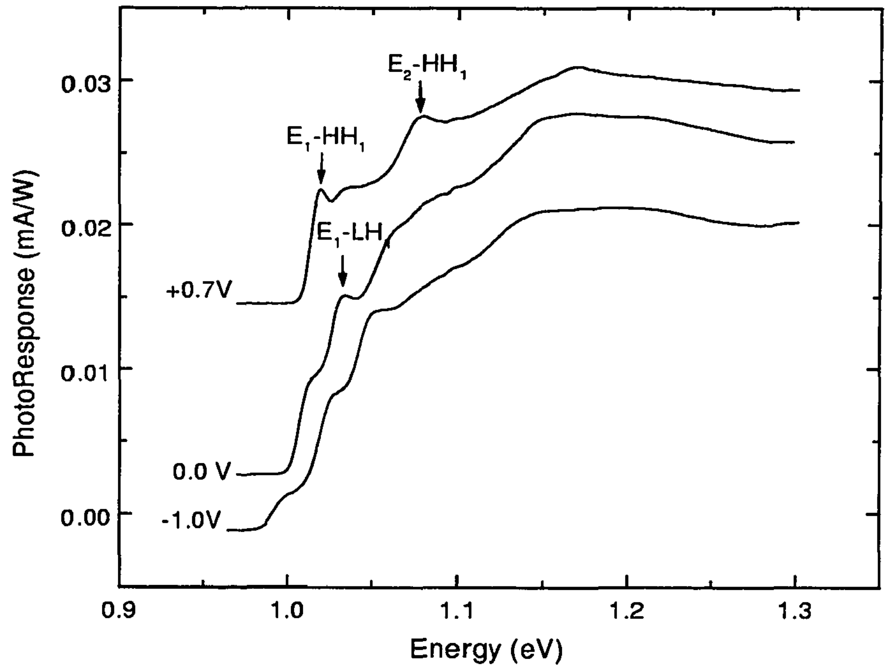

Figure 6.4: Photoresponse of the InGaAsP/InP MQW sample at 77 K measured at different bias voltage.

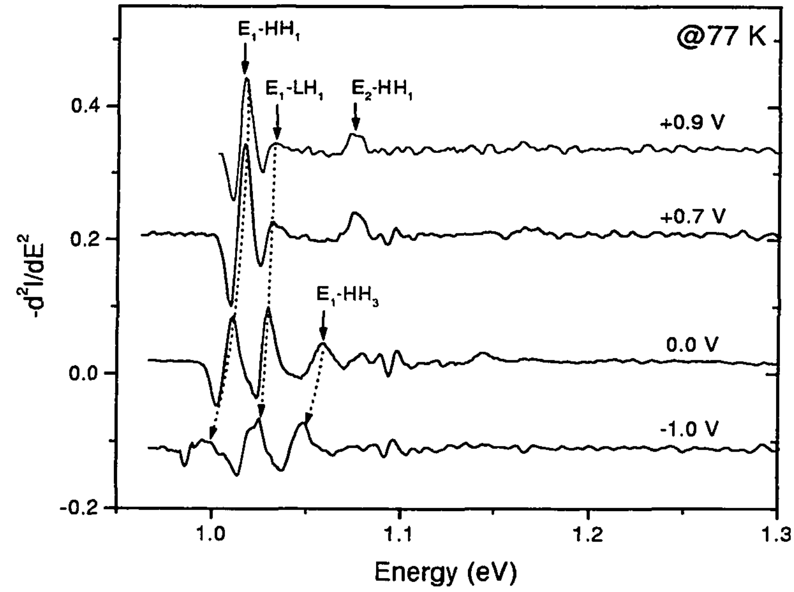

Figure 6.5: Evolution of the PC features with the bias: second derivative of the InGaAsP/InP MQW sample at 77 K measured at different voltage bias. Dotted lines are drawn to show changes in PC peak positions due to the QCSE (Stark Effect). +0.7 and +0.9 V curves are in the "resonant" range

age goes from -1.0 V to +0.7 V the amplitude of the various spectral features changes. To get peak positions more accurately the second derivative of the I_{pc} ($-d^2I_{pc}/dE^2$) was calculated. Table 6.1 lists some prominent experimental peaks and calculated quantum well energy states. There is a very good agreement between experiments and calculations. In the calculation the following InGaAsP material parameters [62] were used: $m_e = 0.056m_0$, $m_{lh} = 0.079m_0$, $m_{hh} = 0.46m_0$, and conduction band offset $\Delta E_c = 0.168$ eV.

Fig. 6.5 shows several plots of ($-d^2I_{pc}/dE^2$) taken at selected V_{bias}. One can observe interesting behavior – there are some features which are present at all V_{bias} ($E_1 - HH_1$ and $E_1 - LH_1$), and, at the same time, there are peaks which only exist in limited bias range ($E_2 - HH_1$, $E_1 - HH_3$). This is better illustrated in Fig. 6.6, where the positions of these

Number	Experiment	ID	Calculation
1	1.018	$E_1 - HH_1$	1.018
2	1.034	$E_1 - LH_1$	1.034
3	1.059	$E_1 - HH_3$	1.050
4	1.077	$E_2 - HH_1$	1.075
5	1.090	$E_2 - HH_2$	1.091
6	1.146	$E_2 - LH_2$	1.146
7	1.164	$E_1 - LH_3$	1.171

Table 6.1: A list of energy values of prominent features in PC spectra together with calculated values of quantum well states. $T = 77\ K,\ V_{bias} = 0.3\ V$.

peaks are drawn against V_{bias}. One can see that the lowest plot ($E_1 - HH_1$ transition) is the most sensitive to bias, its total shift is 0.03 eV compared to ≈ 0.01 eV for others curves. This agrees with the fact known from EFA calculations that ground states of the quantum well experience the largest red shift.

Observation of the SRT

The most interesting feature of the MQW sample is its SRT capability. We have found multiple evidence of resonant alignment occurring in the MQW sample.

Dark Current Fig. 6.7 shows the measured dark current versus applied bias at different temperatures in steps of ≈ 20 K. All curves clearly indicate the presence of a resonance peak located at 0.9 V (77 K). To estimate the position and width of the resonance peak more accurately, we assumed that the I-V characteristic is described by an ideal diode model and subtracted a single exponential fitted to the part of the I-V curve before the peak and then extended it to the whole curve. The inset shows the result of this subtraction. Due to unintentional Zn diffusion [66] during the growth, which was not included in the initial design, the thickness of the intrinsic layer was reduced by 0.1 μm. This changed the internal field and moved the position of the expected resonance peak to 0.6-0.7 V (at room

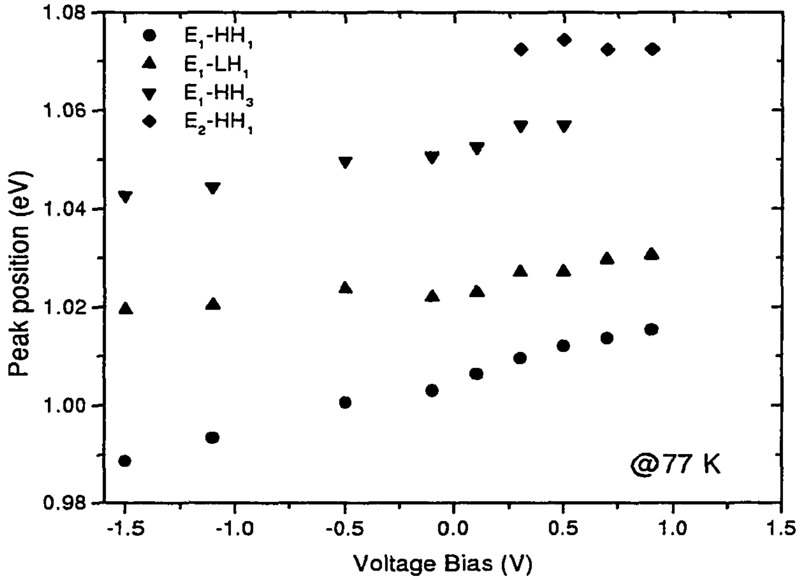

Figure 6.6: Photocurrent peak positions vs voltage bias for the InGaAsP/InP MQW sample at 77K.

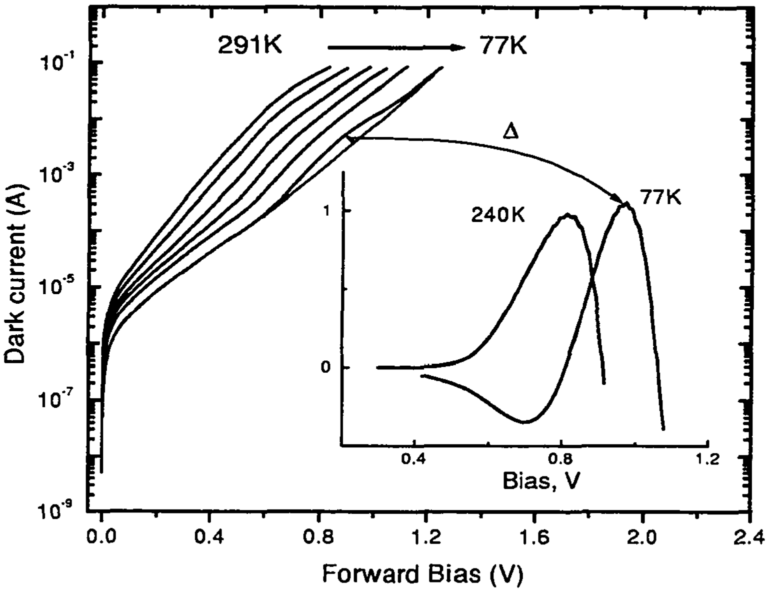

Figure 6.7: Temperature dependence of the dark current in the $In_{1-x}Ga_xAs_{1-y}P_y$/InP MQW sample. The plots were taken at $\Delta T \approx 20$ K intervals. The inset shows the 77 K curve after subtracting a fitted exponential background.

temperature).

Fig. 6.7 also shows that as temperature increases the position of the resonance peak shifts towards lower biases. This behavior can be understood if we replace V_{pv} in Eq. 6.1 with $[V_{pv} + (V_{bias} - V_x)]$, where V_{bias} is the total bias applied to the sample and V_x is the part of bias applied to the doped InP. An increase in temperature reduces both the device bandgap (and V_{bi}) and the resistance of the doped layers which causes V_x to decrease. The net result is a reduction of V_{bias} required to achieve a resonant condition, and consequently, a shift of the resonance peak towards lower bias. At room temperature the resonance peak becomes broader and weaker because of increased electron-phonon scattering and rising probability of thermionic emission.

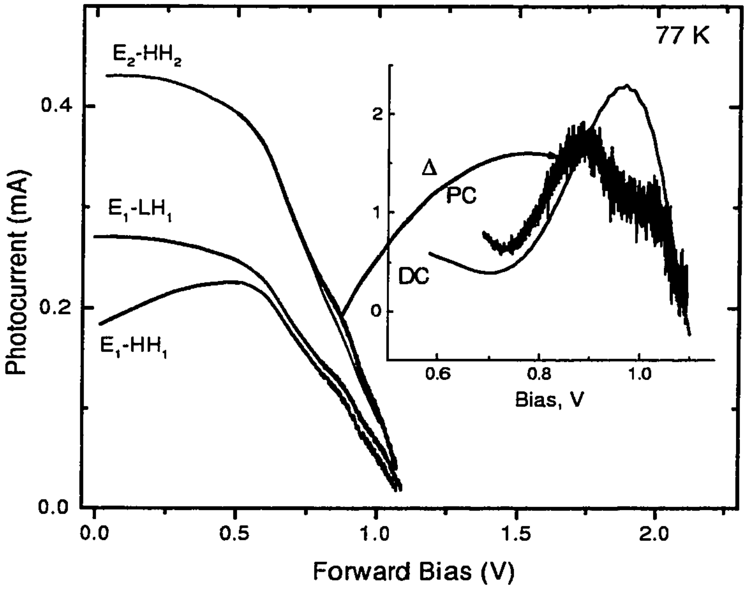

Figure 6.8: Bias dependence of the photocurrent at 77 K. The detection wavelengths were fixed at the $E_1 \rightarrow HH_1$, $E_1 \rightarrow LH_1$, and $E_2 \rightarrow HH_2$ transitions. The inset shows $E_1 \rightarrow HH_1$ curve after eliminating a linear background.

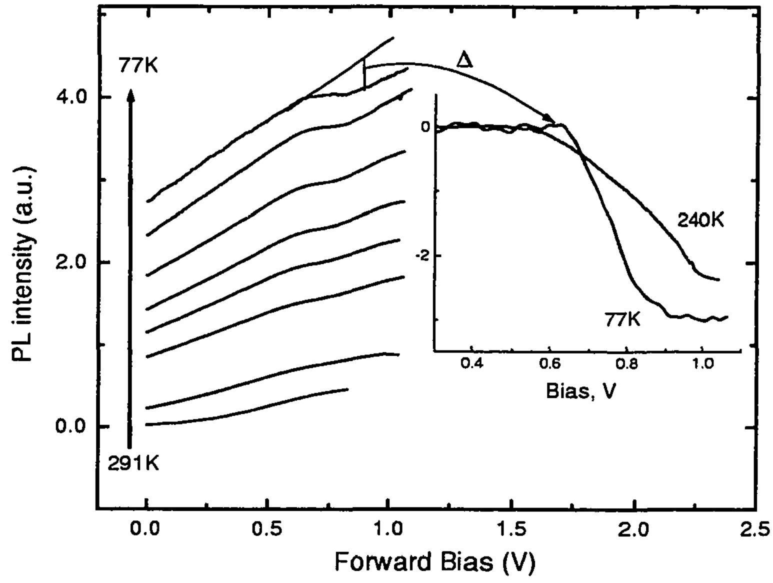

Figure 6.9: Temperature dependence of PL intensity vs. bias. For each PL(V) curve, the detection system was fixed at the PL maximum. The plots were taken at $\Delta T \approx$ 20 K intervals.

Photocurrent Figure 6.8 shows the photocurrent at 77 K versus bias measured at wavelengths corresponding to $E_1 \rightarrow HH_1$, $E_1 \rightarrow LH_1$, and $E_2 \rightarrow HH_2$ transitions. All curves demonstrate similar behavior: relatively flat to $\approx$ 0.6 V, and a rapid fall afterwards. The rising portion of the $E_1 \rightarrow HH_1$ curve is caused by the Stark effect, as the ground state is the most sensitive to field changes (see Fig. 6.6). The salient feature of all curves is a peak located at 0.9 V. The inset shows the $E_1 \rightarrow HH_1$ curve after removing a linear background, assumed for this region. We were not able to observe the photocurrent resonance peak at room temperature due to the high magnitude of the dark current at 0.7-0.9 V at this temperature.

Photoluminescence One of the most interesting experimental results for this sample was found in photoluminescence measurements. To determine if resonance tunneling had any effect on the radiative recombination rate we have measured the photoluminescence intensity as a function of applied bias as shown in Fig. 6.9. It can be seen that the PL intensity dips in the vicinity of the resonance peak $\approx$ 0.9 V, and that the amplitude of this dip diminishes with increasing temperature. Room temperature PL curve was cut short due to the same problem with rising dark current amplitude as it was with the photocurrent.

Temperature Dependence of Photocurrent As we saw in Chapter 5, the QW photocurrent ($I_{QW} = \int_{E_{QW}}^{E_{bat}} I_{pc}(E)dE$) dependence on the temperature can be used to identify the dominant escape mechanism. Fig. 6.10 shows the integrated quantum well PC as a function of temperature measured at several bias voltages. All curves present essentially the same behavior: slow decline towards high temperatures. This behavior is very different from what we have observed in InGaAsP strained MQW samples in Chapter 4 (Fig. 4.9), where the PC vs. T curves showed well defined maxima. The observed differences can be traced back to the differences in the structures. In Chapter 4 we were dealing with a shallow well system (0.9 eV well bandgap and 1.1 eV barrier bandgap), where the thermionic emission was a strong contributor to the whole escape process, and thus the photocurrent

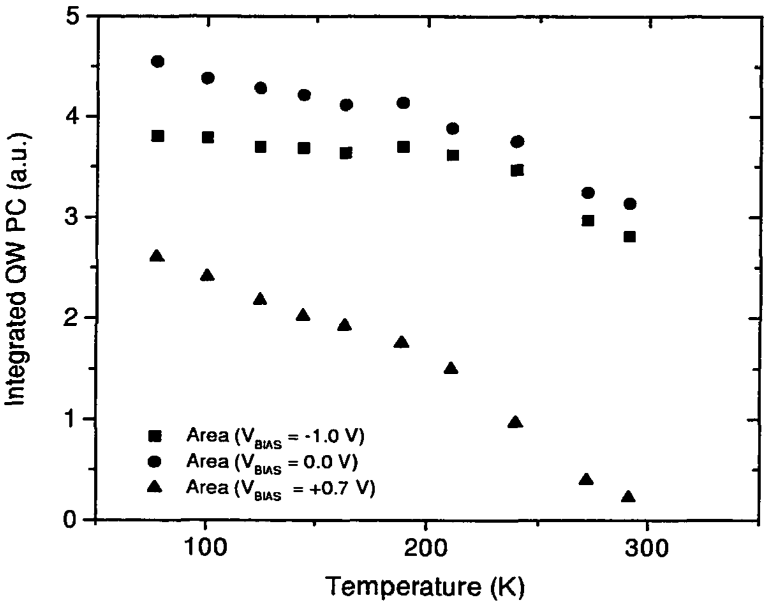

Figure 6.10: Integrated QW PC versus temperature measured at different biases.

intensity. Here we have a deeper well system with 0.9/1.35 eV well-to-barrier bandgap ratio, and the role of the thermionic emission is diminished. It is worth to note the effect of the bias on the curves. The negative and zero bias curves affected the least by the temperature, while the positive bias curve showed steeper decline. The possible explanation of the bias effect will be given in the Discussion section.

6.4.2 Electroreflectance Results

As we mentioned before, the electroreflectance spectroscopy allows us to extract a maximum value of the internal electric field F in the i-layer of p-i-n diode from the FKO oscillations. Fig. 6.11 shows F as a function of V_{bias} for both samples [67]. Both curves demonstrate linear field dependence which indicates ohmic contacts ($F = aV + b$), where $a_{MQW} = -25\ 10^3/cm$, $a_{ctrl} = -30\ 10^3/cm$, $b_{MQW} = -45\ kV/cm$, $b_{ctrl} = -40\ kV/cm$.

It should be noted that because of the nature of FKO (it depends on *free* carriers), no oscillations can be observed inside the MQW region. The FKO signal for the MQW sample originates in the undoped 500 Å InP buffer. As a result the field value is not the same as that for the control sample, where the signal comes from the whole undoped InP layer. A self-consistent Poisson's-diffusion calculation shows that due to the narrow *i*-InP layer of 500 Å there is a transfer of electrons from the *n*-InP into the nearest InGaAsP quantum well (QW), i.e., modulation doping. This results in an additional modulation doping field ($F_{mod} \approx$ 12 kV/cm) in the *i*-InP layer between the *n*-InP and the MQW stack. This field is similar to those that occur in the spacer layers of modulation-doped QWs due to the transfer of charge from the doping layers into the wells. The total field in this region is now $F_{tot} = 32\ kV/cm + 12\ kV/cm = 44\ kV/cm$, in good agreement with the experimental value.

6.4.3 SIMS Results

Figs. 6.12(a,b) and 6.13(a,b) are the SIMS data for both samples taken before ("a" curves) and after ("b" curves) metalization, respectively. The thick solid lines in Fig. 6.13 indicate the As distribution to denote placement of the MQW region while the thin solid and dashed lines in Fig. 6.13 denote the Zn and Si dopant profiles, respectively. Note that while there is some Zn in the intrinsic region for the MQW sample, both samples have approximately the same amount of unintentional Zn diffusion during growth. On the other hand, there is a pronounced difference in the Zn profiles for the control sample, such that the postmetallization sample having a smaller *i*-InP region.

6.5 Discussion

All our dark current, photocurrent and photoluminescence measurements confirm that sequential resonant tunneling does occur in our sample. Sequential resonant tunneling

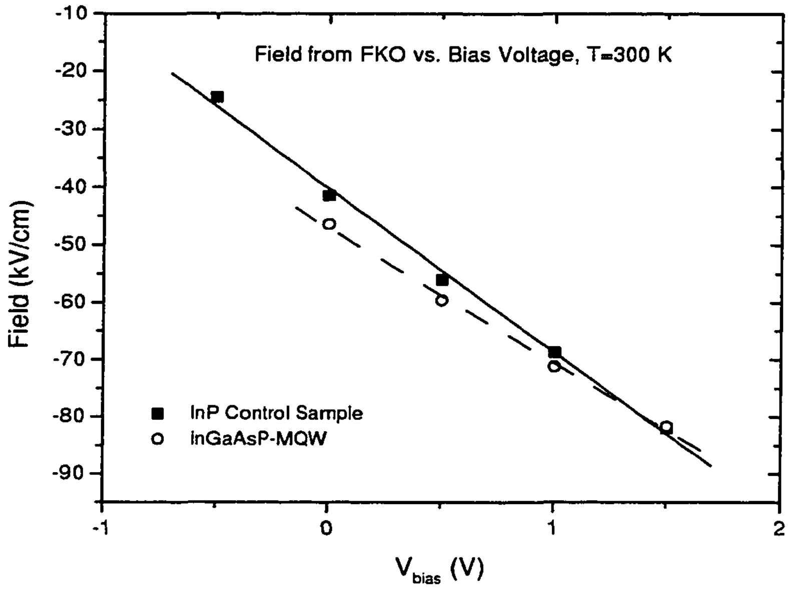

Figure 6.11: InP-related electric fields (from FKO) as a function of *dc* bias for control (squares) and MQW (circles) samples. Lines are fits to a linear function. Electric field is found to vary linearly with a slope coefficient of 30.

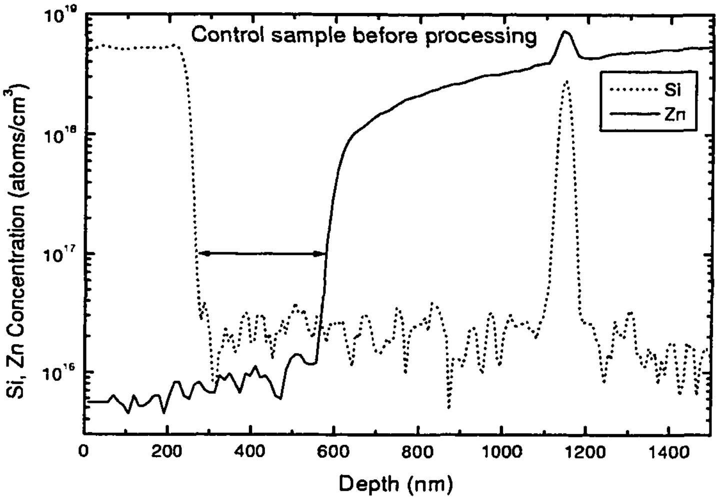

(a) Before metalization

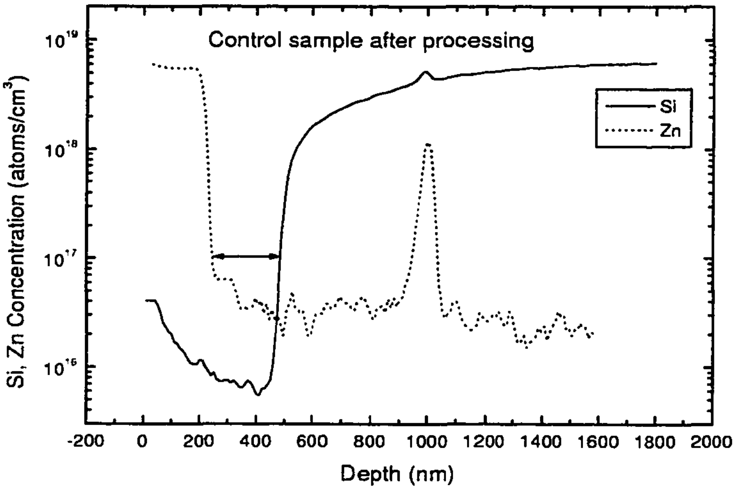

(b) After metalization

Figure 6.12: SIMS profiles of the InP control sample.

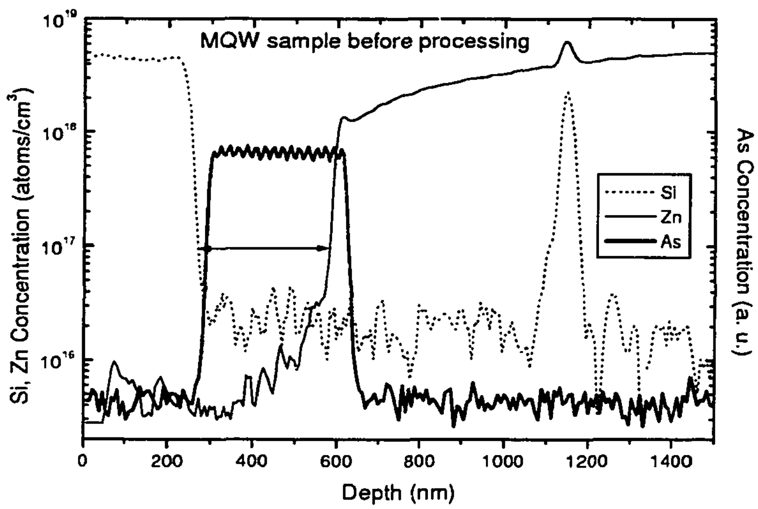

(a) Before metalization

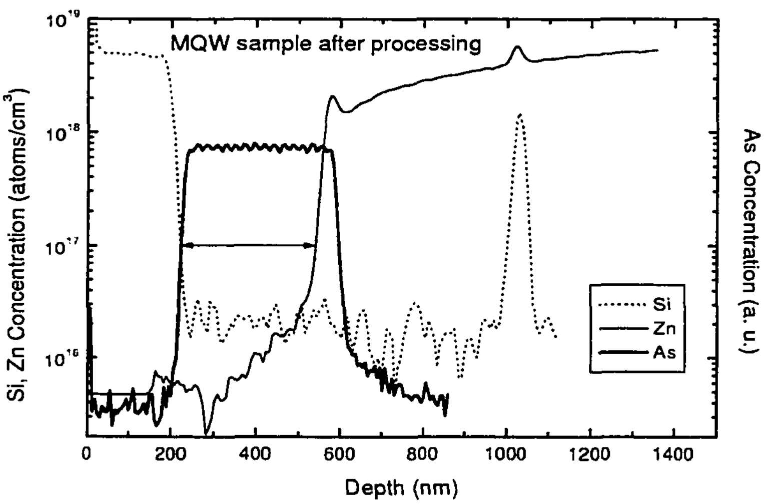

(b) After metalization

Figure 6.13: SIMS profiles of the InGaAsP/InP MQW sample.

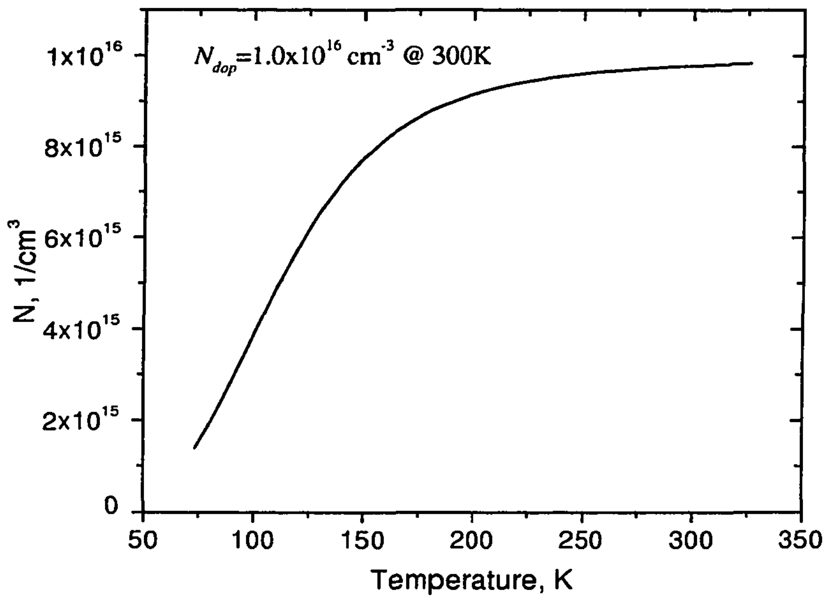

Figure 6.14: Calculated concentration of ionized impurity atoms (Zn) in InP as a function of temperature. Activation energy $E_{ac} = 46$ meV

enhances the photocarrier collection and reduces radiative recombination losses.

However several factors have led to the situation where the SRT effect was present only at low temperatures, and the resonance itself occurred at V_{bias} which was outside the operational range of the cell (The operational range of the solar cell is from 0 to V_{oc}).

To explain the temperature dependence of the SRT we have to recall that *i*-region is lightly p-doped. A number of ionized acceptor atoms depends on the temperature as

$$N_{acc}^{-} = \frac{N_{acc}^{0}}{1 + g\exp[(E_{ac} - E_f)/k_B T]} \tag{6.5}$$

where N_{acc}^0 is the total concentration of acceptor atoms, g the degree of degeneracy of acceptor level, and E_{ac} is the so-called *activation* energy, which in the case of Zn in InP it is ≈0.046 eV.

Fig. 6.14 shows calculated concentration of ionized acceptor atoms as a function of temperature. Room temperature concentration was chosen to be $1 \times 10^{16}\ cm^{-3}$ as it was measured by Dr. C.L. Reynolds' group. It can be seen that at 77 K the concentration is reduced by factor of 10 compared to the concentration at room temperature. The effect of reduced concentration of ionized impurities on the band edges and the field distribution of the MQW structures is shown in Figs. 6.15 and 6.16. Band diagrams and field distribution were calculated using the Poisson solver program described in Sec. 2.5.

Fig. 6.15 shows that at $1 \times 10^{16}\ cm^{-3}$ all wells inside MQW layer *can not* be aligned perfectly. That means the condition for resonant transfer exists only in selected areas of this layer, which reduces the effect of the SRT on carrier collection. The fact that "resonance" bias is different for different areas broadens the SRT peak in current-voltage characteristic and reduces its amplitude. Fig. 6.16 shows that at $1 \times 10^{15}\ cm^{-3}$ (dotted curve) the variation in the field value does not exceed 20% of the average field 30 kV/cm. For a superlattice with a 200Å period this means the deviation of $1\ meV = (200Å) \times (0.2 \cdot 30\ kV/cm)$ from a resonance value. This is acceptable because typical FWHM for quantum well levels is of the order several meV.

6.6 Conclusion

All our dark current, photocurrent and photoluminescence measurements confirmed that sequential resonant tunneling did occur in our MQW sample. Sequential resonant tunneling transfer enhanced the photocarrier collection and reduced radiative recombination losses. That is the most significant result of the this investigation.

From these results we have also drawn conclusions which can lead to an improved design of MQW devices with SRT. The SRT increases *both* photocurrent I_{ph} and dark current I_{dc}. The total current of a photovoltaic device is the difference of these two currents ($I_{tot} = I_{ph} - I_{dc}$), and thus, to take advantage of the SRT, the MQW solar cell should be

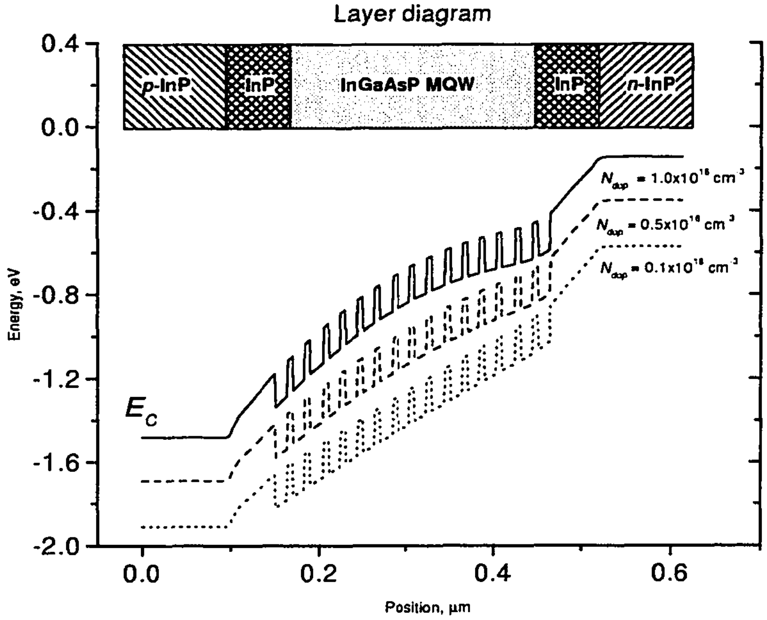

Figure 6.15: Calculated band diagram of the MQW InGaAsP/InP sample at different concentration of ionized impurity atoms inside the intrinsic layer.

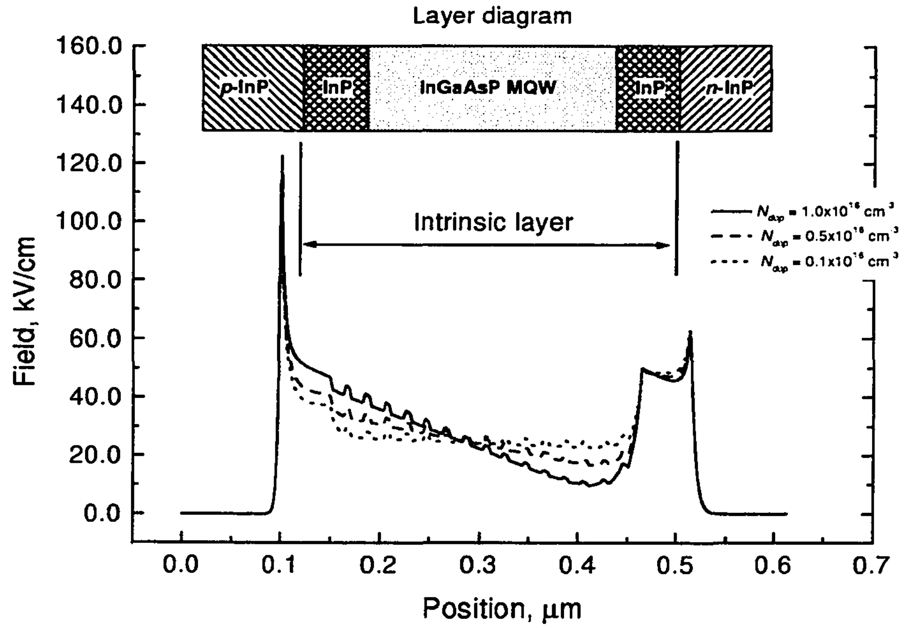

Figure 6.16: Calculated field distribution inside the intrinsic layer of the MQW InGaAsP/InP sample at different concentration of ionized impurity atoms.

designed to have the resonance in the region where $I_{ph} >> I_{dc}$.

Our experiments with different MQW samples showed that built-in resonant alignment is more beneficial for deeper wells where carrier escape rates associated with thermally activated mechanisms (thermionic emission and phonon-assisted tunneling) are lower than that in our sample.

Carrier extraction from the MQW layer is another issue to be addressed more carefully. From Fig. 6.2 it is clear that the bottleneck of electron transfer is the last (N-th) well, where carriers face a significantly thicker right barrier than inside the MQW region. This can lead to charge build-up and screening of the built-in field. To avoid this we suggest that a layer of InGaAsP with a bandgap intermediate between that of the well's and InP be inserted between the N-th well and n-InP.

6.6.1 Criteria for Successful Implementation of the SRT in MQW Solar Cell

Based on these studies we have established a few conditions for the SRT in MQW solar cell devices. Below is the summary of what we believe can be used as guidelines to the successful integration of the sequential resonant tunneling transfer in photovoltaic devices.

- Use of the SRT transfer in MQW solar cells is better suited for deep-well systems (with well/barrier difference more than 0.5 eV), where the thermionic emission escape rate is substantially lower than the tunneling rate.
- Low residual dopant concentration in the i-layer of the p-i-n diode is a very important element. It provides a uniform field distribution across that region. Our estimates show that 1×10^{15} cm^{-3} for 0.5 μ-thick intrinsic layer is a sufficient value.
- The "resonant" value of the bias has to be carefully chosen. It *should* be within operational range of the designed cell.

Chapter 7

Conclusion

7.1 Thesis summary

The main topic of this thesis was the physics of carrier transport and photovoltaic conversion in InP-based multiple quantum well and bulk heterostructures. A new concept of enhancing MQW solar cell conversion efficiency using sequential resonant tunneling transfer was introduced. To verify this idea MQW InGaAsP/In solar cells were designed, grown and investigated. Sample characterization was conducted using a wide set of techniques: photoluminescence and photocurrent measurements, current-voltage measurements, electroreflectance[1] and SIMS[2]. Most PL, I-V and PC data were studied for their temperature and bias dependence. Enhancement of the photocurrent in an InGaAsP/InP MQW heterostructure due to built-in SRT has been observed for the first time. Photovoltaic efficiency measurements showed that the MQW solar cells made from one wafer, on average, outperformed the control non-MQW cells by 13% (relative efficiency of the control sample taken as 100%; absolute efficiencies of 2.68 and 3.02 % for the control and MQW samples, respectively). The effect of the SRT on performance was relatively small because of (1) the small magnitude of the SRT peak and (2) the location of the peak was out of the operational

---

[1] exp. data by Dr. A. Jaeger

[2] exp. data by Dr. M. Geva

range of the cell. Based on the obtained results the criteria for successful implementation of SRT in MQW structures for the purpose of enhancement of photovoltaic efficiency have been established. The main requirements are low residual dopant concentration in the *i*-layer (less than 1×10^{15} cm^{-3}) and careful choice of the "resonant" value of the bias, which must be within operational range of the designed cell.

In addition, a separate set of InGaAsP MQW samples with the same well thickness and different barrier widths was investigated using photoluminescence, photocurrent and dark current measurements. The focus of the study was the basic properties of the MQW structures: quantum well energy states, the effect of the strain, temperature and electric field on these states, and the escape processes in quantum wells. The origin of recombination losses was analyzed. The relation of the quantum well electronic properties with structural and compositional parameters of heterostructures was also a subject of investigation as it is important for an understanding of the basic physics in MQW devices.

7.2 Future developments in Photovoltaics

In this section we briefly review new ideas and developments in photovoltaics not necessarily limited to MQW devices only which can potentially lead to high performance solar cells.

7.2.1 Issues to be addressed

Our investigation has raised several questions which need to be addressed in future studies.

One of the problems we found in our samples is that at room temperature the SRT effect practically disappears and has no significant influence on carrier collection. It is important to investigate the temperature dependence of the SRT in several different MQW samples, to find out what limits the SRT: phonon-electron interactions, structural defects

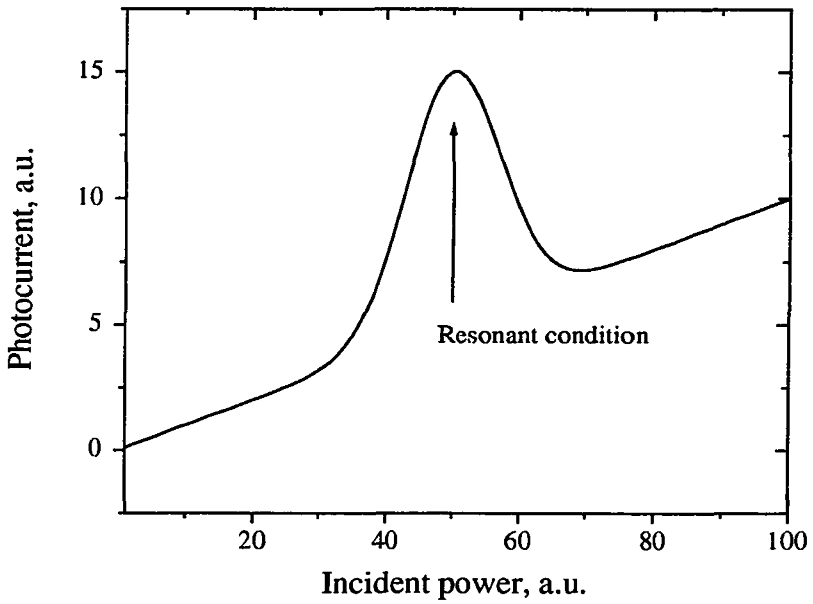

Figure 7.1: Response characteristic of the proposed SRT electro-optical modulator. The peak in the current corresponds to the situation when the incident light power is exactly the one needed to put the device in resonant condition (causes the wells to be "resonantly" aligned).

or something else.

Another very interesting topic is the excitation intensity dependence of the SRT. Different excitation light intensity creates different carrier density inside the MQW layer, which, in turn, will change the field distribution. This will have the same effect as applying an external voltage bias to the sample. In principle, one could make an electro-optical modulator with the I-P (current-intensity) characteristic shown in Fig. 7.1. As soon as the carrier density reaches the value which causes resonant alignment of the wells, the device will switch into a "resonant" mode producing the peak in the response characteristic. The peak in the current corresponds to the situation when the incident light power is exactly the one needed to put the device in resonant condition.

7.2.2 MQW Solar Cells

Recent developments in MQW solar cell research suggest that the main obstacles which prevent MQW solar cells from reaching their predicted efficiency values are quality of material and unoptimized cell structure. One of the quality problems is an unwanted diffusion of dopant material, especially in InP based MQW devices. Optimization of the structure should include modeling of the spectral response and dark current in the device, finding the combination of cell parameters (layer thickness, doping concentration and profile, well and barrier widths etc.) which can provide the best performance. These problems can be solved with time.

In our model of an ideal MQW solar cell, the efficiency of a two-component MQW solar cell can exceed the efficiency of a comparable single-band solar cell by only 15-20 %. Economically it may not be justifiable to grow complex MQW structures in order to get a rather marginal increase in efficiency.

A substantial increase in the efficiency requires extending the spectrum coverage to the UV and IR parts of the solar spectrum, to 400 and 2000 nm, respectively. At the present time, a very promising combination of II-VI and III-V group semiconductor heterostructures has been reported by M. Tamargo's group [68] at CCNY. The II-VI/III-V structure will produce a wider range of band gaps and utilize, correspondingly, a broader part of the solar spectrum. InP- based devices have been shown to be important host material for fabricating infrared photodetectors and lasers used in fiber optics communications. InP solar cells have also demonstrated increased radiation resistance, which is an important issue for extraterrestrial applications. The II-VI group wide bandgap semiconductors are a very promising material for the visible and UV applications. The combination of III-V structure (InP/InGaAs or InP/InGaAsP) with a wide-band II-IV structure (ZnCdMgSe/ZnCdSe) appears to be a suitable choice for a multiple band gap MQW solar cell. All layers can be grown lattice-matched to the InP substrate. *This combination will effectively cover very wide energy range from 0.75 eV for InGaAs to 2.8-3.0 eV for ZnCdMgSe.* This is a much wider range than the range covered by the record holding tandem GaInP/GaAs solar cell [69] (E_g^{GaInP} = 1.8 eV, E_g^{GaAs} = 1.42 eV).

Quantum Well Solar Cell for Thermophotovoltaics

Thermophotovoltaic (TPV) power generation produces electricity converting radiation from various heat sources. TPV recently became a hot topic due to advances in low bandgap cells and selective emitters [70]. Selective emitters such as rare earth oxides ytterbia and erbia are often used to convert broad band radiation of the heat source to the narrow band emission. The re-emitted radiation may be efficiently converted to electric power using a photovoltaic cell of the matching bandgap. Low bandgaps are required since the source temperature is in the range of 800-2000 K.

Semiconductors such as Ge, Si and GaSb were proposed but their fixed bandgaps make it difficult to match the heat source spectra. The bandgap of InGaAs can be changed; however, strain relaxation effects severely degrade cell performance causing a reduction in the output voltage. The quaternary alloy InGaAsP lattice-matched to the InP substrate is a very promising candidate for TPV applications; it is free of the strain problems and the effective bandgap can be tuned by varying composition and well width up to 1.64 μm.

Griffin *et al.* [71] reported on a large enhancement in output voltage of the InGaAsP QWSC compared to a similar control cell made from the well material. Another advantage of the TPV QWSC is their superior temperature efficiency coefficients; this lower sensitivity to the heat makes them very attractive in the hot environment applications.

7.2.3 Graded Band-Gap Solar Cell

An interesting idea of using *a graded bandgap* in solar cells was proposed by Dhingra and Rothwarf [72]. The graded gap semiconductor can be made by continuously changing composition of the ternary or quaternary alloy (e.g. x in $Al_xGa_{1-x}As$). This kind of heterostructure may have an advantage over step-like heterointerfaces, for example, higher

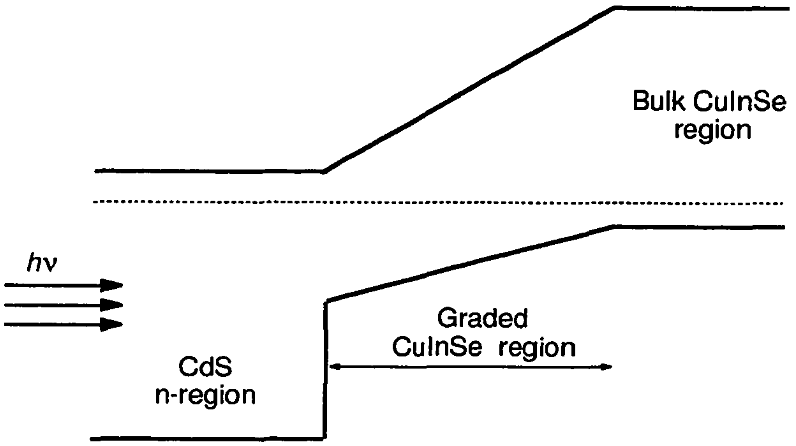

Figure 7.2: *p-i-n* $CuInSe_2$/CdS solar cell structure with graded bandgap *i*-layer.

mobility due to the lack of interface scattering. The *p-i-n* $CuInSe_2$/CdS-based solar cell structure with graded intrinsic layer is shown in Fig. 7.2. According to the authors, proper application of graded-composition semiconductors in the fabrication of a solar cell can potentially increase their power conversion efficiency both through a photovoltaic effect and through increased collection of photo-generated minority carriers in the graded region. A graded bandgap region creates a so-called *quasi-electric field* [73], a field defined as the gradient of the band edge. In a nonuniform semiconductor, the gradient of the conduction band need not be the same as that of the valence band. Therefore, the quasi-electric field which acts upon electrons can be different from the quasi-electric field that acts upon holes. This property can be used to improve carrier collection.

A graded bandgap absorber can improve cell efficiency in the following three ways:

1. Adjust the SRH recombination (see Sec.2.2.7) profile in the depletion/intrinsic layer. Tailor the recombination region to minimize recombination and thus achieve higher open-circuit voltages.
2. Improve the collection efficiency through suitably directed quasi-electric fields acting on electrons and holes.

3. Localize regions of high and low absorption. Confine the incident light in the intrinsic region to achieve higher absorption efficiency.

Dhingra and Rothwarf had conducted a computer simulation of a graded bandgap $CuInSe_2/CdS$ solar cell. They had found that an optimally graded structure with grading between 1.5 eV and 1.3 eV resulted in a conversion efficiency of 17.9% compared to 14.9% of a similar cell with a uniform bandgap.

7.2.4 Solar Cell with Internal Quantum Efficiency > 1

Recently accurate measurements [74] have shown quantum efficiencies higher than 1 in the short-wavelength range which was associated with Auger effect. In the Auger process the energy in excess of the band gap that one of the carriers receives from a high-energy photon is used in a second electron-hole generation.

This has led to a revision of the widely accepted model of the ideal solar cell, where it is assumed that every absorbed photon in a solar cell produces at most *one* electron-hole pair. This assumption has led to an estimated maximum efficiency of about 31% for an ideal semiconductor with energy gap of $E_{gap} = 1.26$ eV [75]. In the revised theory of the ideal solar cell, Werner, Kolodinski and Queisser (WKQ) have found that a thermodynamical limit for a single gap solar cell would increase from 31% to 43% for the absolute conversion efficiency if solar photons were to generate multiple electron-hole pairs whenever energetically possible.

One of the proposed realizations of a mechanism for multiple pair generation is carrier multiplication by impact ionization induced from hot carriers. The same authors (WKQ) [76] later have quantitatively investigated carrier multiplication in the $Si_{1-X}Ge_X$ material system. Their conclusion was that only a small relative increase of solar cell efficiency ($\approx 0.5\%$) may be expected from impact ionization of hot carriers. The competing process of phonon emission restricts the absolute efficiency enhancement. The effective use of impact ionization in solar cells requires a strong reduction of the phonon emission probability in

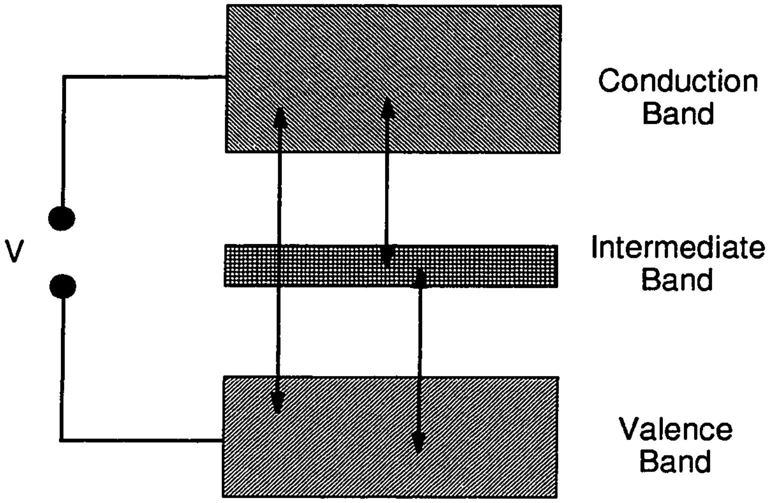

Figure 7.3: Band diagram of a solar cell structure with an intermediate band. Arrows denote possible transitions between bands.

future material systems.

7.2.5 Solar Cell with Intermediate Bandgap

Recently several groups [77,78] have investigated the possibility to increase the efficiency of solar cells by introducing an impurity energy level in the semiconductor band gap that absorbs additional lower energy photons. Luque and Martí [79] have analyzed such a structure shown in Fig. 7.3. They found that such cell has an efficiency limit higher than the ideal two band (no intermediate band) solar cell if the intermediate band gap is radiatively connected with the two bands: conduction and valence.

Appendix A

Transfer Matrix Method

The method is used to calculate the transmission probability $T(E)$ of electron wave through the potential barrier of arbitrary shape. The following simplifications are assumed:

- The electrons are considered as *free carriers* with isotropic effective mass m^*.
- There is no inelastic scattering.
- The Coulomb interaction between electrons is neglected.

With these assumptions three dimensional problem can be reduced to one-dimensional. Let the growth axis be in z direction.

$$\left[-\frac{\hbar^2}{2m^*}+V(z)\right]\psi(z)=E_z\psi(z) \tag{A.1}$$

where E_z is z component of the total electron energy and $\psi(z)$ is an electron wave function.

Let us discuss a case of double barrier structure shown in Fig. A.1. $V(z)$ can be divided into $n+1$ regions such that in each j-layer the potential V_j is assumed to be constant. In each i region the electron wave $\psi(z)$ is sought as a sum of the incident and reflected plane waves:

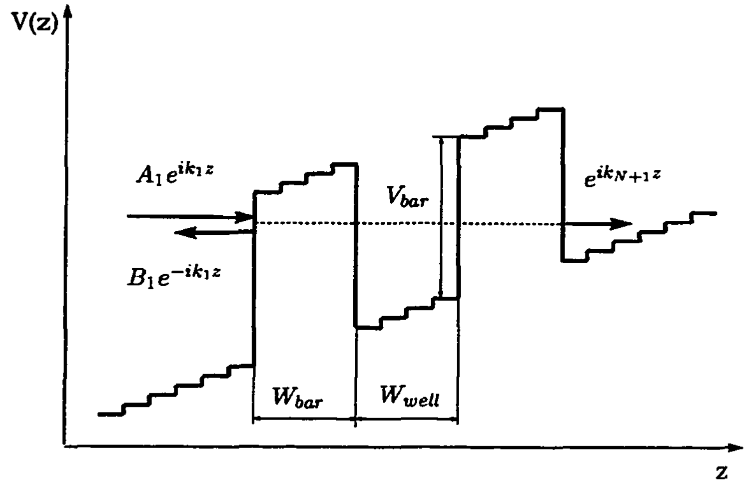

Figure A.1: Piecewise potential used to calculate quantum well eigenstates and eigenfunctions. V_{bar} - barrier height, W_{well} - well width, W_{bar} - barrier width.

$$\psi(z) = A_j(z)e^{ik_j z} + B_j(z)e^{-ik_j z} \tag{A.2}$$

where $k_j = \sqrt{2m_j^*(E_z - V_j)/\hbar^2}$ and m_j^* are, respectively, the wavevector and effective mass in the region i. From A.2 it is clear that k_j is real or imaginary depending on whether $V_j < E_z$ or $V_j > E_z$. Inside the barriers k_j is a pure imaginary and it represents *evanescent* wave. The A_j and B_j coefficients are found from the requirement of continuity of both the wavefunction and the probability flux. At a $z = z_j$ step it can be written as:

$$A_{j-1}e^{ik_{j-1}z_{j-1}} + B_{j-1}e^{-ik_{j-1}z_{j-1}} = A_j e^{ik_j z_j} + B_j e^{-ik_j z_j} \tag{A.3a}$$

$$\frac{ik_{j-1}}{m_{j-1}}(A_{j-1}e^{ik_{j-1}z_{j-1}} - B_{j-1}e^{-ik_{j-1}z_{j-1}}) = \frac{ik_j}{m_j}(A_j e^{ik_j z_j} - B_j e^{-ik_j z_j}) \tag{A.3b}$$

$$|A_j|^2 + |B_j|^2 = 1 \quad \text{for each } j = 1, 2, \ldots, N+1 \tag{A.3c}$$

The coefficients (A_1, B_1) and (A_{N+1}, B_{N+1}) are related by:

$$\begin{pmatrix} A_1 \\ B_1 \end{pmatrix} = M_1 \otimes M_2 \otimes \ldots \otimes M_N \begin{pmatrix} A_{N+1} \\ B_{N+1} \end{pmatrix} \tag{A.4}$$

where the matrix elements $M_j^{\alpha\beta}$, $\alpha, \beta = 1$ or 2 are given by:

$$M_j^{11} = \left(\frac{1}{2} + \frac{k_{j+1}m_j^*}{2k_j m_{j+1}^*}\right) e^{i(k_{j+1}-k_j)z_j} \tag{A.5a}$$

$$M_j^{12} = \left(\frac{1}{2} - \frac{k_{j+1}m_j^*}{2k_j m_{j+1}^*}\right) e^{-i(k_{j+1}+k_j)z_j} \tag{A.5b}$$

$$M_j^{21} = \left(\frac{1}{2} - \frac{k_{j+1}m_j^*}{2k_j m_{j+1}^*}\right) e^{i(k_{j+1}-k_j)z_j} \tag{A.5c}$$

$$M_j^{22} = \left(\frac{1}{2} + \frac{k_{j+1}m_j^*}{2k_j m_{j+1}^*}\right) e^{-i(k_{j+1}+k_j)z_j} \tag{A.5d}$$

The wave is considered to be coming from the left side of the structure, so there is no reflected wave on the right side. Then from Eq. A.3c $(A_{N+1}, B_{N+1}) = (1, 0)$ and the transmission coefficient can be obtained from:

$$T(E_z) = \left|\frac{A_{N+1}}{A_1}\right|^2 \tag{A.6}$$

The Fig. A.2 shows calculated transmission probability for the InGaAsP/InP double barrier heterostructure with following parameters: well depth – 140 Å; barrier width – 60 Å, well depth – 170 eV, internal electric filed – 20 kV/cm, electron mass inside the well and barriers – $0.056m_0$ and $0.079m_0$. The maxima of the $T(E)$ occur at the resonance energy $E = E_n$, corresponding to the bound eigenstate n.

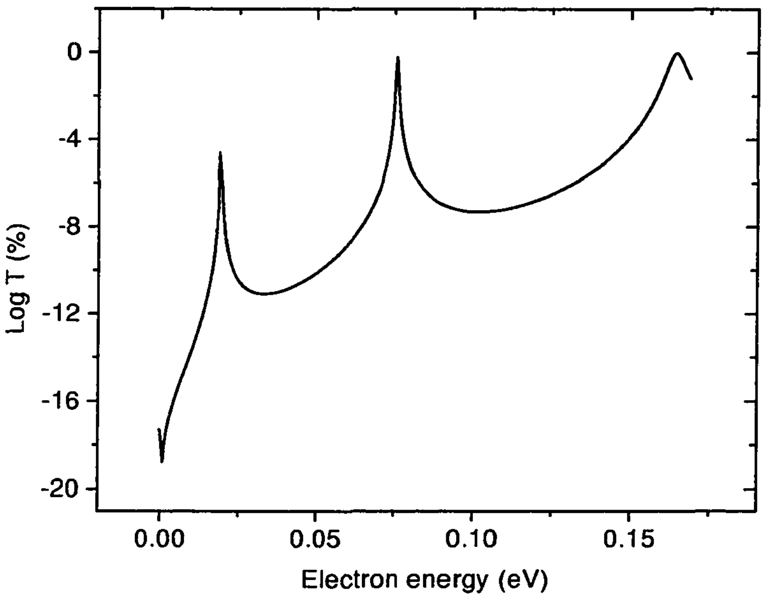

Figure A.2: Logarithmic plot of the calculated transmission coefficient for the InGaAsP/InP double barrier heterostructure.

Appendix B

"Ke236" – a program to control Triax 320, Keithley 236 and SR830

To control the experiment we have written software (*Ke236*) using National Instruments® LabWindows/CVI IDE [49] (Integrated Development Environment). Full C code of the program *Ke236* is provided on the accompanying floppy disk due to its large printed size (about 120 pages). Fig. 3.2 shows a flowchart of the program. The program provides remote control over most of the functions of the spectrometer, the lock-in amplifier and the SMU unit.

Using this program the following types of measurements can be made:

- Current-voltage measurements
- Photoluminescence intensity as a function of wavelength
- Photoluminescence intensity as a function of bias
- Photocurrent intensity as a function of wavelength
- Photocurrent intensity as a function of bias
- Solar cell performance measurements

Device	GPIB Address
Keithley 236 SMU	10
TRIAX 320 Spectrograph	2
SR830 Lock-In	5

Table B.1: A list of GPIB-controlled devices used by the "Ke236.exe" and their addresses

The program code is provided on the accompanied floppy disk and does not include the files (however, necessary for successful compilation of the "ke236") written and copyrighted by National Instruments® Corporation and other vendors. The featured code has to be compiled from inside National Instruments LabWindows® Integrated Development Environment (IDE) version 4.0 or higher. When run, the executable file checks for the presence of a GPIB interface card and exits if no card is found. The following GPIB addresses are hard-coded inside the program and must be set before the run.

Bibliography

[1] L. Esaki and R. Tsu, IBM J. Res. Dev. **14**, 61 (1970).

[2] L. L. Chang, L. Esaki, and R. Tsu, Appl. Phys. Lett. **24**, 593 (1974).

[3] J. M. Woodall, Science **208**, 908 (1980).

[4] F. Capasso, Science **235**, 172 (1987).

[5] C. H. Henry, J. Appl. Phys. **51**, 4494 (1980).

[6] K. W. J. Barnham and G. Duggan, J. Appl. Phys. **67**, 3490 (1990).

[7] K. W. J. Barnham, B. Braun, J. Nelson, M. Paxman, C. Button, J. S. Roberts, and C. T. Foxon, Appl. Phys. Lett. **59**, 135 (1991).

[8] A. Freundlich, A. Bensaoula, and N. Medelci, in *Proceedings of the 1st World Conference on Photovoltaic Energy Conversion* (IEEE, New York, 1994), Vol. 2, pp. 1886–1889.

[9] N. G. Anderson and S. J. Wojtczuk, J. Appl. Phys. **79**, 1973 (1996).

[10] M. Paxman, J. Nelson, B. Braun, J. Connoly, K. W. J. Barnham, C. T. Foxon, and J. C. Roberts, J. Appl. Phys. **74**, 614 (1993).

[11] J. M. Mohaidat, K. Shum, W. B. Wang, and R. R. Alfano, J. Appl. Phys. **76**, 5533 (1994).

[12] J. Nelson, M. Paxman, K. W. J. Barnham, J. C. Roberts, and C. Button, IEEE J. of Quantum Electronics **29**, 1460 (1993).

[13] I. Ballard, K. W. J. Barnham, J. Nelson, J. P. Connoly, C. Roberts, J. S. Roberts, and M. A. Pate, in *Proceedings of the 2th World Conference and Exhibition on Photovoltaic Solar Energy Conversion* (Stephen, Vienna, 1998).

[14] A. F. M. Anwar and K. R. Lefebvre, Phys. Rev. B **57**, 4584 (1998).

[15] F. Capasso, K. Mohammed, and A. Y. Cho, Appl. Phys. Lett. **48**, 478 (1986).

[16] F. Capasso, K. Mohammed, A. Y. Cho, R. Hull, and A. L. Hutchinson, Appl. Phys. Lett. **47**, 420 (1985).

[17] H. Schneider, J. Wagner, and K. Ploog, Solid State Electronics **37**, 881 (1994).

[18] C. J. Summers, K. F. Brennan, A. Torabi, and H. M. Harris, Appl. Phys. Lett. **52**, 132 (1987).

[19] R. R. Alfano, in *Semiconductors Probed by Ultrafast Laser Spectroscopy* (Academic Press, Orlando, Florida, 1984), pp. xi–xiii.

[20] D. Y. Oberli, D. R. Wake, M. V. Klein, J. Klem, T. Henderson, and M. Morkoç, Phys. Rev. Lett. **59**, 696 (1987).

[21] D. Y. Oberli, J. Shah, T. C. Damen, C. W. Tu, T. Y. Chang, D. A. B. Miller, J. H. Henry, R. F. Kopf, N. Sauer, and A. E. DiGiovanni, Phys. Rev. B **40**, 3028 (1989).

[22] G. Livescu, A. M. Fox, D. A. B. Miller, T. Sizer, W. H. Knox, A. C. Gossard, and J. H. Engilsh, Phys. Rev. Lett. **63**, 438 (1989).

[23] K. Leo, J. Shah, J. P. Gordon, T. C. Damen, D. A. B. Miller, C. W. Tu, and J. E. Cunningham, Phys. Rev. B **42**, 7065 (1990).

[24] L. Landau and I. M. Lifshitz, *Nonrelativistic Quantum Mechanics* (Addison-Wesley, Reading, 1958).

[25] E. O. Kane, J. Phys. Chem. Sol. **1**, 249 (1957).

[26] G. Bastard, *Wave Mechanics Applied to Semiconductor Heterostructures* (Les Editions de Physique, France, 1986).

[27] R. Q. Yang, J. M. Xu, and M. Sweeny, Phys. Rev. B **50**, 7474 (19944).

[28] F. H. Pollak and M. Cardona, Phys. Rev. **172**, 816 (1968).

[29] H. Schneider and K. v. Klitzing, Phys. Rev. B **38**, 6160 (1988).

[30] A. Larsson, P. A. Andrekson, S. T. Eng, , and A. Yariv, IEEE J. of Quantum Electronics **24**, 787 (1988).

[31] H. J. Möller, *Semiconductors for Solar Cell* (Artech House, Boston, 1993), pp. 28–31.

[32] P. Yu and M. Cardona, *Fundamentals of Semiconductors* (Springer-Verlag, Berlin, 1996).

[33] W. Müller, H. T. Grahn, R. J. Haug, and K. Ploog, Phys. Rev. B **46**, 9800 (1992).

[34] L. Thibaudeau, P. Bois, and J. Y. Duboz, J. Appl. Phys. **79**, 446 (1996).

[35] R. F. Kazarinov and R. A. Suris, Sov. Phys. Semicond **6**, 707 (1972).

[36] L. Esaki and L. L. Chang, Phys. Rev. Lett. **33**, 495 (1974).

[37] C. J. Summers and K. F. Brennan, Appl. Phys. Lett. **48**, 806 (1986).

[38] S. K. Lyo, Phys. Rev. B **34**, 7129 (1986).

[39] M. Dür, S. M. Goodnick, and P. Lugli, Phys. Rev. B **54**, 17794 (1996).

[40] G. L. Araújo and A. Martí, Sol. Energy Mater. Solar Cells **33**, 213 (1994).

[41] K. W. J. Barnham, I. Ballard, J. Barnes, J. Connoly, P. Griffin, B. Kluftinger, J. Nelson, E. Tsui, and A. Zachariou, Appl. Surf. Sci. **113/114**, 722 (1997).

[42] K. W. J. Barnham, J. Connoly, P. Griffin, G. Haarpainter, J. Nelson, E. Tsui, A. Zachariou, J. Osborne, c.button, G. Hill, M. Hopkinson, M. Pate, and J. Roberts, J. Appl. Phys. **80**, 1201 (1996).

[43] N. G. Anderson, J. Appl. Phys. **78**, 1850 (1995).

[44] M. S. Lundstrom and R. J. Schuelke, IEEE Trans. Electron. Devices **ED-30**, 1151 (1983).

[45] W. H. Press, S. A. Teukolsky, W. T. Vetterling, and B. P. Flannery, *Numerical Recipes in C: The Art of Scientific Computing* (Cambridge University Press, Boston, Massachusetts, 1993).

[46] *Spectrometer Control, INTERFACING & PROGRAMMING MANUAL*, Instruments S.A., Inc, Edison, New Jersey, USA, 1997.

[47] *Model 236 Source Measure Unit Operator's Manual*, fourth ed., Keithley Instruments, Inc., Cleveland, Ohio, USA, 1989.

[48] *Model SR830 DSP Lock-In Amplifier*, 1.4 ed., Stanford Research Systems, Sunnyvale, California, USA, 1993.

[49] *LabWindows/CVI (C for Virtual Instrumentation) Documentation*, 4.0.1 ed., National Instruments Corp, Austin, Texas, USA, 1996.

[50] *Model 1835-C Multi-Function Optical Meter Manual*, Newport Corporation, Irvine, California, USA, 1993.

[51] O. Y. Raisky, W. B. Wang, R. R. Alfano, C. L. Reynolds Jr., and V. Swaminathan, J. Appl. Phys. **81**, 394 (1997).

[52] O. Y. Raisky, W. B. Wang, R. R. Alfano, C. L. Reynolds Jr., and V. Swaminathan, in *Proceedings of the 9th International Conference on Hot Carriers in Semiconductors* (Plenum Press, New York, 1997), pp. 11–13.

[53] Y. P. Varshni, Physica **34**, 149 (1967).

[54] H. Temkin, D. Gershoni, and M. B. Panish, in *Epitaxial Microstructures* (Academic Press, New York, 1994), Chap. Optical properties of GaInAs/InP quantum wells.

[55] S. Marcinkevičius, U. Olin, and G. Treideris, J. Appl. Phys. **74**, 3587 (1993).

[56] D. Gershoni, C. H. Henry, and G. A. Baraff, IEEE J. Quantum Electron. **29**, 2433 (1993).

[57] O. Y. Raisky, W. B. Wang, R. R. Alfano, C. L. Reynolds Jr., D. V. Stampone, and M. W. Focht, J. Appl. Phys. **84**, 5790 (1998).

[58] D. J. Flood and I. Weinberg, Optoelectronics - Devices and Technologies **9**, 451 (1994).

[59] A. Zachariou, K. W. J. Barnham, P. Griffin, J. Nelson, C. Button, M. Hopkinson, M. Pate, and J. Epler, in *Proceedings of the 25th IEEE Photovoltaic Specialists Conference* (IEEE, New Jersey, 1996), p. 113.

[60] C. Blaauw, F. R. Shepherd, and D. Eger, J. Appl. Phys. **66**, 605 (1989).

[61] O. Y. Raisky, W. B. Wang, R. R. Alfano, C. L. Reynolds Jr., D. V. Stampone, and M. W. Focht, Appl. Phys. Lett. **74**, 129 (1999).

[62] S. Adachi, *Physical Properties of III-V Semiconductor Compounds: InP, InAs, GaAs, GaP, InGaAs and InGaAsP* (John Wiley & Sons, New York, New York, 1992).

[63] D. Cui, Z. Chen, S. Pan, H. Lu, and G. Yang, Phys. Rev. B **47**, 1354 (1993).

[64] H. Rücker, E. Molinari, and P. Lugli, Phys. Rev. B **44**, 3463 (1991).

[65] J. H. Heyman, K. Unterrainer, K. Craig, B. Gaidrikian, M. S. Sherwin, K. Campman, P. F. Hopkins, and A. C. Gossard, Phys. Rev. Lett. **74**, 2682 (1995).

[66] C. L. Reynolds Jr., V. Swaminathan, M. Geva, L. E. Smith, and L. C. Luther, J. Electron. Mater. **24**, 747 (1995).

[67] A. Jaeger, W. D. Sun, F. H. Pollak, C. L. Reynolds Jr., D. V. Stampone, M. W. Focht, O. Y. Raisky, W. B. Wang, and R. R. Alfano, J. Appl. Phys. **85**, 1921 (1999).

[68] N. Dai, A. Cavus, D. Dzakpasu, M. C. Tamargo, F. Semendy, N. Bambha, D. M. Hwang, and C. Y. Cheng, Appl. Phys. Lett. **66**, 2472 (1995).

[69] T. Takamoto, E. Ikeda, and H. Kurita, Appl. Phys. Lett. **70**, 381 (1997).

[70] C. Rohr, J. P. Connoly, K. W. J. Barnham, P. R. Griffin, J. Nelson, I. Ballard, A. Zachariou, C. Button, and J. Clark, in *Proceedings of the Second World Conference and Exhibition on Photovoltaic Solar Energy Conversion Conference* (PUBLISHER, Vienna, 1998), p. 1994.

[71] P. R. Griffin, I. Ballard, K. W. J. Barnham, J. Nelson, A. Zachariou, C. Button, M. Hopkinson, and M. A. Pate, in *Proceedings of the Third NREL Conference on Thermophotovoltaic Generation of Electricity* (PUBLISHER, ADDRESS, 1997), pp. 411–421.

[72] A. Dhingra and A. Rothwarf, IEEE Trans. Electron. Devices **43**, 613 (1996).

[73] A. K. Newman and J. M. Liu, J. Appl. Phys. **82**, 4637 (1997).

[74] S. Kolodinski, J. H. Werner, T. Wittchen, and H. J. Queisser, Appl. Phys. Lett. **63**, 2405 (1993).

[75] W. Schockley and H. J. Queisser, J. Appl. Phys. **32**, 510 (1961).

[76] M. Wolf, R. Brendel, J. H. Werner, and H. J. Queisser, J. Appl. Phys. **83**, 4213 (1998).

[77] R. Corkish and M. Green, in *Proceedings of the 23th IEEE Photovoltaic Specialists Conference* (IEEE, New Jersey, 1993), p. 675.

[78] P. Waver, J. Bruns, W. Seifert, H. Winnicke, D. Dräunig, and H. G. Wagemann, in *Proceedings of the 12th European Photovoltaic Solar Energy Conference* (Stephen, Belford, 1994), p. 1994.

[79] A. Luque and A. Martí, Phys. Rev. Lett. **78**, 5014 (1997).

Index

approximation
    depletion, 62
    electric dipole, 25
    envelope function, 21
Arrhenius plot, 56

band
    bending, 43
    offset, 21
bandgap
    graded, 190
Bloch functions, 17

CCD, 87
coherent time, 45
critical layer thickness, 33
cryostat, 91
current
    short circuit, 67

deformation
    potential, 34
    shear, 34
density of states, 63
detector array, 87
DIP, 100
drift
    velocity, 57
DSP, 89

effective mass, 18
electro-optical modulators, 37
electronic band structure, 17
electroreflectance, 12, 158, 165
energy
    subband, 24
epilayer, 33
equation
    Boltzmann, 58
    current density, 65
    Schrödinger, 17
exciton
    bound, 57
    free, 56
extinction coefficient, 53

Fermi Golden Rule, 25
field
    quasi-electric, 191
fill factor, 67
FKO, 166
Franz-Keldysh effect, 166

GPIB, 91

heteroepitaxy, 98
homoepitaxy, 98
hot electrons, 60

IEEE-488, 87
integration time, 88

Kelvin measurements, 95
$k \cdot p$ method, 18

LabWindows/CVI, 91, 198
lattice
    constants, 15

MBE, 15
misfit dislocations, 33
mobility, 57
model
    Ben Daniel-Duke, 23
MOVPE, 15

nanostructures, 15
NDR, 1
negative differential resistance, 45

peak-to-valley current ratio, 47
phase-sensitive detector, 88
photolithography, 98
photoresist, 99
p-n junction, 62
PSD, 89
pseudomorphic, 33

QHT, 93
quantum
    dots, 15
    well, 15
    wires, 15

recombination
    Auger, 42
    radiative, 42
region
    depleted, 63

semiconductor
    compensated, 56
Shockley-Read-Hall statistics, 43
SIMS, 12, 158, 165, 167
Source–Measure Unit, 88
spectral
    chromatic aberration, 86
    response, 64
spin-orbit interaction, 19
stoichiometry, 15
superlattice, 15

thermal equilibrium, 41
Thermophotovoltaics, 190
transition
    free-to-bound, 55
    band-to-band, 55
TRIAX-320, 87
tunneling
    nonresonant, 44
    phonon-assisted, 9
    resonant, 44

van Roosbruck-Schokley relation, 54
voltage
    open circuit, 67

wafers, 99
wave vector, 17

ZIF, 101